Bimetallic and Metal/Semiconductor Nanoparticle-Embedded Polymer Thin Films: Catalyst, Photocatalyst and SERS Substrate

A Thesis Submitted for the Degree of
DOCTOR OF PHILOSOPHY

by

Vanjarapu Kesava Rao

School of Chemistry
University of Hyderabad
Hyderabad 500 046
INDIA

December 2016

Dedicated To

My Parents

CONTENTS

DECLARATION

I hereby declare that the matter embodied in this thesis is the result of investigations carried out by me in the School of Chemistry, University of Hyderabad, Hyderabad under the supervision of Prof. T. P. Radhakrishnan.

In keeping with the general practice of reporting scientific observations, due acknowledgements have been made wherever the work described is based on the findings of other investigators.

V. Kesava Rao

CERTIFICATE

This is to certify that the thesis entitled "**Bimetallic and Metal/Semiconductor Nanoparticle-Embedded Polymer Thin Films: Catalyst, Photocatalyst and SERS Substrate**" submitted by **V. Kesava Rao** bearing registration number **11CHPH15** in partial fulfillment of the requirements for award of Doctor of Philosophy in the School of Chemistry is a bonafide work carried out by him under my supervision and guidance.

This thesis is free from plagiarism and has not been submitted previously in part or in full to this or any other University or Institution for award of any degree or diploma.

Parts of this thesis have been:

A. Published in the following publications:

1. Rao, V. K.; Radhakrishnan, T. P. *J. Mater. Chem. A* **2013**, *1*, 13612–13618. **(Chapter 2)**
2. Rao, V. K.; Radhakrishnan, T. P. *Mater. Res. Bull*. **2017**, *87*, 193-201. **(Chapter 3)**
3. Rao, V. K.; Radhakrishnan, T. P. *ACS Appl. Mater. Interfaces* **2015**, *7*, 12767−12773. **(Chapter 4)**
4. Rao, V. K.; Ghildiyal, P.; Radhakrishnan, T. P. *J. Phys. Chem. C* (accepted). **(Chapter 5)**

and

B. Presented in the following Conferences:

1. 13th Eurasia Conference on Chemical Science, (International).
2. 7th International workshop on Polymer/Metal nanocomposites, (International).
3. Materials for the Millenium (MATCON-2016), (International).

Further the student has passed the following courses towards fulfillment of course work requirement for Ph.D:

Course code	Name	Credits	Pass/Fail
1. CY-801	Research Proposal	3	Pass
2. CY-805	Instrumental Methods A	3	Pass
3. CY-806	Instrumental Methods B	3	Pass
4. CY-850	Chemistry of Materials	3	Pass

Prof. T. P. Radhakrishnan
(Thesis Supervisor)

Dean
School of Chemistry

ACKNOWLEDGEMENTS

I would like to acknowledge and extend my heartfelt gratitude to Prof. T. P. Radhakrishnan, my research supervisor for his constant guidance, encouragement and for the freedom he gave me in carrying out my research. His innovative thoughts, commitment to the work with a great sense of discipline and patience are highly admirable and motivating which I always have aspired to imbibe. My association with him is a memorable one.

I thank present and former Deans and faculty members of the School of Chemistry for their support and help on various occasions. I thank Prof. T. Jana and Prof. R. Chandrasekhar for the support as doctorial committee members. I thank all the faculty members for their cooperation whenever required. I thank all non-teaching staff, School of Chemistry for their cooperation. I would also like to thank Prof. D. Narayana Rao (physics) and Dr. B. L. V. Prasad (NCL, Pune), for their support and help in my doctoral research.

My sincere thanks to all the teachers for their excellent teaching during my masters course. From their inspired and dedicated teaching, I have benefited much in my career. My special thanks to Prof. M. Ray (M.Sc supervisor), Prof. J. B. Barua and Prof. B. Mondal (IIT Guwahati) for the excellent teaching and inspiration they gave in my M.Sc days. I am thankful to Prof. C. N. R. Rao, Prof. T. K. Maji, Prof. Eswara Murty and Dr. A. Govinda Raj (JNCASR, Bangalore) for their contribution to start my research career.

I would like to express my sincere gratitude to Mr. Durgaprasad Muvva (TEM, CFN), Mr. Sunil (FESEM, School of chemistry), Mr Laksmi narayana (FESEM, School of Physics), Mr. Pavan (SEM, CIL), Ms. Sandya (Profilometer), Mr. Bhaskar Rao (LC-MS), Mr. Venkata Ramana (GC-MS) and Mr. Anand (N_2 gas) for their assistance in various instruments is greatly appreciated. I thank UGC for providing the fellowship.

I am deeply indebted to all my teachers right from my school to the University for the excellent training I received throughout my academics. Especially to my teachers Prasad, Banuji from my school days; Galib, Vissaly, Ganesh, Srinivas, Dr. K. Sharma, Dr. Mohana Rao, Dr. satyavathi, Dr. Nagarajan, Mr. Danial, Ms. Nanda Chowdary and Mr. Bhuma Reddy from my college days. My thanks to Dr. Leela Srinivas (IITB), Dr. Saikumar and Dr. Gurunath for their guidance during summer projects.

It is a great pleasure to thank my seniors Dr. Ramesh, Dr. Hari, Dr. Gupta and Balaswamy for their help and cooperation. I am extremely thankful to Srujana and Lasya for their help, support and encouragement during my Ph.D. I am also thankful to Durgaprasad for his support. I thank Divya, Senthil and Dr. Jony for their support in lab. I also acknowledge project students worked with me; Abhisek, Shibu, Pankaj and Iswarya. I also acknowledge the project students worked in lab. ***I thank all the research scholars of School of chemistry and friends*** for the cheerful and enlivening atmosphere they maintained and for making my stay in the campus unforgettable.

It's my pleasure to acknowledge my friends, MSc: Saiakat, Jashobanta and Susmith, BSc: Sri Shailu, Krishna, Bhaskar, Narsimha, Chiru, Yudhister and Mahesh, Inter: Naveen, Rama Rao and Satyanarayana. I specially thank my Roommates, Ugandhar, Dr. Shiva, Srinu and Dr. Karunakar during Ph.D for making my stay pleasant and memorable moments which I have shared with them.

I am at a loss of words to express gratitude to my parents. The way I grew up, the values I imbibed, the education I received and the person I am now is all due to them. I am grateful to my caring and loving sisters who have always been an ardent listeners and a strong support to me. I would like to acknowledge all my relatives for their love and encouragement.

V. Kesava Rao

COMMON ABBREVIATIONS

AFM	atomic force microscope
EF	enhancement factor
EDXS	energy dispersive X-ray spectroscopy
FESEM	field emission scanning electron microscope
GC-MS	gas chromatography-mass spectrometer
ICP-OES	inductively coupled plasma - optical emission spectroscopy
IC	ion chromatography
kDa	kilodalton
kW	kilowatt
LOD	limit of detection
LSPR	localized surface plasmon resonance
mL	milliliter
µL	microliter
µm	micrometer
µW	microwatt
nm	nanometer
M_w	weight average molecular weight
MB	methylene blue
MO	methyl orange
mW	milliwatt
ppb	parts-per-billion
pmol	picomol
PVA	poly(vinyl alcohol)
PS	polystyrene
RPM	revolutions per minute
R6G	rhodamine 6G
SERS	surface enhanced Raman scattering
TEM	transmission electron microscope
TON	turn-over-number
TOF	turn-over-frequency
t	time
T	temperature
XPS	x-ray photoelectron spectroscopy
x	metal to polymer weight ratio

CHAPTER 1

Introduction

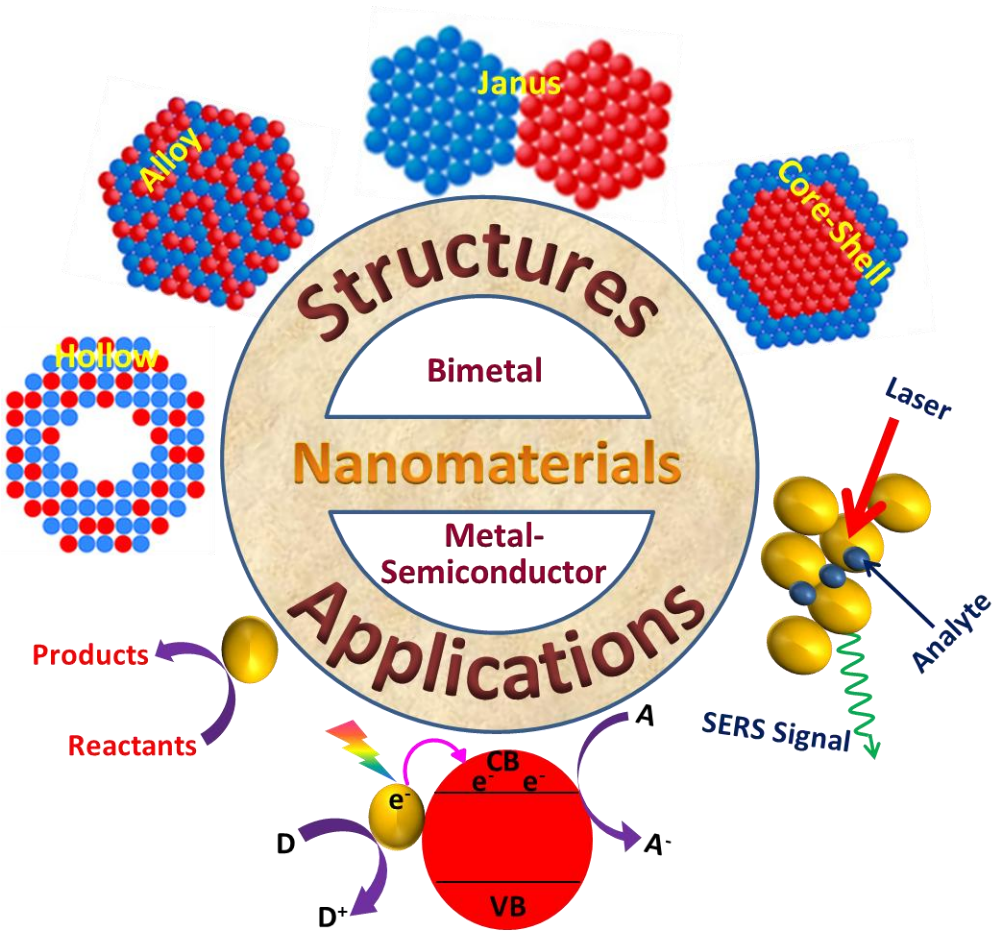

Synthesis and structures as well as applications of bimetallic and metal-semiconductor nanoparticles are discussed in this chapter.

Scope

The ability to synthesize bimetallic and metal-semiconductor nanoparticles of desired composition, size and shape facilitates precise tailoring of their properties and the eventual use of these structures in various applications, ranging from electronics and photonics, catalysis and sensing, to biology and medicine. Focus of the work presented in this thesis is bimetallic nanoparticles and metal-semiconductor nanoparticles with specific composition and structure, fabricated in situ inside a solid polymer thin film matrix. The former is obtained by the galvanic displacement route using suitable templates, whereas the latter is formed through a seed-mediated method. The prospect of using nanoparticle-embedded polymer thin films is extremely attractive since they exhibit the mutualistic effect from the components present. In situ generation of the nanoparticles is one of the most convenient, simple and efficient route to the fabrication of the nanocomposite thin films. The soft-chemical protocol we have optimized for the fabrication of bimetal nanostructures as well as metal-semiconductor nanoparticles inside the polymer thin films is environment-friendly, with the polymer acting as the stabilizing agent, and also as the reducing agent in many of the cases. We have employed the nanocomposite thin films in various applications such as chemical catalysis, photocatalysis and surface-enhanced Raman scattering (SERS).

This chapter is developed as follows. First, we present a brief introduction to the different types of materials (Sec. 1.1). Sec. 1.2 describes the historical aspects, uniqueness and classification of nanomaterials. The following sections discuss the synthesis and structures, as well as the properties and applications of bimetallic nanoparticles (Sec. 1.3) and metal-semiconductor nanocomposites (Sec. 1.4). The methodologies available for the fabrication of polymer thin films embedded with in situ generated metal nanoparticles and the unique features and applications that highlight the versatility of these nanocomposite materials are presented in Sec. 1.5. Sec.1.6 offers an overview of the topics of particular interest in this thesis, namely nanoparticles in catalysis, photocatalysis and surface-enhanced Raman scattering. Layout of the thesis is outlined in Sec. 1.7.

1.1 Materials

Materials play a crucial role in our daily life, covering a wide range of arenas such as transportation, housing, clothing, communication and food production. The various applications exploit their basic properties such as mechanical, electrical, thermal, magnetic, optical, and various combinations of these. Various factors such as the elemental composition, bonding, structure, presence of impurities, surface structure and method of fabrication can alter the properties associated with materials. However, inherent properties of these materials are generally independent of the actual physical size and shape. The nature and type of materials are often classified based on their chemical/elemental composition and bonding interactions.[1]

Metals, Dielectrics and Semiconductors

Metals are characterized by a large density of non-localized electrons (the so-called free electrons) contributed from the unbound electrons of the constituent atoms. They are good conductors of electricity and heat. Combination of two or more metals, called alloys, can show increased chemical stability and strength as well as novel properties over the components; examples are the increased stability of Fe-Cr and magnetic properties of Cu-Mn. Dielectrics are compounds with strong covalent bonding between metal and nonmetal elements; examples include oxides, nitrides and carbides, as well as clay minerals, and ceramics that are hard and stable up to high temperatures. They are electrical insulators; showing low charge transport, but capable of charge storage through polarization. Semiconducting materials, also composed of similar atoms as in dielectrics, show electrical conductivity between metals and semiconductors, which are highly sensitive to the presence of small amount of impurity atoms. Electrical conductivity of semiconductors increases with temperature, a trend opposite to that shown by metals. Examples of semiconductors include Si, Ge, TiO_2, ZnO, GaAs etc. Semiconductors are used extensively in various applications, including electronics, catalysis, and sensors.

Molecular Materials and Polymers

Molecular materials are composed of small molecules or molecular ions as well as macromolecules, held together by relatively weak interactions like hydrogen bonds, π-stacking and dispersion forces. The molecular properties are largely transferred to the bulk material, with novel features added due to the association. An important aspect of these materials is that they can be easily dissociated into their constituents through dissolution in appropriate solvents, melting or sublimation, and reassembled into new structures with properties that are different from the earlier assembly.[2] Polymers are versatile materials with special mechanical properties. Conjugated polymers are unique materials as they exhibit additionally, metallic or semiconducting properties as well. Examples of polymers include rubber, nylon and silk as well as the natural polymers such as proteins, enzymes, starch, and cellulose; polyacetylene and polyaniline are famous examples of conjugated polymers.

Composites and Biomaterials

Composite materials consist of more than one disparate material type, and may show synergetic properties arising from the individual components. If optimised protocols are used for the synthesis, they exhibit a combination of the best characteristics of each of the constituents; for example, fiberglass acquires the strength of glass and flexibility of the polymer forming the composite. Biomaterials are composites, natural or synthetic, alive or lifeless, and usually fabricated from the various types of materials discussed above including metals, polymers, ceramics, etc., which are compatible with biological systems. Natural biomaterials include shells, bones and teeth. Synthetic biomaterials are frequently used in medical applications to augment or replace a natural function. Examples include heart valve, bone plates, hip joint, contact lenses, drug delivery systems and scaffolding for tissue regeneration.[3]

1.2 Nanomaterials

Nanomaterials are characterised by size scales in the range of 1-100 nm, at least in one dimension.[4,5] They exhibit properties that are different from the bulk materials as well as the building blocks such as atoms or molecules. Without being established as such, nanomaterials, have been used from ancient days in applications that utilise their optical and medicinal properties. "Swarna Bhasma" an ancient Indian medicine is now established to be made up of gold nanoparticles.[6] "Lycurgus cup" from the 4th century AD[7] is another example; it appears greenish under reflected light and red when illuminated from inside, the optical properties arising due to the embedded gold and silver nanoparticles (Fig. 1.1a). The magnificent south rose windows (Fig. 1.1b) of Notre Dame Cathedral also get their color from the metal nanoparticles embedded in the glass. Nanowires in the Mediterranean cementite and carbon nanotubes in Wootz steel are other famous examples.[8]

The ability to master the synthesis and characterization, and eventually targeted application of nanomaterials has led to the emergence of the field of nanoscience and nanotechnology. The first documented synthetic route for Au nanoparticles (finely divided gold) was given by Faraday in 1857;[9] it involved the reduction of gold chloride

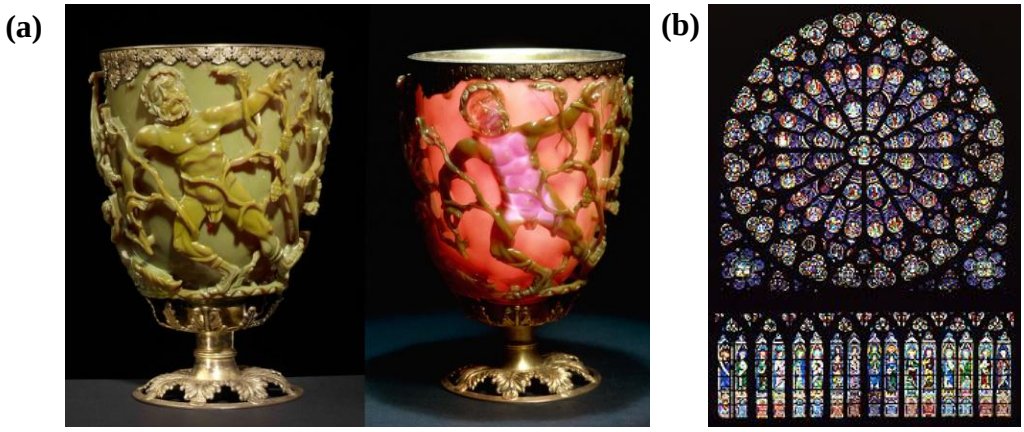

Figure 1.1. ***(a)*** *The Lycurgus cup in reflected light (green) and transmitted light (red) and* ***(b)*** *magnificent south rose window of Notre Dame Cathedral (figure adapted from ref. 5).*

using phosphorus in CS_2. Many theoretical approaches were developed to understand the optical properties of nanoparticles. Maxwell-Garnett gave the first quantitative theoretical description of light scattering by small particles in 1904; he assumed that the particles size is negligible compared to the wavelength of the incident light.[10] Later, Mie provided the first theoretical treatment for optical properties of small particles in 1908.[11] The morphology and structure of nanoparticles were directly observed only after the invention of electron and probe microscopy techniques. The electron microscope was invented by Knoll and Ruska, in which they used an electron beam rather than visible light. Later, in 1938 Prebus and Hillers built the first practical transmission electron microscope (TEM). TEM provides high-resolution images of nanostructures using electron beams with the wavelength comparable to atomic dimensions achieved by accelerating the electrons in the vacuum. In 1981, Binning and Rohrer invented the scanning tunneling microscope (STM); which provides some of the highest resolutions in imaging to date.[12] In 1986, Binning, Quate and Gerber invented the atomic force microscope (AFM).[13] Earlier in 1959, Feynman had highlighted the importance of physics at extremely small length scales, in his famous lecture entitled, “There's Plenty of Room at the Bottom”.[14] Taniguchi used the term "nanotechnology" for the first time in 1974. The discovery of carbon nanotubes, fullerenes and graphene has further advanced the field of nanoscience and nanotechnology. [15]

The unique nature of nanomaterials originates from the fact that, upon decreasing the size of the material to a few nanometers, they exhibit high surface to volume ratio[16,17] and confined quantum electronic states,[18,19] resulting in characteristic properties that are different from that of their bulk state. In the case of nanomaterials, relatively large fractions of atoms are on the surface as the surface to volume ratio increases; atoms at the surface have fewer neighbours than those present in the bulk. This leads to various effects such as decrease in the melting point of the material and efficient catalytic and bacterial action. Stabilization of specific surfaces can impart special catalytic capability to nanoparticles. At extremely small sizes, electronic energy levels of nanoparticles become discrete, changing from the continuous band structure. Unique effects such as absorption in the visible region due to localized surface plasmon

resonance (LSPR) can be observed, whereas bulk metal reflects. The unique features of nanomaterial have been exploited in a broad range of areas such as energy, environment, medicine, textiles, cosmetics, food and information technology.

Gleiter classified nanomaterials based on the growth habit and morphology;[20] and later, Skorokhod extended it further.[21] They classified nanomaterials into 2-, 1- and 0-dimensional structure based on extension of the bulk material. 2-dimensional structures include thin films and plates with a variety of shapes, wires, fibres and rods belong to 1-dimensional structures; spheres, clusters and cubes are examples of 0-dimensional system (Fig. 1.2). Anisotropy of the shape usually expressed as an aspect ratio, is basic to the description of a 2- dimensional or 1-dimensional structure. Unusual structures like bipods, tripods and multipods do not fit into this classification. Powders and fibrous, multilayer and polycrystalline materials in which the 0-D, 1-D and 2-D structural components are connected with each other and form interfaces, belong to 3-D materials.

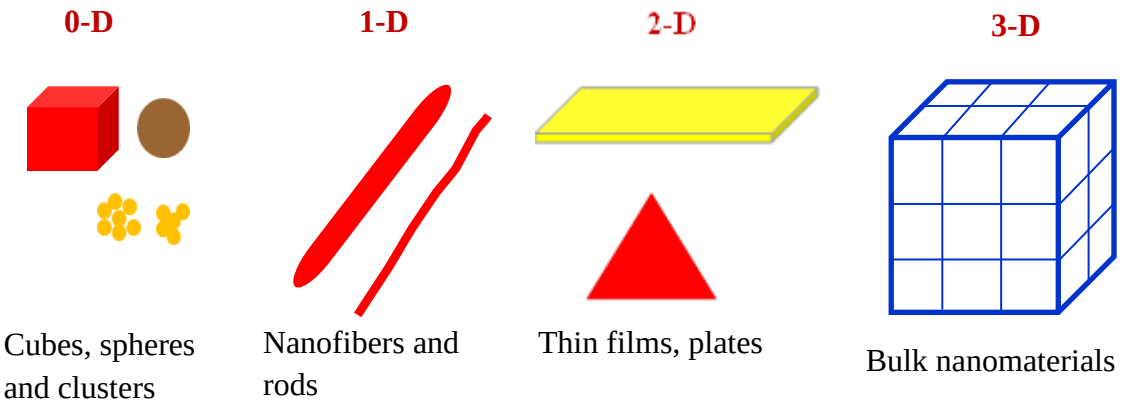

Figure 1.2. *Classification of nanomaterials based on growth habit (figure adapted from ref. 21).*

1.3 Bimetallic Nanoparticles

Bimetallic nanoparticles have attracted considerable attention in recent times.[22,23] Combination of two different metals in the same nanoparticle adds the possibility of tuning the composition and structure, in order to vary the characteristics of the nanoparticles. The two elements involved can adopt different organizations, core-shell, hollow structures and alloys are common (Fig. 1.3). Alloys may have segregated domains of the two atoms or a homogeneous distribution which may be random (solid solution) or with a specific structure;[24,25] Janus structures have also been reported.[26] The composition, structure, size and shape of the bimetallic nanoparticles control their electronic structure and surface organization, leading to unique physical attributes and chemical reactivities.[27-29]

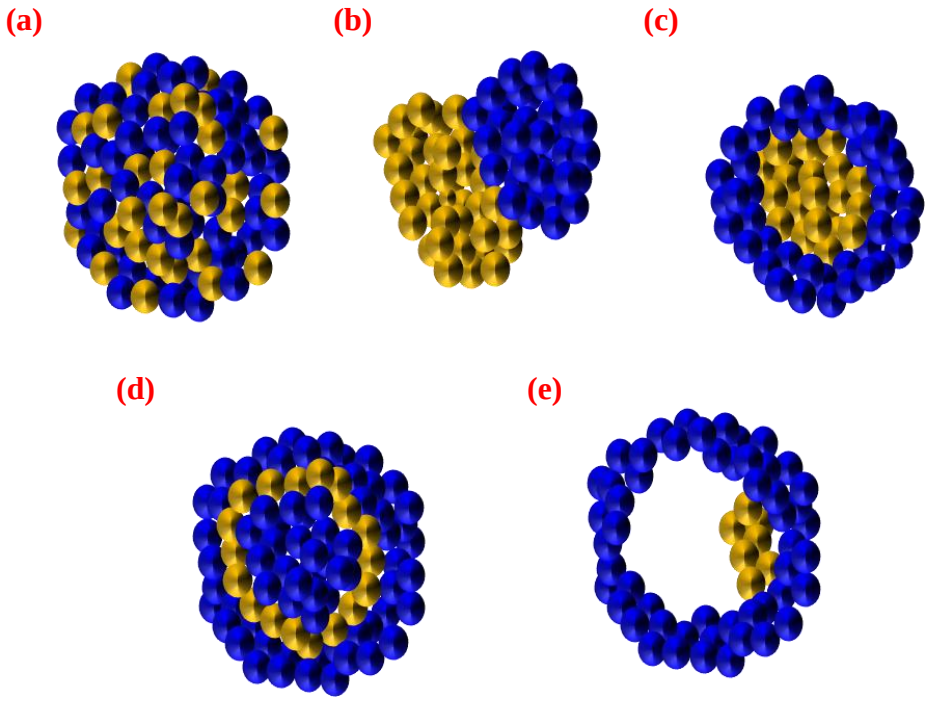

Figure 1.3. *Schematic of the structures of bimetallic nanoparticles:* ***(a)*** *mixed alloys;* ***(b)*** *subclusters with an interface* ***(c)*** *core-shell nanoparticles* ***(d)*** *multishell core-shell nanoparticles and* ***(e)*** *movable core within hollow shell material (figure adapted from refs. 24 and 25).*

1.3.1 *Synthesis and Structures*

Co-reduction is commonly used to produce alloy and intermetallic compounds.[30-32] It involves simultaneous reduction of two metal precursors as well as nucleation and growth of the atoms together, resulting in the nanostructures. Structure of the bimetallic nanoparticles is tailored by exploiting parameters such as the reduction potentials of the metal ions, reducing agents, coordinating ligands, capping agents, and the reaction temperature. This method is favourable for metal ions with small difference in their redox potentials. Pd-Pt alloy nanoparticles[33] are prepared by simultaneous reduction of $Pd(acac)_2$ and $Pt(acac)_2$ with morpholine borane, and nanoparticles of Au-Ag alloy is achieved by concomitant reduction of $HAuCl_4$ and $AgNO_3$ with oleylamine.[34]

Thermal decomposition is another popular method for the fabrication of bimetallic nanoparticles, often in alloy form. It involves the decomposition of two metal precursors concurrently or a bimetallic precursor compound at elevated temperatures. It is highly favourable for metals with relatively low standard reduction potentials such as Fe, Co and Ni, which are difficult to convert to the metal chemically. Simultaneous decomposition of $Fe(CO)_5$ and $Co_2(CO)_8$ leads to the formation of Fe-Co nanocrystals;[35] Fe-Pt nanocrystals have been prepared by decomposing $Pt_3Fe_3(CO)_{15}$.[36]

Core-shell nanoparticles are specifically obtained through seed-mediated growth approach as, such structures are difficult to achieve either through co-reduction or thermal decomposition methods. This is a prominent route for the fabrication of rationally designed bimetallic nanoparticles with precise architecture. In this route, pre-synthesized monometal nanoparticles with definite shape are used as seeds, and the second metal is nucleated heterogeneously on the seed by either reduction or thermal decomposition of the metal precursor. Heterogeneous nucleation has low energy barrier compared to homogeneous nucleation; due to this factor, the second metal (material) nucleates easily on the seed particles. Pt nanocubes are used as seeds to synthesize Pt@Pd core-shell nanocrystals[37] through the overgrowth of Pd on Pt surface.

Galvanic displacement strategy is widely used to fabricate hollow bimetallic nanoparticles.[38,39] Metal nanoparticles with low standard reduction potentials are used to reduce ions of a second metal with high reduction potentials, where the former one acts as a sacrificial template. The second metal ions are reduced by the electrons from the template atoms, and grow on the surface while the interior atoms that are oxidized, dissolve into the reaction medium. This process results in hollow bimetallic structures.[40] These uniquely structured nanoparticles are difficult to fabricate through other methods. Ag nanocrystals with a definite shape were used as a sacrificial template to obtain various hollow bimetallic systems such as Ag-Au, Ag-Pd and Ag-Pt.[41-43] Also, other metal nanoparticles like Ni, Cu, Co and Pb have been used as sacrificial templates to generate hollow bimetallic nanoparticles.[44]

1.3.2 *Properties and Applications*

Similar to single metal nanoparticles, the optical properties of bimetallic nanoparticles are affected by various factors such as size, shape and the dielectric environment; additionally, the properties are crucially dependent on the composition and structure. Bimetallic nanoparticles are used in several applications such as catalysis, photocatalysis, SERS and sensing. The characteristic LSPR of metal nanoparticles is due to the collective oscillation of the surface free electrons resonating with the incident light (Fig. 1.4).[45] The LSPR lies in the visible region for metals like Ag, Au and Cu; it occurs in the ultraviolet (UV) region for Ru, Rh, Pd and Pt nanoparticles.[46,47] The scattering of light by small particles can be understood in terms of the Mie theory, wherein Maxwell's equations are solved for a homogeneous sphere irradiated by an electromagnetic plane wave. It is applicable when the size of the spherical particle is negligible compared to the incident light wavelength. The extinction cross section is given by,

$$C_{ext}(\lambda) = \frac{24\pi^2 R^3 \varepsilon_m^{3/2}(\lambda)}{\lambda} \frac{\varepsilon_i(\lambda)}{[\varepsilon_r(\lambda) + 2\varepsilon_m(\lambda)]^2 + \varepsilon_i^{\,2}(\lambda)}$$

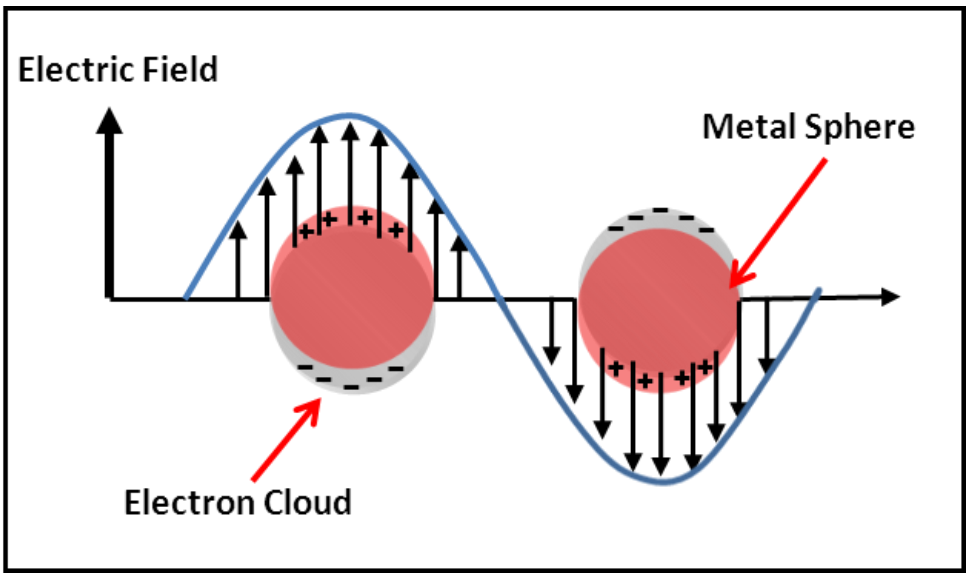

Figure 1.4. *Localized surface plasmon resonance due to the coherent interaction of the electrons with light in metal nanoparticles.*

where λ is the incident light wavelength, ε_m is the dielectric constant of the surrounding medium,[48] R is the radius, and ε_r and ε_i are the real and imaginary parts of the dielectric constant of the particles. The dielectric constant of the nanocrystals is assumed to be similar to that of the material in the bulk state, independent of the size and shape. The LSPR shifts towards the higher wavelength with increasing size of the metal nanoparticles or an increasing dielectric constant of the medium. Mie theory can also be applied to spherical bimetallic nanocrystals, with the dielectric constant of the alloy (of M and N metals) is taken to be, $\varepsilon_{MN}(\alpha) = \alpha\varepsilon_M + (1 - \alpha)\varepsilon_N$ (where α is mole-fraction of M and ε_M and ε_N are the dielectric constants of pure M and N respectively). Size dependent dielectric constants are used in some extensions of the Mie theory.[49] Simulation methods, such as DDA[50] and FDTD[51] are widely used to model LSPR spectra of nanoparticles; to explore the impact of size, shape, composition and structure (hollow, core-shell, etc.,). The LSPR of bimetallic (Au-Ag, Au-Cu and Ag-Cu)[52-54] nanoparticles can be tuned over the visible region, exploiting the composition, structure and shape. Combinations with metals like Pd or Pt result in drastic dampening of the LSPR extinction of Ag nanoparticles.

Bimetallic nanoparticles often show higher catalytic activity in terms of turn-over-number (TON) or frequency (TOF) compared to individual metal nanoparticles, and hence are highly useful in industrial applications. Rate of a catalytic reaction strongly depends on the adsorption process. The coordination number of atoms on the surface depends on the facets of the metal nanoparticles, which therefore influence the activity in heterogeneous catalysis.[55] In the case of fcc metals, {111}, {100} and {110} - facets have a coordination number of 9, 8 and 7 respectively. {111}-facet is the most stable. Nanosized defects like steps or kinks usually have a coordination number of 6. Bligaard and Nørskov demonstrated that energetic differences between these different facets on a catalytic surface could vary by up to 1 eV for the chemisorption of CO on Pt.[56] Incorporating the second metal can result in many new effects including charge transfer between the two different surface atoms, altering the electronic structure and activity. The spatial arrangement of surface atoms is affected by strain, geometry and size. A typical example of bimetallic nanoparticle catalyst is Au-Pd used for the acetoxylation of ethylene to vinyl acetate.[57] Growing catalytic Pt from the ends of plasmonic Au rods gave a novel class of bimetallic hybrid whose catalytic activity could be enhanced using light.[58] Depositing Pd on the surface of magnetic Ni nanocrystals produces a catalyst with high activity per Pd atom as all the atoms being on the surface are catalytically active; it also makes the hybrid system magnetically recoverable.[59]

Bimetallic magnetic nanoparticles have attracted great interest in various fields such as biomedicine[60] and information storage[61] in addition to catalysis. Ni, Co and Fe nanoparticles as well as their alloys (Co-Ni, Fe-Pt and Co-Pt) exhibit ferromagnetism. Nanomagnetic materials behave as single domain magnets when reduced down to a critical size, whereas bulk materials are composed of multiple magnetic domains. When a ferromagnetic nanocrystal is reduced even further in size, it eventually reaches the superparamagnetic limit. The temperature above which ferromagnetic nanocrystals become superparamagnetic is known as the blocking temperature. It is observed that the incorporation of strong spin-orbit coupling metals (Rh, Pd and Pt) into metals with large local magnetic moments (Fe, Co and Ni) enhance their magnetic moments,

stability and anisotropy.[62] For example, FePt alloy is stabler, and exhibits superior magnetic properties compared to their single metal nanoparticles.[63,64]

1.4 Metal-Semiconductor Nanoparticles

Metal-semiconductor nanoparticles are useful hybrid materials showing novel properties because of the synergistic effect of the individual components, in addition to the impact of size, shape, structure and composition. The combination of two different materials, metals and semiconductors, can be fabricated through different processes and growth mechanisms (as shown in Fig. 1.5).[65-70]

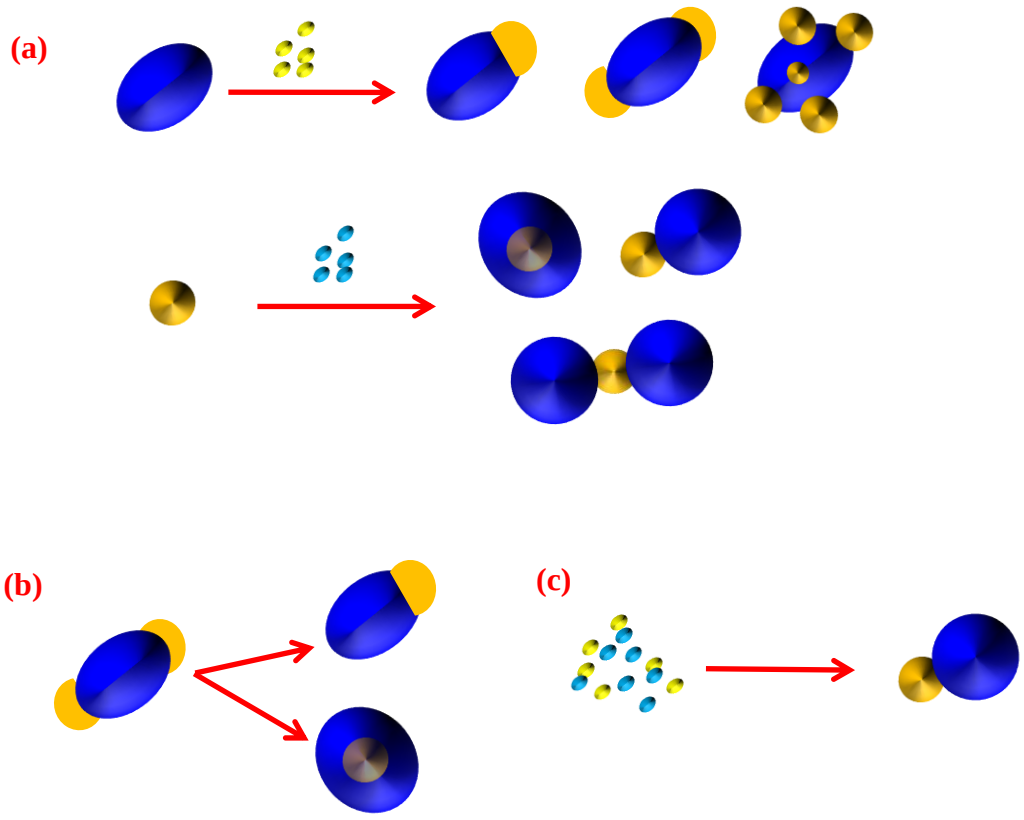

Figure 1.5. *Schematic of growth mechanisms **(a)** surface nucleation and growth of a second phase on a seed nanoparticle **(b)** surface nucleation followed by surface diffusion of the metal phase and an inward diffusion and **(c)** simultaneous nucleation and growth of both materials (figure adapted from ref. 65).*

1.4.1 *Synthesis and Structure*

Seed-mediated growth is commonly employed to fabricate metal-semiconductor nanoparticles. Semiconducting nanomaterials are often used as seeds and metal nanoparticles are grown heterogeneously on the seed surface (Fig. 1.5a). The final structure of the composite material depends on various factors such as the size, morphology and facets of the seed. For example, Au nanocrystals preferentially nucleate at the tips of CdSe and CdS nanorods rather than on the side walls, because the facets of the tips possess relatively higher surface energy.[71-74] High temperature as well as light have been used as external stimuli to overcome the energetic barrier for the growth of Co on TiO_2[75] and Ag on ZnO[76] respectively. Nucleation and growth on the surface may be followed by diffusion (Fig. 1.5b). Diffusion on the surface can lead to coalescence of clusters at a single location, either on the surface of the hybrid particle or within the center of the hybrid particle. Gold diffuses into InAs nanocrystal due to the concentration gradient between the surface and interior of the particles.[77]

Nucleation and growth of nanocrystal can occur concurrently. In this process the initial seeds are not isolated before the second material grows; the two fragments grow mostly independently (Fig. 1.5c). The above route is used in the synthesis of Ag/AgBr hybrid nanocrystals, in which Ag and AgBr nanocrystal are nucleated and grown simultaneously, where the Ag nanocrystals are obtained by the reduction of silver ions which are coordinated to ionic surfactant containing a bromide counterion.[78] Replacement of a sacrificial domain involves the conversion of heterostructure nanocrystals into hybrid nanoparticles, primarily through the replacement or reaction of a sacrificial component within the heterostructure nanocrystal. Liu and Guyot reported the synthesis of Ag_2S- and Ag_2Se-coated gold nanoparticles by treating the core-shell Au@Ag nanoparticles with sodium sulfide or selenourea.[79]

1.4.2 *Properties and Applications*

The unique properties of metal-semiconductor nanocomposites arise from the fundamentally different nature of the individual components in the system as well as the

interaction between the two at the metal-semiconductor contact. The metal-semiconductor nanoparticles show remarkable optical properties due to interaction of the different electronic structures. Metal nanoparticles exhibit LSPR, whereas the semiconducting materials often show photoluminescence characteristics. The plasmon peak of the metal nanoparticles can be shifted to longer wavelength in the presence of semiconducting material with a higher index of refraction;[80] a typical example is the Au/CdS nanoparticles.[81] Luminescence of the semiconducting material may be quenched or enhanced in the presence of metal nanoparticles. Fluorescence quenching can occur due to the energy transfer from the exciton in the semiconductor to the metal. Au in Au/CdSe,[71] Au/CdS[72] or Au/InAs[77] hybrid nanosystems is known to quench the fluorescence of the respective semiconductor. Fluorescence enhancement together with the decreased lifetime is known to occur due to the interaction between

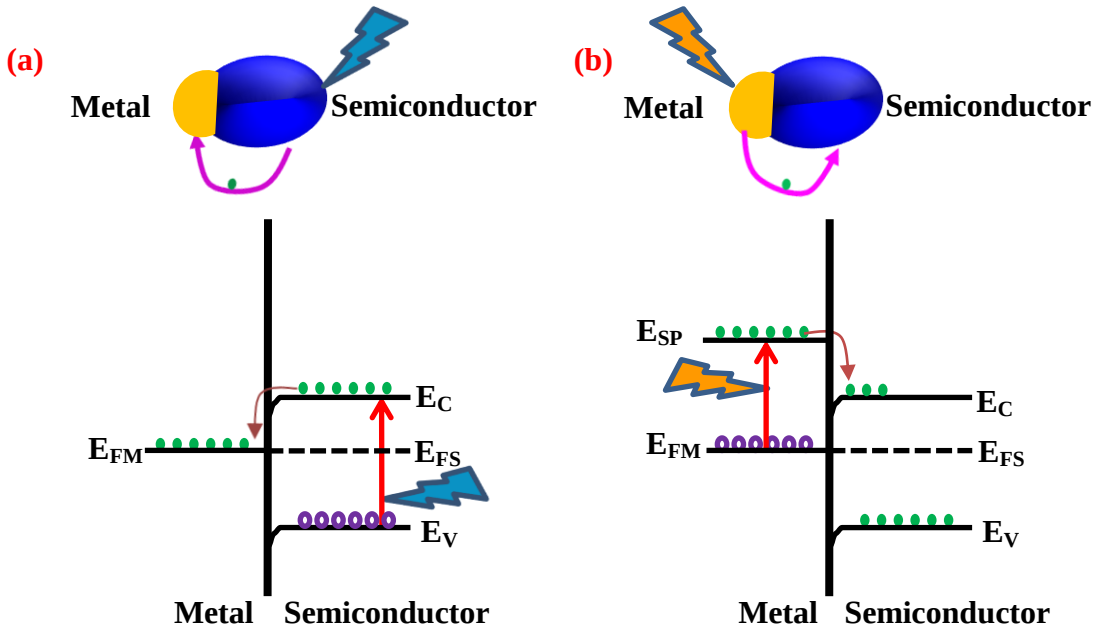

Figure 1.6. *Schematics illustrating the generation of electrons and holes, and electron transfer from* ***(a)*** *the semiconductor to the metal and* ***(b)*** *the metal to the semiconductor (where E_{SP} and E_{FM} refer to the surface plasmon state and Fermi level of metal, E_{FS} is the Fermi level of the semiconductor) (figure adapted from ref. 84).*

collective surface plasmons of metal nanoparticles and the excitons of the semiconductor nanowires; this was observed in CdTe nanowires with chemically linked Au nanocrystals.[82]

Metal-semiconductor hybrid nanoparticles are known to be efficient photocatalysts, providing efficient charge separation at the metal-semiconductor interface. Photon absorption by the semiconductor or metal region generates an electron–hole pair, followed by the fast transfer of one of the charge carriers into the closely spaced energy levels in the metal (Fig. 1.6a) or semiconductor (Fig. 1.6b) nanoparticle domain.[83] Most of the semiconductors have strong absorption only in the UV region, which constitutes only about 4% of the entire solar spectrum. An efficient photocatalyst must have absorption that extends into the visible range. Therefore semiconducting materials are combined with plasmonic metals mainly Ag and Au, to enhance the absorption in the visible region. Metallic deposits on oxide nanocrystals (TiO_2, ZnO),[84,85] significantly improve the photocatalytic and photoelectrochemical responses of the semiconductor cores, as photoinduced charge carrier separation is promoted upon electron migration towards the metal domain. The latter can also favor fast electron release to suitable acceptors in the solution. Recently, Ag/AgCl nanocomposites have attracted attention as efficient photocatalysts.[86]

1.5 Metal-Polymer Nanocomposite Thin Films

Metal-polymer nanocomposite materials are versatile materials in which the nanoparticles are stabilized inside a polymer matrix. The properties such as the optical response of the nanoparticles are affected by the dielectric environment of the polymer,[87] whereas the mechanical properties and thermal behaviour of the polymer are influenced by the presence of the metal nanoparticles.[88-90]

1.5.1 *Fabrication*

The metal-polymer nanocomposites can be fabricated through different methods,[91] which can be broadly classified as *in situ*[92] and *ex situ*.[93] *In situ* method

involves generally two steps: in the first step, metal precursor is incorporated into the polymer or monomer (before polymerization); the metal ions are reduced using thermal treatment, light irradiation etc., resulting in metal nanoparticles in the second step. In the case of *ex situ* methods, the pre-synthesized metal nanoparticles are mixed with the polymer or the monomer which is subsequently polymerized. *In situ* synthesis offers a relatively more homogeneous distribution of metal nanoparticles in the polymer matrix. Several *in situ* methods have been developed, among which two methods are commonly

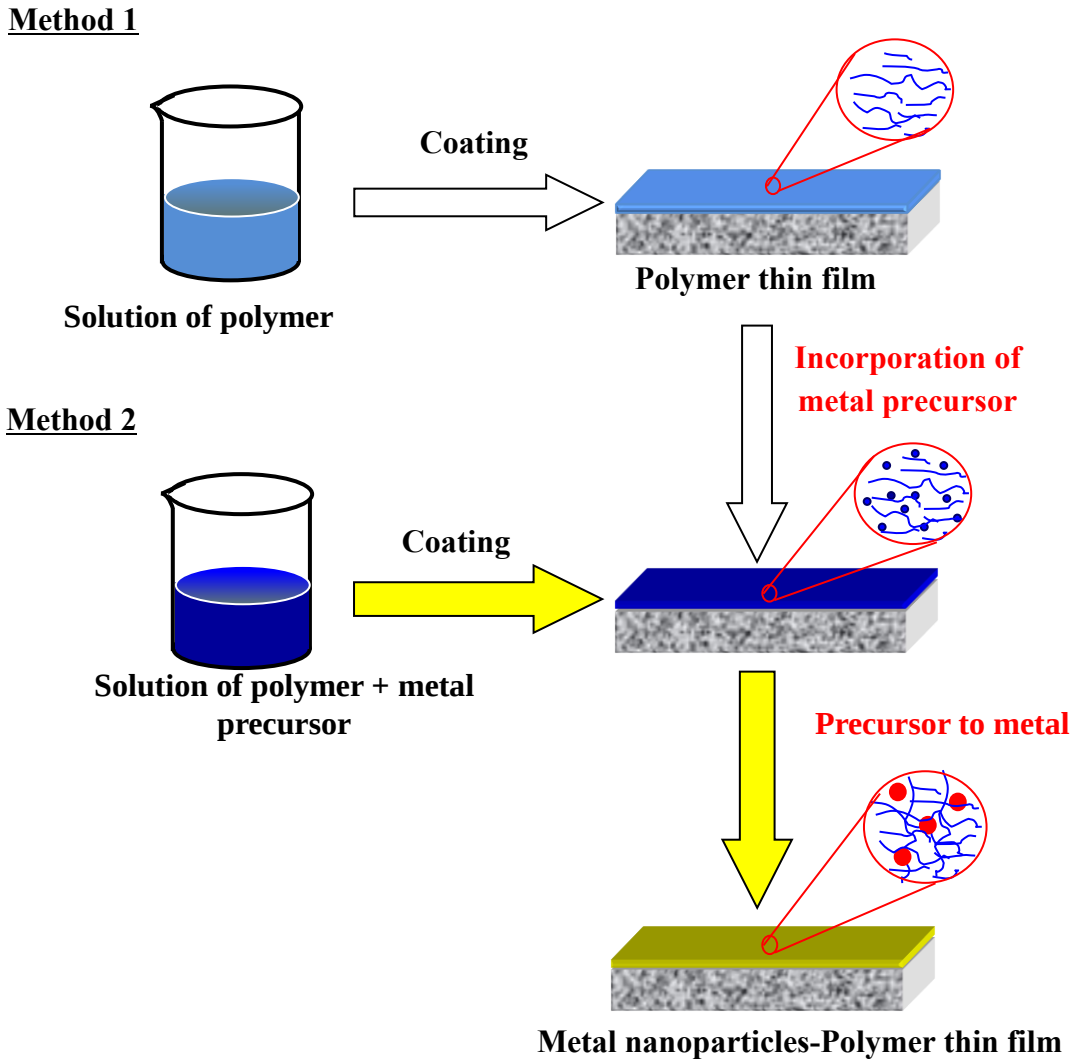

Figure 1.7. *Schematic of the two approaches employed for the in situ synthesis of metal nanoparticles inside a polymer thin film on substrate (figure adapted from refs. 100 and 101).*

used to generate metal nanoparticles inside a solid polymer thin film (Fig. 1.7). In Method 1, the metal precursor is incorporated into a prefabricated polymer thin film through different methods (treatment with metal precursor solution[94-97] or vapor,[98] plasma treatment, etc.,) whereas in Method 2, a mixture of the polymer and metal precursor in solution is used for coating the film to obtain the metal precursor-polymer thin film. The film formed by either method (through spin-coating commonly) is treated by various ways such as photo-irradiation, chemical reduction, electrochemical reduction[99] and thermal treatment to generate the nanoparticles *in situ* inside the film. In general, Method 2 produces a more homogeneous distribution of nanoparticles than Method 1. Thermal treatment is probably the simplest procedure, which can cause either

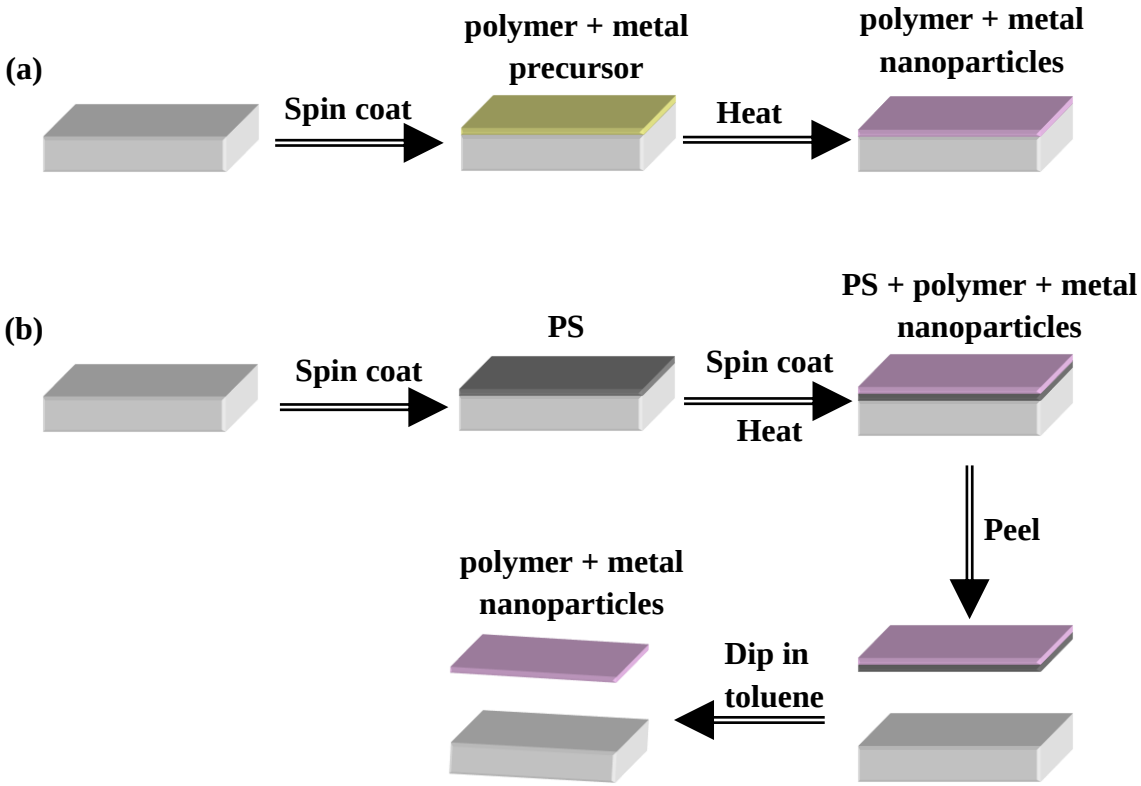

Figure 1.8. *Schematic of the protocol developed in our laboratory for the in situ synthesis of metal nanoparticles inside PVA film and the fabrication of* ***(a)*** *film on substrate and* ***(b)*** *free-standing films (figure adapted from refs. 100 and 101); (PS=polystyrene).*

decomposition of the precursor or reduction of the metal ion precursor by the polymer itself; polymers with functional groups like alcohols and amines can act as reducing agents. The metal-polymer nanocomposites are fabricated in different forms including fibers, gels and thin films. A simple protocol has been developed in our lab, for the fabrication of nanoparticles of metals such as Ag, Au, Pd, Hg and Pt,[100,101] embedded in a polymer thin film on substrates as well as free standing form (Fig. 1.8a,b).[102] The method ensures the formation of the metal nanoparticles within the polymer matrix thereby avoiding their exposure to the environment. Poly(vinyl alcohol) (PVA) is one of the best choices for the polymer, as it reduces the metal precursor under mild thermal annealing conditions or photo-irradiation, using the hydroxyl groups. The reduction of metal ions to atoms and their aggregation to form nanoparticles inside the polymer film is accompanied by chemical changes in the polymer including oxidation of hydroxyl groups and formation of ether cross-linkage.[103] Formation of the metal nanoparticles can be conveniently monitored through various spectroscopy and microscopy techniques. Free standing films obtained using the polystyrene (PS) as the supporting layer which is dissolved out subsequently (Fig. 1.8b) are extremely thin, and can be used directly for imaging in a TEM. The size, shape and density of the metal nanoparticles in polymer thin films can be tailored by changing the metal to polymer ratio, viscosity of the solution and the spin-coating conditions and finally the thermal annealing time and temperature. Polymers such as the poly(vinylpyrrolidone) (PVP) and poly(vinyl butyral-*co*-vinyl alcohol-*co*-vinyl acetate) (PVVV) have also been used to prepare metal-polymer nanocomposite thin film in our laboratory.

A wide range of spectroscopy and microscopy techniques have been used for monitoring the formation as well as the final structure and composition of the metal nanoparticles. Electronic absorption/extinction spectrum is used to monitor the emergence of the characteristic LSPR of the metal nanoparticles in the visible or UV region. The process can be followed as a function of time to monitor the progress and completion.[104,105] X-ray photoelectron spectroscopy (XPS) provides proof of the reduction of the metal ions to atoms based on the oxidation state changes.[106-108] Atomic force microscopy (AFM) has been used not only to look at the final nanocomposite

film, but also for real-time monitoring of the *in situ* growth of nanostructures in the polymer film.[109,110] Scanning electron microscopy (SEM) and transmission electron microscopy (TEM), combined with energy dispersive X-ray scattering (EDXS) and selected area electron diffraction (SAED) are used for the detailed characterization of the nanomaterials, including size, shape, composition and structure. Besides these, X-ray diffraction (XRD) techniques can be used to characterize the size and structure of crystalline metal nanoparticles and simultaneously, any crystalline structure present in the polymer. Formation of gold nanoparticles inside PVA films by photo-irradiation has been monitored using XRD.[111]

1.5.2 *Applications*

Metal-polymer nanocomposite thin films fabricated through *in situ* methods have been shown to be useful in a number of applications. Simultaneous formation of metal nanoparticles and polymer chain cross-linking results in reduced solubility of the final nanocomposite thin film, thereby enhancing its application potential in aqueous media. The hydrogel character of polymers such as PVA and the swelling of the thin film in solution media facilitates contact between the external medium and the metal nanoparticles embedded within the film. These characteristics are essential for various applications such as catalysis and sensing. Metal-polymer nanocomposite thin films with different noble metals such as Ag, Au, Pd and Pt, have been used as optical limiter,[102,112,113] microwave absorber,[114] random laser,[115] surface-enhanced Raman scattering substrates (SERS),[116,117] sensor,[118] antibacterial,[119] catalyst[120] and in electron beam lithography (EBL).[121]

1.6 Applications of Interest in This Thesis

1.6.1 *Nanoparticles as Catalysts*

Catalysts are an integral part of the production of fine chemicals, plastics and fertilizers as well as the remediation of environmental pollutants. Catalysts are classified as homogeneous and heterogeneous. Even though, homogeneous catalysts are

in general highly efficient, there is an inherent problem of catalyst separation for recycling, thereby reducing the overall catalyst utilisation. Heterogeneous catalysis offers a more convenient option for catalyst recovery; however, the catalytic activity is limited as the surface atoms only are involved in the conversion of reactants to products. Metal nanoparticles are highly attractive as catalysts, as the large fraction of surface atoms present are utilised. However, proper embedding in a matrix is essential to effect efficient recovery. If that is achieved, nanocatalysts can harness the benefits of homogeneous and heterogeneous catalysis.[122] Catalytic activities of metal nanoparticles have been studied extensively, and the relevance of size and shape has been highlighted. Nanoparticles with sharp edges and corners as well as rough surfaces have high catalytic efficiency.[123] The structure can indeed influence the catalytic activity, so also the incorporation of another metal. Au@Pd core-shell nanoparticles catalyse the Suzuki-Miyaura coupling between chlorobenzene and phenylboronic acid more efficiently than pure Pd.[124] Hollow nanoparticles with high surface area and low density exhibit high catalytic activity than solid particles. In the case of oxygen reduction and methanol oxidation reactions, Pt nanotubes and Pt hollow spheres have been shown to exhibit higher activity than their solid counterparts.[125] Separation of the catalyst and products is further improved by incorporating the metal nanoparticles into various supports like oxides, magnetic nanostructures, carbon nanotubes and polymers.[126] The concept of 'dip catalysts' developed in our laboratory exploits the possibility of nanocatalyst-embedded polymer thin film that can be conveniently introduced in a reaction system and retrieved by simple mechanical dipping and removal.[127,128]

1.6.2 *Nanoparticles as Photocatalysts*

Semiconductor nanomaterials are widely used as photocatalysts in applications, such as degradation of pollutants, water splitting and sunlight harvesting. Photocatalysis is one of the focal areas of research and development in the broad arena of sustainable energy, manufacturing and environmental remediation technologies. Inexpensive and easily fabricated photocatalysts with high efficiency and reusability, form an important and evolving theme of research. Metal-semiconductor composite

nanostructures are prime candidates in these applications. Nanoparticles of noble metals like Ag, Au and Cu show strong light absorption in the visible regime. The metal-semiconductor interface facilitates the separation of charge carriers generated by light absorption; these electrons and holes induce reductive and oxidative reactions leading to photocatalysis. Exploitation of this general principle has led to extensive research on the design and fabrication of plasmonic photocatalysts.

Even though combinations like Au/TiO_2, Ag/Ag_3PO_4 and Ag/AgBr have been explored,[129-131] the most extensively studied and popular new composites in this field are Ag/AgCl or AgCl/Ag (nano Ag on nano/micro AgCl or the reverse respectively). The high photocatalytic efficiency results from the strong visible light absorption due to the LSPR of the Ag nanoparticle, and the separation of the photo-generated charge carriers by the intense electric fields at the Schottky junction between Ag and AgCl.

1.6.3 *Nanoparticles as SERS Substrates*

When light interacts with matter, it undergoes various processes like transmission, absorption and scattering. The scattered light can have the same energy as the incident light ($h\upsilon_I$) (known as Rayleigh scattering) as well as different energies (known as Raman scattering) (Fig. 1.9). Vibrational Raman transition arises from the change in the polarizability (α) during the molecular vibrations. Only a very small fraction of the incident photons undergo Raman scattering.[132]

The inherently weak Raman signal is enhanced significantly through the influence of the strong local field offered by the substrate surface.[133-137] The surface-enhanced Raman scattering (SERS) effect has been explained in terms of the general mechanism of electromagnetic field enhancement[138] as well as the role of chemical enhancement effects[139,140] in specific cases. While the latter addresses the impact of the substrate surface on the analyte molecule through chemical interactions such as charge transfer, the former is a consequence of the strong local field provided by the surface. Metal nanoparticles, especially those of Ag, Au and Cu, with their strong LSPR fields

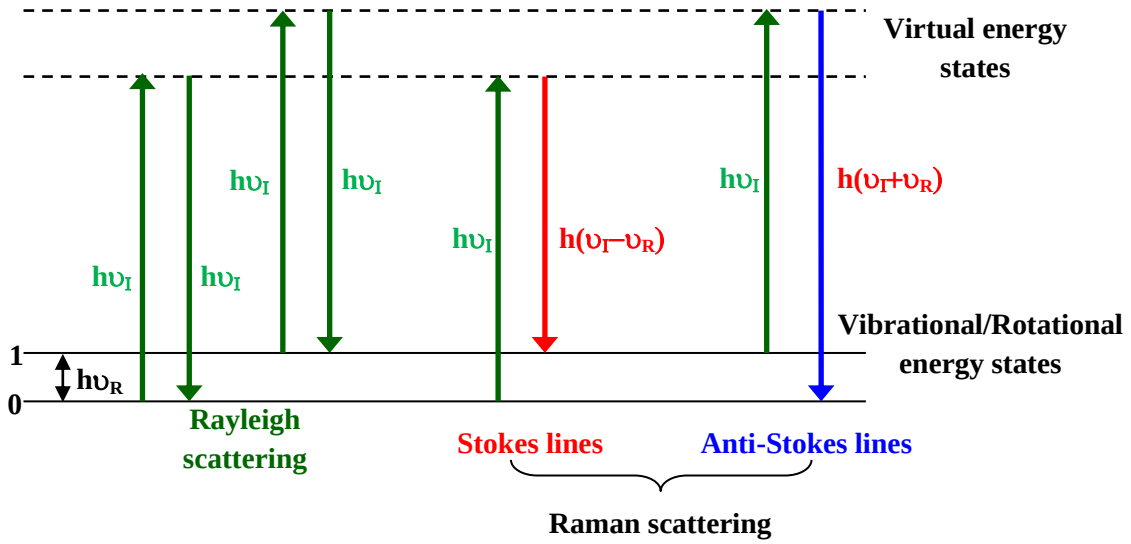

Figure 1.9. *A schematic illustration of Raman and Rayleigh scattering of light.*

which can be excited by visible radiation, have been the popular choices for realizing high SERS effects.

The SERS response is critically dependent on the impact of the local electric field on the exciting (frequency = ν_I) and scattered (frequency = ν_R) photons in the Raman process [$\Delta\nu_{Stokes/Anti\text{-}Stokes} = \pm(\nu_I\text{-}\nu_R)$]. Therefore the SERS enhancement factor (EF) due to a metal nanoparticle based substrate is likely to be influenced by the correlation between the LSPR energy and the exciting laser energy. Wavelength-scan studies with different substrates have shown that maximum enhancement occurs when the LSPR peak is approximately midway between the ν_I and ν_R; for Stokes lines in the Raman spectrum, maximum EF is obtained when the LSPR peak is slightly red-shifted with respect to the exciting laser wavelength.[141,142] However, several studies show that the correlation between the LSPR extinction and the SERS EF is not so straight forward. The link between the LSPR extinction and the SERS can be quite indirect and the spatial distribution of resonance plays a significant role, the bulk-like character of the collective resonance at a specific wavelength contributing to the extinction and the surface-like character to the SERS.[143] The inherent competition between extinction and enhancement can lead to maximum signals off-resonance, at optimal concentrations in

colloidal media, and in particular when the LSPR is blue-shifted with respect to ν_I.[144,145] Another factor of fundamental relevance in this context is that the extinction is controlled by the far-field behaviour of the plasmonic substrate while the SERS response is determined by the near-field effects which once again makes the correlation between the two responses complex.[146] A major focus in the development of SERS substrates has been the generation of large local fields through the formation of features such as 'hot spots'.[147,148] The impact of cluster size and inter-particle separation in nanoparticle aggregates on the near field enhancement and the design of ultrasensitive plasmonic nanostructures for SERS have been investigated in detail.[149,150] From an alternate perspective, the facility with which the LSPR of metal nanoparticles can be systematically tailored through various methods, allows fundamental studies of SERS EF tuning and optimization of the substrate to realize maximum enhancement. LSPR of metal nanoparticles such as Au and Ag have been tuned by varying their size and shape, and different aspects of their assembly.[151-155]

1.7 Layout of the Thesis

The main objective of this thesis is to develop and optimize new protocols for the *in situ* generation of bimetallic as well as metal/semiconductor nanoparticles embedded in polymer thin films, and explore their unique application potentials. The *in situ* fabrication strategy is simple and environmentally benign. Following earlier work in our laboratory on metal-polymer composites; we have used PVA as the polymer because it can reduce most of the noble metals as well as act as a stabilizer for the nanoparticles. This polymer is soft and water soluble; it has excellent film forming capability and is biodegradable. In this thesis, we have explored a variety of problems: details of the *in situ* formation of metal nanoparticle, and the control of the size of Ag as well as Cu nanoparticles, use of these particles as templates for the fabrication of bimetallic nanoparticles such as Ag-Pd, Ag-Au and Cu-Ag. The metal/semiconductor composite nanoparticles of Ag/AgCl in PVA thin film were also developed. We present our investigations of Ag-Pd-PVA and Ag/AgCl-PVA thin films as catalyst and photocatalyst respectively; Ag-Au-PVA and Cu-Ag-PVA thin films are shown to be

efficient SERS substrates. The thesis is organized in six chapters. Following the introductory material presented in this chapter, we present details of our investigations in the following chapters as noted below.

Chapter 2

This chapter focuses on the *in situ* formation of Ag-Pd nanoparticles embedded in polymer thin films. The Ag nanoparticles size was tuned by introducing catalytic amounts of Cu^{2+} into the reaction mixture. Ag nanoparticles with selected size range, embedded in the polymer thin film are used subsequently as sacrificial templates to generate hollow Ag-Pd nanoparticles *in situ* inside polymer thin film by treating with aqueous K_2PdCl_4 under ambient conditions, in a galvanic displacement reaction. Hollow Ag-Pd nanoparticles embedded in PVA thin film were employed as 'dip catalysts' in the Suzuki-Miyaura reaction of iodobenzene with phenylboronic acid. The TON and TOF obtained using the bimetallic nanoparticles were shown to be significantly higher than that obtained with monometallic nanoparticles.

Chapter 3

Ag/AgCl nanoparticles were synthesized inside a PVA thin film in two steps. In the first step, AgCl nanoparticles were formed by mixing $AgNO_3$ and HCl in presence of PVA, and the solution was spin coated to form AgCl-PVA thin film. Photo-irradiation of AgCl-PVA film in the second step led to the formation of Ag/AgCl-PVA. The thin film was used as an efficient photocatalyst for the degradation of methyl orange dye. Extensive recyclability and the unique advantage of convenient catalyst monitoring between the reuse cycles were demonstrated.

Chapter 4

The general methodology developed in Chapter 2, was extended to fabricate Ag-Au nanoparticles embedded in a polymer thin film. Ag-Au nanoparticles with various compositions were fabricated in PVA thin film by treating the Ag-PVA films with different concentrations of $HAuCl_4$ solutions under ambient conditions. The LSPR of

the system could be tuned over the visible region, by varying the compositions systematically. The Ag-Au-PVA thin films with different Ag and Au composition were used as SERS substrates. Raman scattering experiments were carried out using R6G as the analyte molecule. The SERS enhancement was shown to vary strongly with the Ag-Au composition; high enhancement factor was obtained for the Ag-Au-PVA thin film with low amount of Au. Correlation of the enhancement factor with the LSPR extinction was analysed.

Chapter 5

This chapter focuses on the fabrication of Cu nanoparticles in the polymer thin films followed by the fabrication of Cu-Ag-PVA thin films. CuO-PVA thin films were first prepared by thermal decomposition of $Cu(NO_3)_2$ incorporated in a PVA thin film. Cu-PVA nanocomposite thin film was fabricated by exposing the CuO-PVA thin film to hydrazine vapors. Cu nanoparticles embedded in the polymer film was used as a sacrificial template to generate Cu-Ag nanoparticles through galvanic displacement reaction by treating with aqueous $AgNO_3$. Cu-Ag-PVA with different compositions, Cu-PVA and Ag-PVA thin films were studied to explore their efficiency as SERS substrates. Raman scattering experiments with analyte molecules such as rhodamine 6G and methylene blue and under different excitation lasers, established Cu-Ag-PVA as a highly efficient SERS substrate for broad spectra applications.

Chapter 6

The final chapter presents a brief overview of the various investigations in this thesis and highlights the significant achievements of the new explorations. The highlights of the work include: (i) the development of general, simple and mild strategies to fabricate *in situ* inside a polymer thin film, bimetallic and metal-semiconductor nanoparticles with tuned composition and structure, (ii) the demonstration of effective use of these nanocomposite thin films in catalytic, photocatalytic and SERS applications. The new directions in which the present studies can be expanded and evolved are also discussed in this chapter.

References

1. Callister, W. D.; Rethwisch, D. G. *Fundamentals of materials science and engineering: An integrated approach*. Hoboken, N. J: John Wiley & Sons, **2008.**
2. Radhakrishnan, T. P. *Acc. Chem. Res.* **2008**, *41*, 367-376.
3. Huebsch, N.; Mooney, D. J. *Nature* **2009,** *462*, 426-432
4. Fahlman, B. D. *Materials Chemistry*, Vol. 1, Springer, Mount Pleasant, **2007**.
5. Vajtai, R. *Springer Handbook of Nanomaterials,* Springer, **2013.**
6. Brown, C. L.; Bushell, G.; Whitehouse, M. W.; Agrawal, D. S.; Tupe, S. G.; Paknikar, K. M.; Tiekink, E. R. T. *Gold Bulletin*. **2007**, *40*, 245-250.
7. Freestone, I.; Meeks, N.; Sax, M.; Higgitt, C. *Gold Bulletin* **2007**, *40*, 270-277.
8. Reibold, M.; Paufler, P.; Levin, A.A.; Kochmann, W.; Patzke, N.; Meyer, D. C. *Nature* **2006**, *444*, 286.
9. Faraday, M. *Philos. Trans. R. Soc. London* **1857**, *147*, 145-181.
10. Maxwell-Garnett, J. C. *Phil. Trans. R. Soc. Lond. A* **1904**, *203*, 385-420.
11. Mie, G. *Ann. d. Physik* **1908,** *25*, 377-445.
12. Swart, I.; Liljeroth, P.; Vanmaekelbergh, D. *Chem. Rev*. **2016**, *116*, 11181-11219.
13. Binnig, G. K.; Quate, C. F.; Gerber. C. *Phys. Rev. Lett.* **1986**, *56*, 930-933.
14. Feynman, R. P. *Engineering and Science* **1960,** *23*, 22-36.
15. Pinzón, R.; Villalta-Cerdas, A.; Echegoyen, L. *Top. Curr. Chem.* **2012**, *312*, 127-174.
16. Schmid, G. *Clusters and Colloids - From Theory to Applications*, VCH: Weinheim, Germany, **1994**.
17. Daniel, M. C.; Astruc, D. *Chem. Rev.* **2004,** *104*, 293-346.
18. Kubo, R. J. *Phys. Soc. Jpn*. **1962,** *17*, 975-986.

19. Ghosh, S. K.; Pal, T. *Chem. Rev.* **2007**, *107*, 4797-4862.

20. Gleiter, H. *Acta Mater.* **2000**, *48*, 1-29.

21. Skorokhod, V.; Ragulya, A.; Uvarova, I. *Physico-chemical Kinetics in Nanostructured Systems*, Academperiodica, Kyiv, **2001.**

22. Muñoz-Flores, B. M.; Kharisov, B. I.; Jiménez-Pérez, V. M.; Martínez, P. E.; López, S. T. *Ind. Eng. Chem. Res.* **2011**, *50*, 7705-7721.

23. Liu, X.; Liu, X. *Angew. Chem. Int. Ed.* **2012**, *51*, 3311-3313.

24. Ferrando, R.; Jellinek J.; Johnston, R. L. *Chem. Rev*. **2008**, *108*, 845-910.

25. Chaudhuri, R. G.; Paria, S. *Chem. Rev.* **2012**, *112*, 2373–2433.

26. Logsdail, A. J.; Johnston, R. L. *J. Phys. Chem. C* **2012**, *116*, 23616-23628.

27. Gilroy, K. D.; Ruditskiy, A.; Peng, H.-C.; Qin, D.; Xia, Y. *Chem. Rev*. **2016**, *116*, 10414–10472.

28. Toshima. N.; Yonezawa T. *New J. Chem*. **1998**, 1179-1201.

29. Yang, J.; Yang, J.; Ying, J. Y. *ACS Nano* **2012**, *6*, 9373-9382.

30. Weiner, R. G.; Kunz, M. R.; Skrabalak, S. E. *Acc. Chem. Res.* **2015**, *48*, 2688−2695.

31. Chi, M.; Wang, C.; Lei, Y.; Wang, G.; Li, D.; More, K. L.; Lupini, A.; Allard, L. F.; Markovic, N. M.; Stamenkovic, V. R. *Nat. Commun*. **2015**, *6*, 8925 (1-9).

32. Sra, A. K.; Schaak, R. E. *J. Am. Chem. Soc*. **2004**, *126*, 6667−6672.

33. Liu, Y.; Chi, M.; Mazumder, V.; More, K.; Soled, S.; Henao, J.; Sun, S. *Chem. Mater*. **2011**, *23*, 4199−4203.

34. Wang, C.; Yin, H.; Chan, R.; Peng, S.; Dai, S.; Sun, S. *Chem. Mater*. **2009**, *21*, 433−435.

35. Bönnemann, H.; Brand, R. A.; Brijoux, W.; Hofstadt, H. W.; Frerichs, M.; Kempter, V.; Maus-Friedrichs, W.; Matoussevitch, N.; Nagabhushana, K. S.; Voigts, F.; et al. *Organomet. Chem*. **2005**, *19*, 790−796.

36. Rutledge, R. D.; Morris, W. H.; Wellons, M. S.; Gai, Z.; Shen, J.; Bentley, J.; Wittig, J. E.; Lukehart, C. M. *J. Am. Chem. Soc*. **2006**, *128*, 14210−14211.

37. Habas, S. E.; Lee, H.; Radmilovic, V.; Somorjai, G. A.; Yang, P. *Nat. Mater*. **2007**, *6*, 692−697.

38. El Mel, A. A.; Chettab, M.; Gautron, E.; Chauvin, A.; Humbert, B.; Mevellec, J.-Y.; Delacote, C.; Thiry, D.; Stephant, N.; Ding, J.; Du, K.; Choi, C.-H.; Tessier, P-Y. *J. Phys. Chem. C* **2016**, *120*, 17652– 17659

39. Xia, X.; Wang, Y.; Ruditskiy, A.; Xia, Y. *Adv. Mater.* **2013**, *25*, 6313−6333.

40. Sun, Y.; Xia, Y. *J. Am. Chem. Soc*. **2004**, *126*, 3892−3901.

41. Meng, X. K.; Tang, S. C.; Vongehr, S. *J. Mater. Sci. Technol*. **2010**, *26*, 487−522.

42. Rycenga, M.; Cobley, C. M.; Zeng, J.; Li, W. Y.; Moran, C. H.; Zhang, Q.; Qin, D.; Xia, Y. *Chem. Rev*. **2011**, *111*, 3669−3712.

43. Cobley, C. M.; Xia, Y. *Mater. Sci. Eng. R* **2010**, *70*, 44−62.

44. Gilroy, K. D.; Farzinpour, P.; Sundar, A.; Hughes, R. A.; Neretina, S. *Chem. Mater*. **2014**, *26*, 3340−3347.

45. Zhang, J. Z.; Noguez, C. *Plasmonics* **2008**, *3*,127–150.

46. Liz-Marzan, M. N.; Murphy, C. J.; Wang, J. *Chem. Soc. Rev*. **2014**, *43*, 3820−3822.

47. Sanz, J. M.; Ortiz, D.; de la Osa, R. A.; Saiz, J. M.; Gonzalez, F.; Brown, A. S.; Losurdo, M.; Everitt, H. O.; Moreno, F. *J. Phys. Chem. C* **2013**, *117*, 19606−19615.

48. Cortie, M. B.; McDonagh, A. M. *Chem. Rev*. **2011**, *111*, 3713−3735.

49. Kreibig, U.; Vollmer, M. *Optical Properties of Metal Clusters*, Springer, Berlin, **1995.**

50. Draine, B. T.; Flatau, P. J. *J. Opt. Soc. Am. A* **1994**, *11*, 1491-1499.

51. Lumerical simulation: http://www.lumerical.com/

52. Mallin, M. P.; Murphy, C. J. *Nano Lett*. **2002**, *2*, 1235−1237.

53. Hajfathalian, M.; Gilroy, K. D.; Yaghoubzade, A.; Sundar, A.; Tan, T.; Hughes, R. A.; Neretina, S. *J. Phys. Chem. C* **2015**, *119*, 17308− 17315.

54. Smetana, A. B.; Klabunde, K. J.; Sorensen, C. M.; Ponce, A. A.; Mwale, B. *J. Phys. Chem. B* **2006**, *110*, 2155−2158.

55. Xie, S.; Choi, S.-I.; Xia, X.; Xia, Y. *Chem. Eng*. **2013**, *2*, 142−150.

56. Bligaard, T.; Nørskov, J. K. *Electrochim. Acta* **2007**, *52*, 5512−5516.

57. Chen, M.; Kumar, D.; Yi, C. W.; Goodman, D. W. *Science* **2005**, *310*, 291−293.

58. Wang, F.; Li, C.; Chen, H.; Jiang, R.; Sun, L. D.; Li, Q.; Wang, J.; Yu, J. C.; Yan, C. H. *J. Am. Chem. Soc*. **2013**, *135*, 5588−5601.

59. Dong, Z.; Le, X.; Dong, C.; Zhang, W.; Li, X.; Ma, J. *Appl. Catal. B* **2015**, *162*, 372−380.

60. Reddy, L. H.; Arias, J. L.; Nicolas, J.; Couvreur, P. *Chem. Rev*. **2012**, *112*, 5818−5878.

61. Skumryev, V.; Stoyanov, S.; Zhang, Y.; Hadjipanayis, G.; Givord, D.; Nogues, J. *Nature* **2003**, *423*, 850−853.

62. Bansmann, J.; Baker, S. H.; Binns, C.; Blackman, J. A.; Bucher, J. P.; Dorantes-Davila, J.; Dupuis, V.; Favre, L.; Kechrakos, D.;´ Kleibert, A.; et al. *Surf. Sci. Rep*. **2005**, *56*, 189−275.

63. Inomata, K.; Sawa, T.; Hashimoto, S. *J. Appl. Phys.* **1988**, *64*, 2537-2540.

64. Sun, S.; Murray, C. B.; Weller, D.; Folks, L.; Moser, A. *Science* **2000**, *287*, 1989−1992.

65. Costi, R.; Saunders, A. E.; Banin, U. *Angew. Chem. Int. Ed*. **2010**, *49*, 4878–4897.

66. Shaviv, E.; Schubert, O.; Alves-Santos, M.; Goldoni, G.; Di Felice, R.; Vallée, F.; Del Fatti, N.; Banin, U.; Sönnichsen, C. *ACS Nano* **2011**, *5*, 4712– 4719.

67. Uri, B.; Yuval, B.-S.; Kathy, V. *Chem. Mater*. **2014**, *26*, 97– 110.

68. Dawson, A.; Kamat P. V. *J. Phys. Chem. B* **2001**, *105*, 960–966.

69. Dutta, S. K.; Mehetor, S. K.; Pradhan, N. *J. Phys. Chem. Lett*. **2015**, *6*, 936−944.

70. Nag, A.; Kundu, J.; Hazarika, A. *CrystEngComm* **2014**, *16*, 9391– 9407.

71. Mokari, T.; Rothenberg, E.; Popov, I.; Costi, R.; Banin, U. *Science* **2004**, *304*, 1787-1790.

72. Saunders, A. E.; Popov, I.; Banin, U. *J. Phys. Chem. B* **2006**, *110*, 25421-25429.

73. Mokari, T.; Sztrum, C. G.; Salant, A.; Rabani, E.; Banin, U. *Nat. Mater.* **2005**, *4*, 855-863.

74. Menagen, G.; Mocatta, D.; Salant, A.; Popov, I.; Dorfs, D.; Banin, U. *Chem. Mater*. **2008**, *20*, 6900-6902.

75. Habas, S. E.; Yang, P. D.; Mokari, T. *J. Am. Chem. Soc*. **2008**, *130*, 3294-3295.

76. Pacholski, C.; Kornowski, A.; Weller, H. *Angew. Chem. Int. Ed.* **2004**, *43*, 4774-4777.

77. Mokari, T.; Aharoni, A.; Popov, I.; Banin, U. *Angew. Chem. Int. Ed*. **2006**, *45*, 8001-8005.

78. Saunders, A. E.; Popov, I.; Banin, U.; Anorg. Z. *Allg. Chem*. **2007**, *633*, 2414-2419.

79. Liu, M. Z.; Guyot-Sionnest, P. *J. Mater. Chem*. **2006**, *16*, 3942-3945.

80. Costi, R.; Saunders, A. E.; Banin, U. *Angew. Chem. Int. Ed.* **2010**, *49*, 4878 – 4897

81. Mulvaney, P. *Langmuir* **1996**, *12*, 788-800.

82. Lee, J.; Govorov, A. O.; Dulka, J.; Kotov, N. A. *Nano Lett*. **2004**, *4*, 2323-2330.

83. Kim, S. M.; Lee, S. W.; Moon, S. Y.; Park, J. Y. *J. Phys. Condens. Matter* **2016**, *28*, 254002 (1-13).

84. Hirakawa, T.; Kamat, P. V. *J. Am. Chem. Soc*. **2005**, *127*, 3928-3934.

85. Fragua, D. M.; Abargues, R.; Rodriguez-Canto, P. J.; Sanchez-Royo, J. F.; Agouram, S.; Martinez-Pastor, J. P. *Adv. Mater. Interfaces* **2015**, *2*, 1500156 (1-10).

86. Wang, P.; Huang, B.; Dai, Y.; Whangbo, M. *Phys. Chem. Chem. Phys.* **2012**, *14*, 9813–9825.

87. Stepanov, A. L. *Tech. Phys.* **2004**, *49*, 143-153.

88. Mbhele, Z. H.; Salemane, M. G.; van Sittert, C. G. C. E.; Nedeljković, J. M.; Djoković, V.; Luyt, A. S. *Chem. Mater*. **2003**, *15*, 5019-5024.

89. Mendoza, C.; Pietsch, T.; Gutmann, J. S.; Jehnichen, D.; Gindy, N.; Fahmi, A. *Macromolecules* **2009**, *42*, 1203-1211.

90. Arceo, A.; Meli, L.; Green, P. F. *Nano Lett.* **2008**, *8*, 2271-2276.

91. Heilmann, A. *Polymer Films with Embedded Metal Nanoparticles*, Springer, **2003**.

92. Sih, B. C.; Wolf, M. O. *Chem. Commun.* **2005**, 3375-3384.

93. Faupel, F.; Zaporojtchenko, V.; Strunskus, T.; Elbahri, M. *Adv. Eng. Mater*. **2010**, *12*, 1177-1190.

94. Won, J.; Ihn, K. J.; Kang, Y. S. *Langmuir* **2002**, *18*, 8246.

95. Korchev, A. S.; Bozack, M. J.; Slaten, B. L.; Mills, G. *J. Am. Chem. Soc.* **2004**, *126*, 10-11.

96. Li, J.; Kamata, K.; Watanabe, S.; Iyoda, T. *Adv. Mater.* **2007**, *19*, 1267-1271.

97. Sohn, B.; Seo, B.; Yoo, S. *J. Mater. Chem.* **2002**, *12*, 1730-1734.

98. Horiuchi, S.; Nakao, Y. *Curr. Nanosci.* **2007**, *3*, 206-214.

99. Shang, L.; Wang, Y.; Huang, L.; Dong, S. *Langmuir* **2007**, *23*, 7738-7744.

100. Ramesh, G. V.; Porel, S.; Radhakrishnan, T. P. *Chem. Soc. Rev.* **2009**, *38*, 2646−2656.

101. Hariprasad, E.; Radhakrishnan, T. P. in Nanocomposites: *In Situ* Synthesis of Polymer-Embedded Nanostructures, Eds. Carotenuto, G.; Nicolais, L. John Wiley, **2013**, p.129.

102. Porel, S.; Singh, S.; Harsha, S. S.; Rao, D. N.; Radhakrishnan, T. P. *Chem. Mater.* **2005**, *17*, 9-12.

103. Jaffe, H. L.; Rosenblum, F. M. Poly(vinyl alcohol) for Adhesives. In *Handbook of Adhesives;* Skeist, I., Ed.; Chapman and Hall: New York, **1990**; p. 401-407.

104. Porel, S.; Singh, S.; Radhakrishnan, T. P. *Chem. Commun.* **2005**, 2387-2389.

105. Porel, S.; Hebalkar, N.; Sreedhar, B.; Radhakrishnan, T. P. *Adv. Funct. Mater.* **2007**, *17*, 2550-2556.

106. Mendoza, C.; Pietsch, T.; Gutmann, J. S.; Jehnichen, D.; Gindy, N.; Fahmi, A. *Macromolecules* **2009**, *42*, 1203-1211.

107. Arceo, A.; Meli, L.; Green, P. F. *Nano Lett.* **2008**, *8*, 2271-2278.

108. Li, J.; Kamata, K.; Watanabe, S.; Iyoda, T. *Adv. Mater.* **2007**, *19*, 1267-1271.

109. Deshmukh, R. D.; Composto, R. J. *Chem. Mater.* **2007**, *19*, 745-754.

110. Ramesh, G. V.; Sreedhar, B.; Radhakrishnan, T. P. *Phys. Chem. Chem. Phys.* **2009**, *11*, 10059-10063.

111. Pucci, A.; Bernabò, M.; Elvati, P.; Meza, L. I.; Galembeck, F.; de Paula Leite, C. A.; Tirelli, N.; Ruggeriab, G. *J. Mater. Chem.* **2006**, *16*, 1058-1066.

112. Porel, S.; Venkatram, N.; Rao, D. N.; Radhakrishnan, T. P. *J. Appl. Phys*. **2007**, *102*, 033107.

113. Karthikeyan, B. *Physica B* **2005**, *364*, 328-332.

114. Ramesh, G. V.; Sudheendran, K.; Raju, K. C. J.; Sreedhar, B.; Radhakrishnan, T. P. *J. Nanosci. Nanotech.* **2009**, *9*, 261-266.

115. Meng, X.; Fujita, K.; Zong, Y.; Murai, S.; Tanaka, K. *Appl. Phys. Lett*. **2008**, *92*, 20112-20115.

116. Hasell, T.; Lagonigro, L.; Peacock, A. C.; Yoda, S.; Brown, P. D.; Sazio, P. J. A.; Howdle, S. M. *Adv. Funct. Mater.* **2008**, *18*, 1265-1271.

117. Hariprasad, E.; Radhakrishnan, T. P. *Langmuir* **2013**, *29*, 13050-13057.

118. Ramesh, G. V.; Radhakrishnan, T. P. *ACS Appl. Mater. Interfaces* **2011**, *3*, 988-994.

119. Porel, S.; Ramakrishna, D.; Hariprasad, E.; Gupta, A. D.; Radhakrishnan, T. P. *Curr. Sci.* **2011**, *101*, 927-934.

120. Hariprasad, E.; Radhakrishnan, T. P. *Chem. Eur. J.* **2010** *16*, 14378-14384.

121. Marqués-Hueso, J.; Abargues, R.; Canet-Ferrer, J.; Agouram, S.; Valdés, J. L.; Martínez-Pastor, J. P. *Langmuir* **2010**, *26*, 2825-2830.

122. Bergbreiter, D. E.; Tian, J.; Hongfa, C. *Chem. Rev.* **2009**, *109*, 530-582.

123. Mahmoud, M. A.; Narayanan, R.; El-Sayed, M. A. *Acc. Chem. Res.* **2013**, *46*, 1795-1805**.**

124. Cao, Y.; Jin, R.; Mirkin, C. A. *J. Am. Chem. Soc***. 2001**, *123*, 7961-7962.

125. Chen, Z. W.; Waje, M.; Li, W. Z.; Yan, Y. S. *Angew. Chem. Int. Ed.* **2007**, *46*, 4060-4063.

126. Haller, G. L.; Resasco, D. E. *Adv. Catal.* **1989**, *36*, 173-235.

127. Hariprasad, E.; Radhakrishnan, T. P. *Chem. Eur. J.* **2010**, *16*, 14378–14384.

128. Hariprasad, E.; Radhakrishnan, T. P. *ACS Catal.* **2012,** *2*, 1179−1186.

129. Liu, Z.; Hou, W.; Pavaskar, P.; Aykol, M.; Cronin, S. B. *Nano Lett*. **2011**, *11*, 1111–1116.

130. Liu, Y. P.; Fang, L.; Lu, H. D.; Liu, L. J.; Wang, H.; Hu, C. Z. *Catal. Commun.* **2012**, *17*, 200–204.

131. Kuai, L.; Geng, B.; Chen, X.; Zhao,Y.; Luo, Y. *Langmuir* **2010**, *26*, 18723–18727.

132. Long. D. A. *The Raman Effect: A Unified Treatment of the Theory of Raman Scattering by Molecules*, Wiley, **2002**.

133. Fleischman, M.; Hendra, P. J.; McQuillan, A. J. *Chem. Phys. Lett.* **1974,** *26,* 163-166.

134. Jeanmaire, D. L.; Van Duyne, R. P. *J. Electroanal. Chem.* **1977,** *84,* 1-20.

135. Albrecht, M. G.; Creighton, J. A. *J. Am. Chem. Soc.* **1977,** *99,* 5215-5217.

136. Campion, A.; Kambhampati, P. *Chem. Soc. Rev.* **1998,** *27,* 241-250.

137. Kneipp, K.; Kneipp, H.; Kneipp, J. *Acc. Chem. Res.* **2006,** *39,* 443-450.

138. Wang, W.; Li, Z.; Gu, B.; Zhang, Z.; Xu, H. *ACS Nano* **2009,** *3,* 3493−3496.

139. Campion, A.; Ivanecky, J. E.; Child, C. M.; Foster, M. *J. Am. Chem. Soc.* **1995,** *117,* 11807−11808.

140. Uetsuki, K.; Verma, P.; Yano, T.; Saito, Y.; Ichimura, T.; Kawata, S. *J. Phys. Chem. C* **2010,** *114,* 7515−7520.

141. McFarland, A. D.; Young, M. A.; Dieringer, J. A.; Van Duyne, R. P. *J. Phys. Chem. B* **2005,** *109,* 11279−11285.

142. Zhao, J.; Dieringer, J. A.; Zhang, X.; Schatz, G. C.; Van Duyne, R. P. *J. Phys. Chem. C* **2008,** *112,* 19302−19310.

143. Le Ru, E. C.; Galloway, C.; Etchegoin, P. G. *Phys. Chem. Chem. Phys.* **2006,** *8,* 3083−3087.

144. van Dijk, T.; Sivapalan, S. T.; DeVetter, B. M.; Yang, T. K.; Schulmerich, M. V.; Murphy, C. J.; Bhargava, R.; Carney, P. S. *J. Phys. Chem. Lett.* **2013,** *4,* 1193−1196.

145. Li, M.; Kang, J. W.; Dasari, R. R.; Barman, I. *Angew. Chem. Int. Ed.* **2014**, *53,* 14115–14119.

146. Doherty, M. D.; Murphy, A.; Pollard, R. J.; Dawson, P. *Phys. Rev. X* **2013,** *3,* 011001 (1-12).

147. Lee, S. J.; Morrill, A. R.; Moskovits, M. *J. Am. Chem. Soc.* **2006,** *128*, 2200−2201.

148. Wang, H.; Levin, C. S.; Halas, N. J. *J. Am. Chem. Soc.* **2005,** *127*, 14992−14993.

149. Fraire, J. C.; Pérez, L. A.; Coronado, E. A. *J. Phys. Chem. C* **2013**, *117*, 23090−23107.

150. Fraire, J. C.; Pérez, L. A.; Coronado, E. A. *ACS Nano* **2012**, *6*, 3441-3452.

151. Angelome , P. C.; Mezerji, H. H.; Goris, B.; Pastoriza-Santos, I.; Pérez-Juste, J.; Bals, S.; Liz-Marzán, L. M. *Chem. Mater.* **2012,** *24*, 1393−1399.

152. Jensen, T. R.; Malinsky, M. D.; Haynes, C. L.; Van Duyne, R. P. *J. Phys. Chem. B* **2000,** *104*, 10549−10556.

153. Kelly, K. L.; Coronado, E.; Zhao, L. L.; Schatz, G. C. *J. Phys. Chem. B* **2003,** *107*, 668−677.

154. Zhang, X.; Hicks, E. M.; Zhao, J.; Schatz, G. C.; Van Duyne, R. P. *Nano Lett.* **2005,** *5*, 1503−1507.

155. Wiley, B. J.; Im, S. H.; Li, Z. Y.; McLellan, J.; Siekkinen, A.; Xia, Y. *J. Phys. Chem. B* **2006,** *110*, 15666−15675.

CHAPTER 2

Hollow Bimetallic Nanoparticles Generated *In Situ* Inside a Polymer Thin Film: Fabrication and Catalytic Application of Silver-Palladium-Poly(vinyl alcohol)

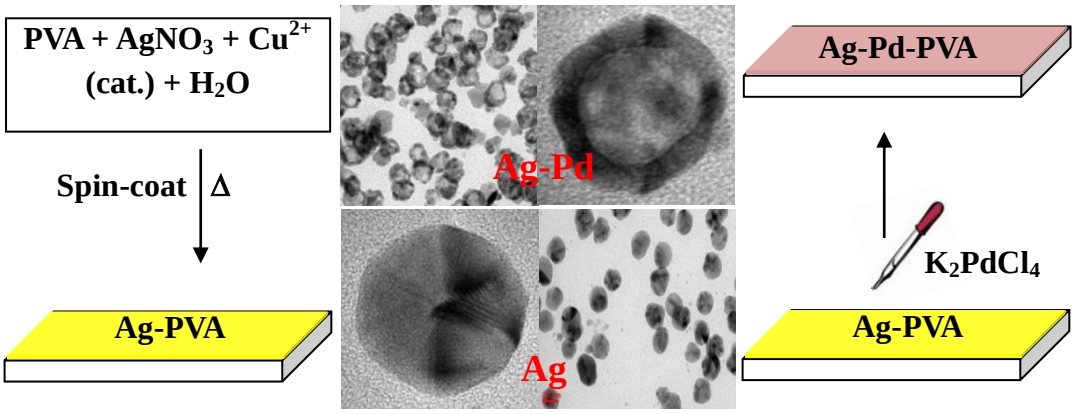

Hollow Ag-Pd nanoparticle-embedded PVA thin film is fabricated by an in situ protocol involving thermal annealing assisted reduction and galvanic displacement, and its catalytic activity is demonstrated.

Paper published

Rao, V. K.; Radhakrishnan, T. P. *J. Mater. Chem. A* **2013**, *1*, 13612-13618.

Scope

This chapter outlines the development of a general approach to the fabrication of bimetallic nanoparticle-embedded polymer thin film by presenting the specific case of generating hollow bimetallic nanoparticles of silver-palladium (Ag-Pd) in situ inside poly(vinyl alcohol) (PVA) thin films by a two-stage process. In the first stage, Ag-PVA is fabricated by mild thermal treatment of a spin-coated thin film, the polymer functioning as the reducing agent for the embedded metal precursor ions as well as the stabilizer for the generated nanoparticles. An important methodology for the formation of relatively larger Ag nanoparticles is also developed. In the second stage, an aqueous solution of potassium palladium chloride (K_2PdCl_4) is spread on this film under ambient conditions, whereupon Pd gets deposited on the Ag nanoparticles through a galvanic displacement reaction and alloys with it. A gradual variation of the concentration of K_2PdCl_4 solution used in the in situ process allowed a systematic demonstration of the evolution of the bimetallic nanoparticles with the eventual formation of hollow particles with Ag-Pd alloy walls. The high catalytic efficiency of the Ag-Pd hollow nanoparticle-embedded PVA thin film is demonstrated by its application in the Suzuki-Miyaura reaction.

2.1 Introduction

The versatility of metal nanoparticles arises from the ease and facility of their synthesis, tunability of their size and shape, unique properties such as the localized surface plasmon resonance (LSPR) extinction that they exhibit, and the strong dependence of these properties on the metal and the size, shape/morphology and assembly of the particles. These attributes lead to potential applications of metal nanoparticles in fields such as electronics, photonics, analytical and environmental sciences, catalysis, biology and medicine, as noted in Sec.1.2.[1-5] As highlighted in Sec.1.3, the presence of two or more types of metals in the same nanoparticle adds the new dimensions of composition and structure to the factors that can be used to tune the

characteristics of the nanoparticles. Bimetallic nanoparticles have attracted great attention in recent times.[6-11] The highly tunable optical properties and the enhanced catalytic efficiencies of bimetallic nanoparticles have led to their extensive application in plasmonics and catalysis.[12-20] As discribed in Sec.1.3.1, popular routes to the fabrication of these versatile nanomaterials involve the chemical reduction of the precursor ions; the two types of metal ions may be reduced concomitantly[21] or in successive steps;[22] some of the methods follow a templated approach.[23] Bio-synthetic processes[24] and thermal decomposition protocols[25] are also commonly used. Other techniques reported for the synthesis of bimetallic nanoparticles include laser ablation,[26] ion implantation,[27] electrochemistry,[28] radiolysis[29] and sonochemistry.[30]

The importance of metal-polymer nanocomposites,[31,32] and the *in situ* fabrication protocol developed in our laboratory using a simple, inexpensive and environmentally benign route,[33] have been described in Sec.1.5. The ease of deployment of the metal-polymer nanocomposte thin film in catalytic applications has been highlighted by qualifying it as a 'dip catalyst', examples being Ag-PVA thin film used in reduction of p-nitrophenol,[34] and Pd-PVA thin film used in C-C bond coupling reactions.[35] In the study presented in this chapter, we have explored the utility of this facile *in situ* approach to the fabrication of bimetallic (Ag-Pd) nanoparticles. Several studies on Ag-Pd alloy nanoparticles have been reported earlier.[15,36-38] We have developed a simple technique for the generation of relatively large Ag nanoparticles in the polymer thin film, followed by the formation of Ag-Pd alloy nanoparticles within the film through an ambient temperature templating approach. The *in situ* approach allowed convenient and systematic monitoring of the different steps in the growth of the hollow bimetallic structure. The high catalytic efficiency of these bimetallic nanoparticles is demonstrated by using the Ag-Pd-PVA nanocomposite thin film as a 'dip catalyst' in the Suzuki-Miyaura coupling reaction.

2.2 Ag-PVA Thin Film

2.2.1 *Fabrication of Ag-PVA Thin Film*

The protocol for the *in situ* fabrication of metal-polymer nanocomposite thin films that was developed earlier[32,33] in our laboratory involves essentially two steps: spin-coating of the polymer thin film with the metal precursor uniformly dispersed within, and thermal annealing during which the metal ions are reduced and the nanoparticles are generated, the polymer acting simultaneously as the reducing agent and stabilizer. PVA has been the polymer of choice in most cases. The Ag-PVA thin film contains nearly monodisperse nanoparticles with sizes that can be tuned from ~ 2-9 nm by controlling the Ag/PVA weight ratio (*x*), in the initial mixture and the thermal annealing conditions.[33] In order to proceed further to fabricate bimetallic nanoparticles, relatively larger Ag nanoparticles which can act as templates are required; the larger size will also facilitate unambiguous structural characterization of the bimetallic systems. An obvious approach to produce larger particles would be to increase the Ag/PVA ratio (*x*); however, we found that this leads to a polydisperse size distribution including smaller ones, possibly due to more extensive nucleation within the polymer film. Increase in the temperature or time of thermal annealing generally resulted in damage of the polymer film. A wide range of variations in the thermal annealing conditions and procedures that we explored, also failed to produce monodisperse, large nanoparticles in the polymer film. In a modified protocol, a high Ag/PVA weight ratio of 0.8 was used and the thermal annealing carried out for a short period of 30 min and the unreduced Ag^+ was washed away using water. Examination of the nanocomposite film revealed only a marginal increase in the size of the Ag nanoparticles to ~12 nm.

We have solved the problem finally by using the general procedure above, but incorporating additionally, very small quantities of Cu^{2+} ions in the initial solution mixture. The protocol followed for the fabrication of the Ag-PVA film is shown schematically as Stage I in Fig. 2.1. The procedure used for the preparation of Ag-PVA thin films using different quantities of Cu^{2+} ions was as follows. Aqueous solutions of

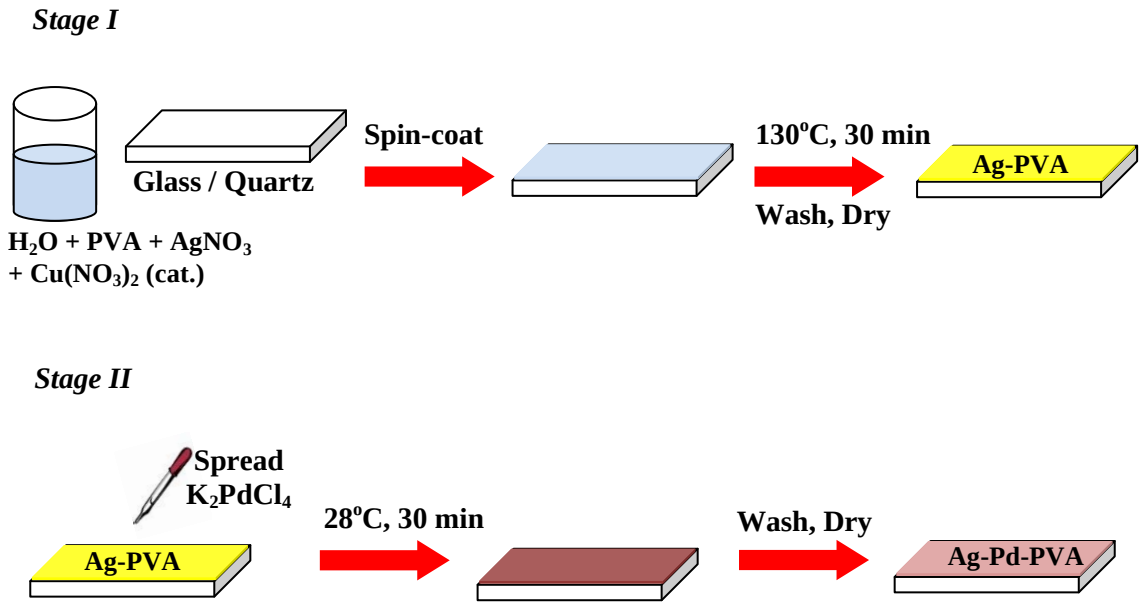

Figure 2.1. *Schematic of the in situ fabrication of Ag-PVA (Stage I) and Ag-Pd-PVA (Stage II) thin films. PVA = poly(vinyl alcohol).*

$AgNO_3$ and PVA were mixed in required proportions; for example, 0.32 g of $AgNO_3$ dissolved in 2.0 mL of water was mixed with 0.25 g of PVA dissolved in 5.0 mL of water to prepare a film with an Ag/PVA weight ratio (x) of 0.8. The appropriate quantity of an aqueous solution of $Cu(NO_3)_2$ was mixed with this solution; the maximum amount of copper used was 1.4 weight % in terms of the total metal (Ag + Cu) content. Glass/quartz substrate for coating the films was cleaned by washing and sonication in isopropyl alcohol and dried. In order to prepare free-standing films for TEM imaging, the substrate was first coated with a few drops of a solution of polystyrene (PS) in toluene (1 g in 8 mL) by spinning at 1000 rpm for 10 s and dried in a hot air oven at 90°C for 15 min. The solution mixture (PVA + $AgNO_3$ + $Cu(NO_3)_2$) was spin-coated on the substrate (glass/quartz/PS coated glass) at 500 rpm for 10 s followed by 6000 rpm for 10 s. The film was heated at 130°C for 30 min and then washed with ~ 1 mL of water and dried under ambient atmosphere.

2.2.2 *Spectroscopy, Microscopy and Chemical Analysis of Ag-PVA Thin Film*

We have measured the thickness of the film using a surface profilometer; it was found to be ~ 150 nm. LSPR extinction spectra and TEM images of the Ag-PVA films fabricated without adding Cu^{2+} and with the addition of different amounts of Cu^{2+} (0.8 – 1.4 % by weight in terms of the total metal content) are shown in Figs. 2.2 and 2.3 respectively. The films fabricated with low percentage of Cu^{2+} show enhanced LSPR extinction, with a slightly red shifted (416 to 425 nm) λ_{max}. With higher Cu^{2+} content the spectrum broadens and exhibits a larger red shift; the λ_{max} for the case with 1.4 % Cu^{2+} is ~ 432 nm. Increase in the size of Ag nanoparticle resulting from the presence of Cu^{2+} is clearly seen in the TEM images; the size (diameter) obtained with 1.4 weight % of Cu^{2+} is ~ 28 nm. The Cu^{2+} ions also appear to impose a faceted structure on the Ag nanoparticles. Identity of the Ag nanoparticles is proved later by electron diffraction pattern and lattice images.

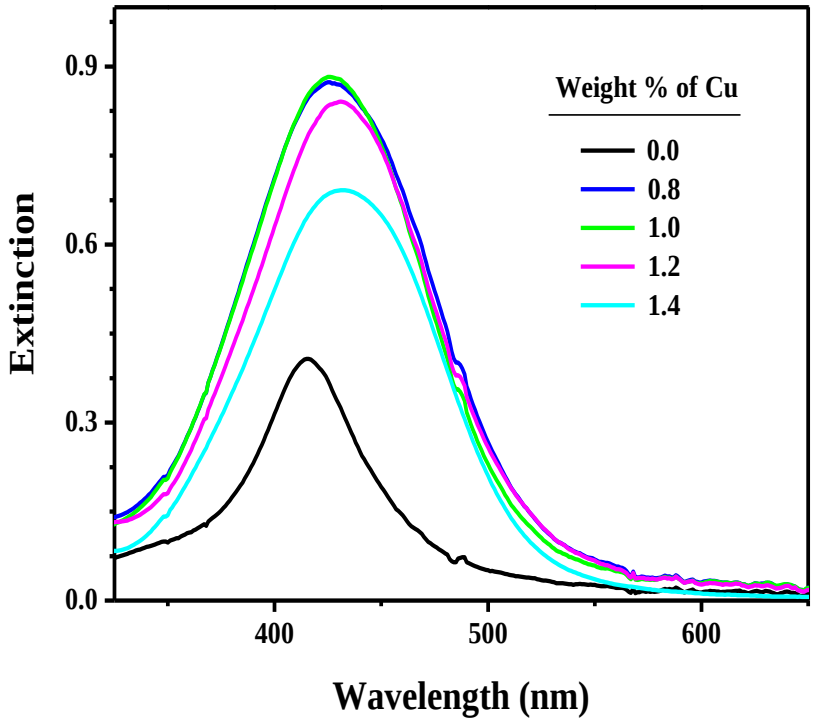

Figure 2.2. *LSPR extinction spectra of Ag-PVA thin films (x=0.8) synthesized in presence of different weight % (in terms of the total metal content) of* Cu^{2+}.

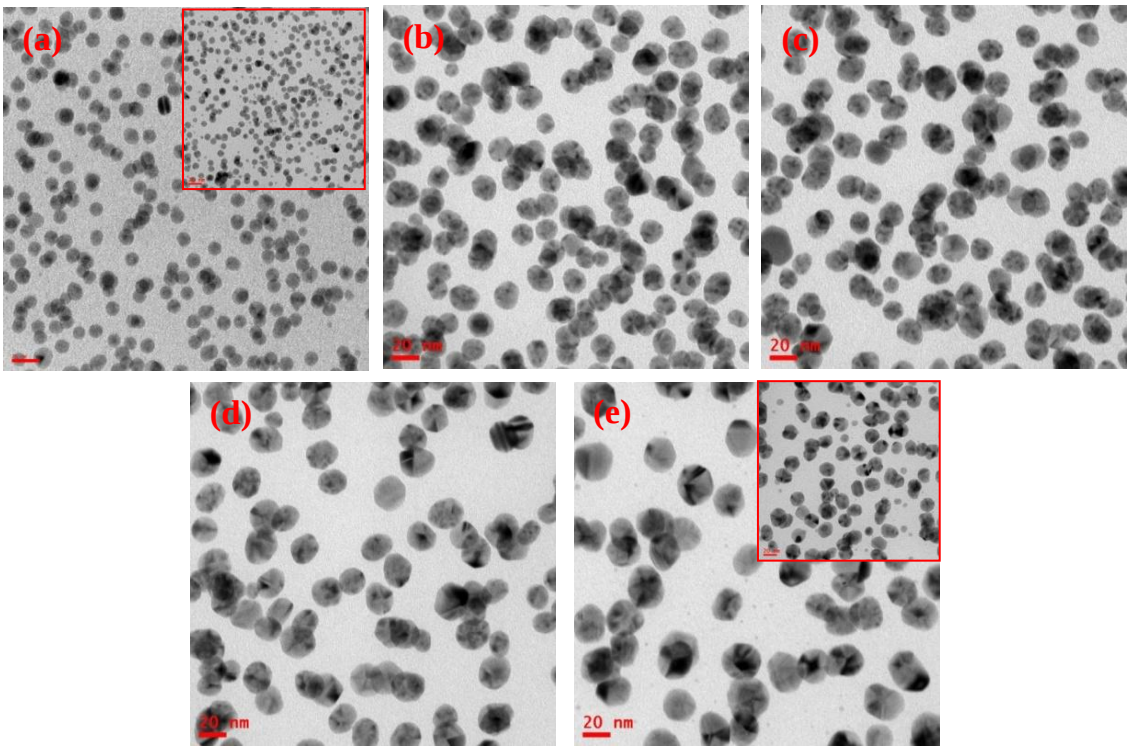

Figure 2.3. *TEM images of Ag-PVA film synthesized in the presence of different weight % of* Cu^{2+}*:* ***(a)*** *0.0,* ***(b)*** *0.8,* ***(c)*** *1.0,* ***(d)*** *1.2 and* ***(e)*** *1.4 (scale bar = 20 nm). The insets of (a) and (e) show the images of the corresponding films prepared under vacuum (scale bar 20 nm).*

Fate of the Cu^{2+} ions is not fully clear. We have checked carefully to see if the few very small particles observed in Fig. 2.3e are copper or copper oxides. However this possibility is ruled as similar particles are seen in the image of the film formed without Cu^{2+}, shown in Fig. 2.3a; further, high resolution image of a ~ 5 nm diameter particle confirms that it is also silver. In an earlier solution synthesis of silver nanoparticles,[39] it was suggested that Cu^{+} formed by the reduction of Cu^{2+} removes oxygen thus preventing the reoxidation of the silver atoms and enhancing the nanoparticle size. In the present case the nanoparticles are generated inside the solid polymer thin film, but under ambient atmosphere. We have carried out control studies involving thermal annealing of the films under vacuum, to explore the effect of atmospheric oxygen on the size of the Ag nanoparticles. TEM images of these films

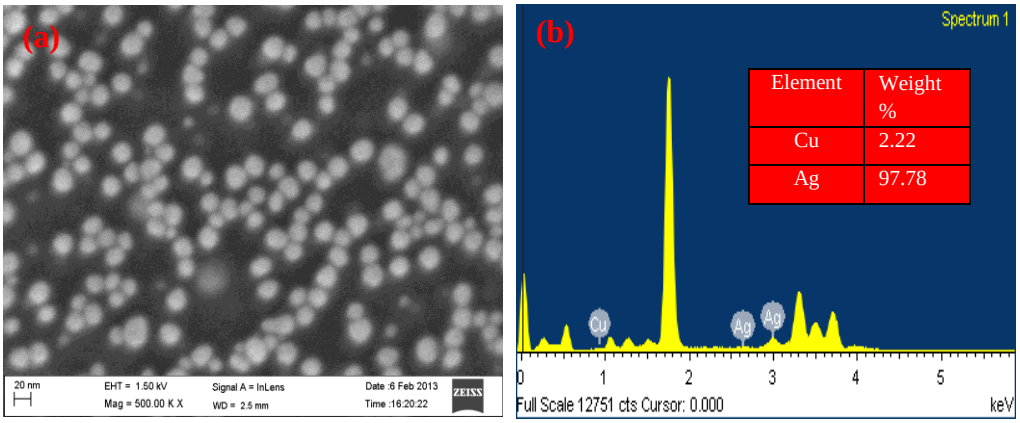

Figure 2.4. ***(a)*** *FESEM image (scale bar 20 nm)and* ***(b)*** *EDX spectrum of Ag-PVA thin film fabricated with 1.4 weight % Cu^{2+}.*

Box 2.1. ICP-OES analysis of the metal content present in Ag-PVA thin film fabricated with 1.4 wt % of Cu^{2+}

The Ag-PVA film coated on a 3.5 × 1.5 cm^2 glass plate was dissolved in 69% nitric acid. The solution was diluted to 100 ml and ICP-OES analysis was carried out. The metal content found are provided below.

Metal	Concentration of the solution analyzed (ppm)	Total weight in the film (µg)	Atom content in the film (µmol)
Cu	0.0174	1.74	0.027
Ag	0.632	63.2	0.59

The Cu/Ag weight (atom) ratio from the ICP analysis is: 0.028 (0.046). This is consistent with the Cu/Ag weight (atom) ratio obtained from the EDX analysis: 0.023 (0.039) (based on the spectra shown in Fig. 2.4b).

Weight of the PVA matrix in the sample analyzed works out to be 86.4 µg (assuming a film thickness of 150 nm, density of PVA to be 1.20 g cm^{-3}, and correcting for the very small volume occupied by the Ag nanoparticles). This implies an Ag/PVA weight ratio of ~0.73 and Cu/PVA weight ratio of 0.02. The Ag/PVA ratio is slightly lower than the weight ratio of 0.8 taken for the synthesis, since the film is heated only for 30 min, leaving some of the Ag^+ unreduced that is subsequently washed away during the last step of the Ag-PVA fabrication.

fabricated under vacuum without (inset of Fig. 2.3a) and with (inset of Fig. 2.3e) the addition of a 1.4 weight % of Cu^{2+} show that the size of Ag nanoparticles obtained are very similar to the similar ones fabricated under ambient atmosphere. The above observations suggest that the Cu^{2+} reduced to Cu^{+} by the PVA may be catalyzing the reduction of Ag^{+} leading to the increase in the size of the particles. This possibility is further supported by the reported observation of the reduction of Cu^{2+} to Cu^{+} by PVA in a solvothermal process.[40] EDXS analysis on the FESEM image (Fig. 2.4) suggests that the amount of copper present is negligible; this is confirmed by the ICP-OES analysis of the Ag-PVA thin film (Box 2.1).

2.3 Ag-Pd-PVA Thin Film

2.3.1 *Fabrication of Ag-Pd-PVA Thin Film*

We have used Ag-PVA films containing the large Ag nanoparticles (~ 28 nm) to synthesize the bimetallic nanoparticles with Pd by performing a galvanic displacement reaction on the Ag nanoparticles (Stage II in Fig. 2.1). The Ag nanoparticles immobilized inside the PVA thin film act as convenient templates for this process. The synthesis procedure of Ag-Pd-PVA thin film was as follows. ~ 0.4 mL of an aqueous solution of K_2PdCl_4 with concentration ranging from 0.05 – 0.25 mM was spread uniformly on the Ag-PVA film and kept for 30 min under ambient temperature (~ 28^{o}C) conditions, inside a closed petri dish to avoid evaporation. The film was then washed with ~ 1 mL of water to remove any unreacted K_2PdCl_4 solution present on the film as well as the byproducts including Ag^{+} and KCl, and dried under ambient atmosphere.

2.3.2 *Spectroscopy, Microscopy and Chemical Analysis of Ag-Pd-PVA Thin Film*

We have investigated the change in the LSPR extinction spectra of the resulting films. Fig. 2.5 clearly shows the decrease of the extinction due to Ag nanoparticles and the appearance of the extinction tail of the Pd nanostructures progressing gradually with

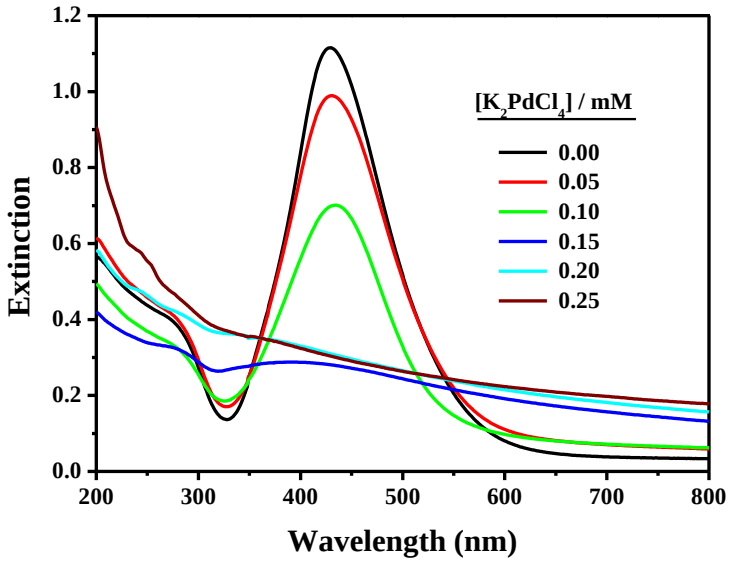

Figure 2.5. *LSPR extinction spectra of Ag-PVA thin film treated with different concentrations (mM) of K_2PdCl_4 solutions.*

increase in the concentration of the K_2PdCl_4 solution. It may be noted that a coating of Pd on Ag can also affect the LSPR extinction of Ag nanoparticles.[13,21,41] The TEM images in Fig. 2.6 illustrate the change in the nanoparticles resulting from the treatment with increasing concentrations of the K_2PdCl_4 solution. The electron diffraction patterns in the insets clearly show the formation of Pd and Ag-Pd crystallites as the concentration of K_2PdCl_4 spread on the film increases; Table 2.1 shows that the diffraction patterns can be indexed to the lattice planes of pure Ag (when not treated with K_2PdCl_4) and to Ag-Pd exclusively when treated with 0.25 mM K_2PdCl_4, with gradual transformation between the extremes. The lattice images of individual particles (Fig. 2.7) show the evolution of their morphology and lattice structures. The faceted structure of the Ag nanoparticles formed in the Cu^{2+} catalyzed reaction is seen clearly in Fig. 2.7a,b. Formation and increase of the hollow space in the particles is revealed in the subsequent images. All particles attain the hollow morphology when the concentration of K_2PdCl_4 solution is ≥ 0.20 mM. The lattice structure observed in these images indicate the formation of small domains of Pd (Fig. 2.7b,c), followed by Ag-Pd alloy when increasing concentrations of the K_2PdCl_4 solution are used (Fig. 2.7c-e). In

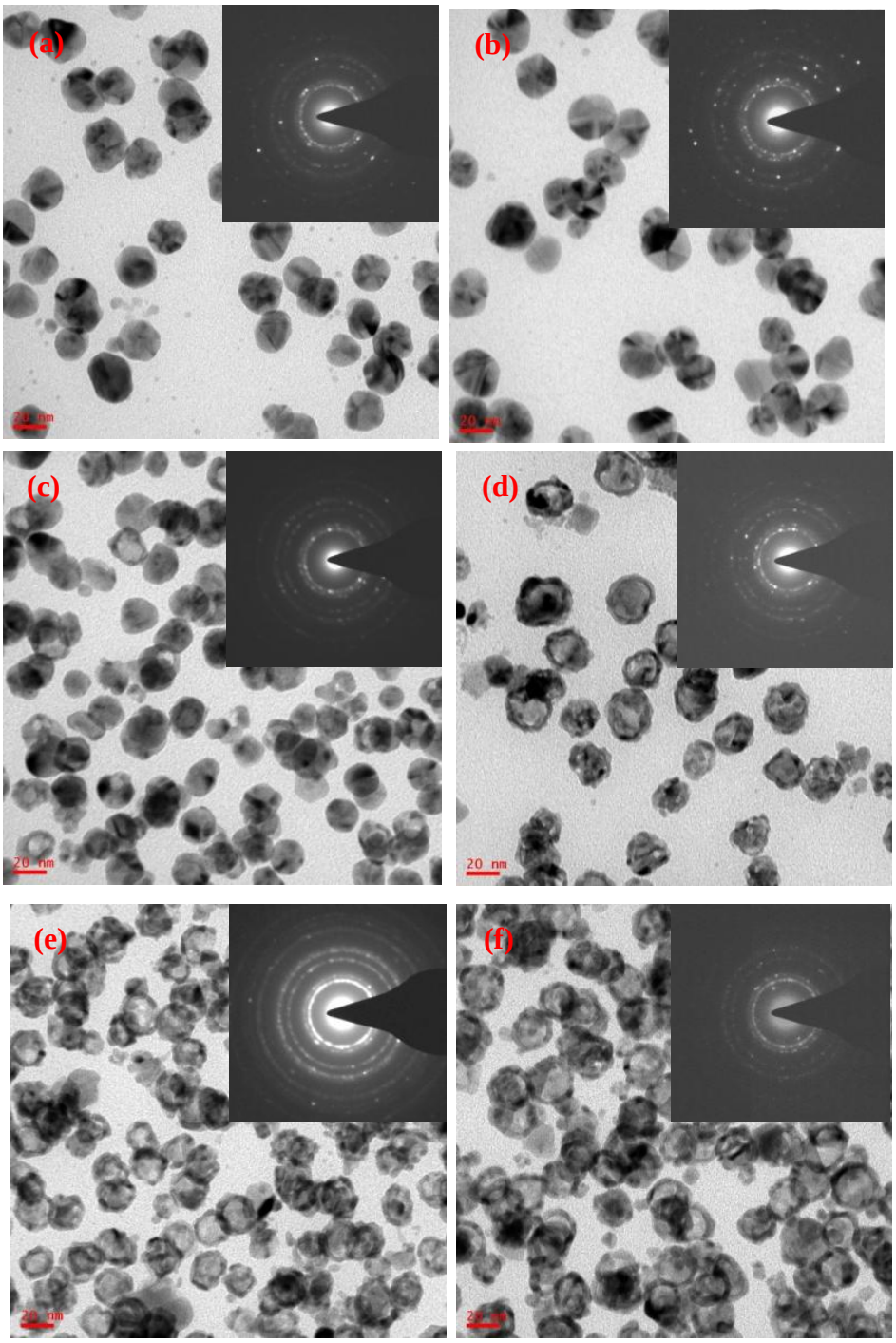

Figure 2.6. *TEM images of Ag-PVA thin films treated with different concentrations (mM) of K_2PdCl_4 solutions :* ***(a)*** *0.00,* ***(b)*** *0.05,* ***(c)*** *0.10,* ***(d)*** *0.15,* ***(e)*** *0.20 and* ***(f)*** *0.25. Scale bar = 20 nm. The insets show the corresponding electron diffraction patterns.*

Table 2.1. *Details of indexing of the electron diffraction patterns shown in Fig. 2.6.*

Image label in Fig. 2.6	**Conc. of K_2PdCl_4 solution used (mM)**	**d (Å)**	**Miller plane h k l**
a	0.00	2.34 2.04 1.44 1.18	1 1 1 (Ag) 2 0 0 (Ag) 2 2 0 (Ag) 2 2 2 (Ag)
b	0.05	2.34 2.03 1.23 2.24	1 1 1 (Ag) 2 0 0 (Ag) 3 1 1 (Ag) 1 1 1 (Pd)
c	0.10	2.33 2.29 2.23 1.99 1.39	1 1 1 (Ag) 1 1 1 (Ag-Pd) 1 1 1 (Pd) 2 0 0 (Ag-Pd) 2 2 0 (Ag-Pd)
d	0.15	2.29 1.97 1.14	1 1 1 (Ag-Pd) 2 0 0 (Ag-Pd) 2 2 2 (Ag-Pd)
e	0.20	2.28 2.00 1.39	1 1 1 (Ag-Pd) 2 0 0 (Ag-Pd) 2 2 0 (Ag-Pd)
f	0.25	2.30 1.98 1.14	1 1 1 (Ag-Pd) 2 0 0 (Ag-Pd) 2 2 2 (Ag-Pd)

the case where 0.10 mM K_2PdCl_4 solution is used, Ag particles containing domains of Pd and Ag-Pd, as well as hollow particles of Ag-Pd containing Pd are observed; the two cases are shown in Figs. 2.7c1 and 2.7c2 respectively. The HAADF and FESEM images (Fig. 2.8) combined with EDX line spectra (Fig. 2.9) confirm the hollow structures and the presence of Ag and Pd in the shell region. The EDX data shows that the Ag-Pd-PVA film prepared using 0.25 mM K_2PdCl_4 has an Ag:Pd ratio

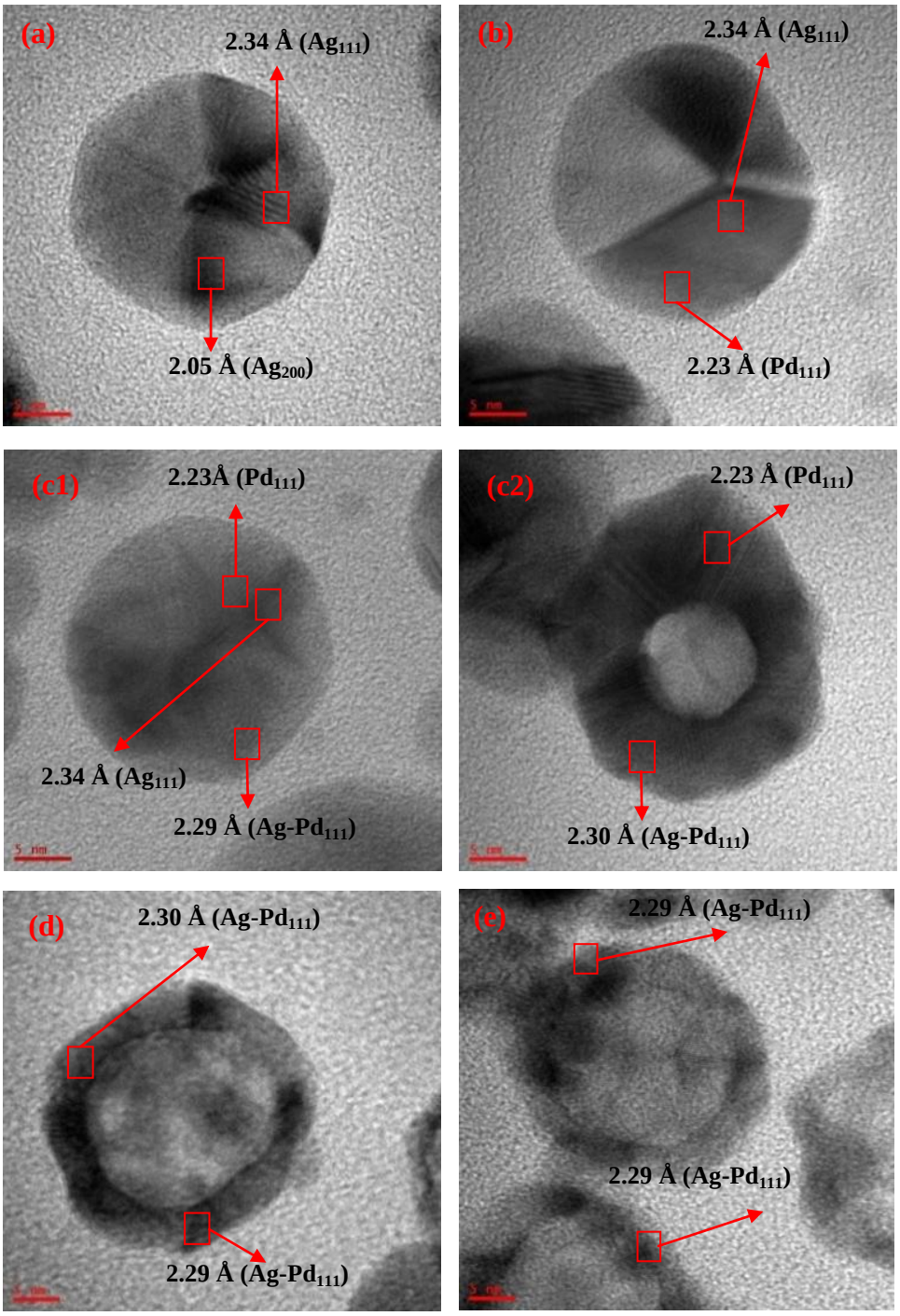

Figure 2.7. *TEM images showing the lattice structures of the nanoparticles in the Ag-PVA thin films treated with different concentrations (mM) of K_2PdCl_4 solutions :* ***(a)*** *0.00,* ***(b)*** *0.05,* ***(c)*** *0.10,* ***(d)*** *0.15 and* ***(e)*** *0.25; in (c), two kinds of particles observed (c1 and c2) are shown. Scale bar = 5 nm.*

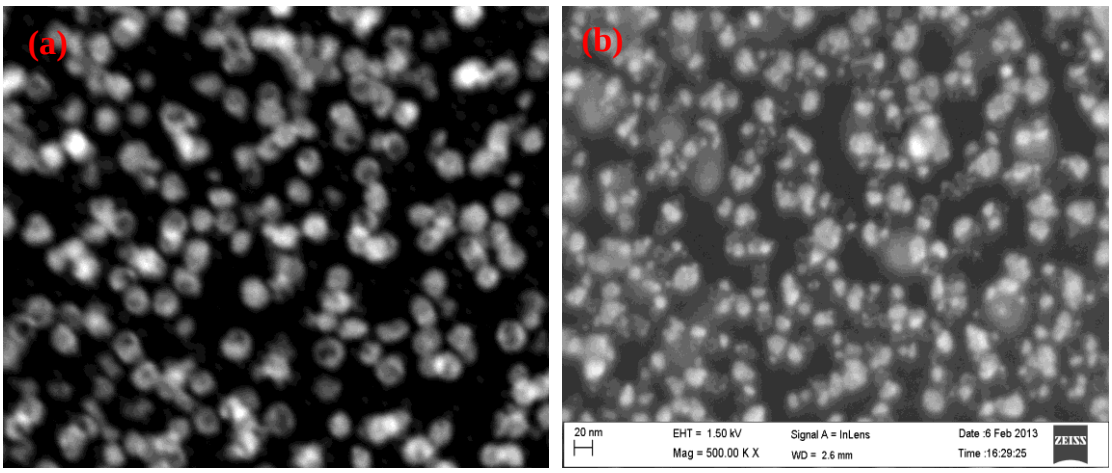

Figure 2.8. ***(a)*** *HAADF and* ***(b)*** *FESEM images (scale bar 20 nm) of Ag-Pd hollow nanoparticles in Ag-Pd-PVA (prepared by treating with 0.25 mM K_2PdCl_4 solution) thin film.*

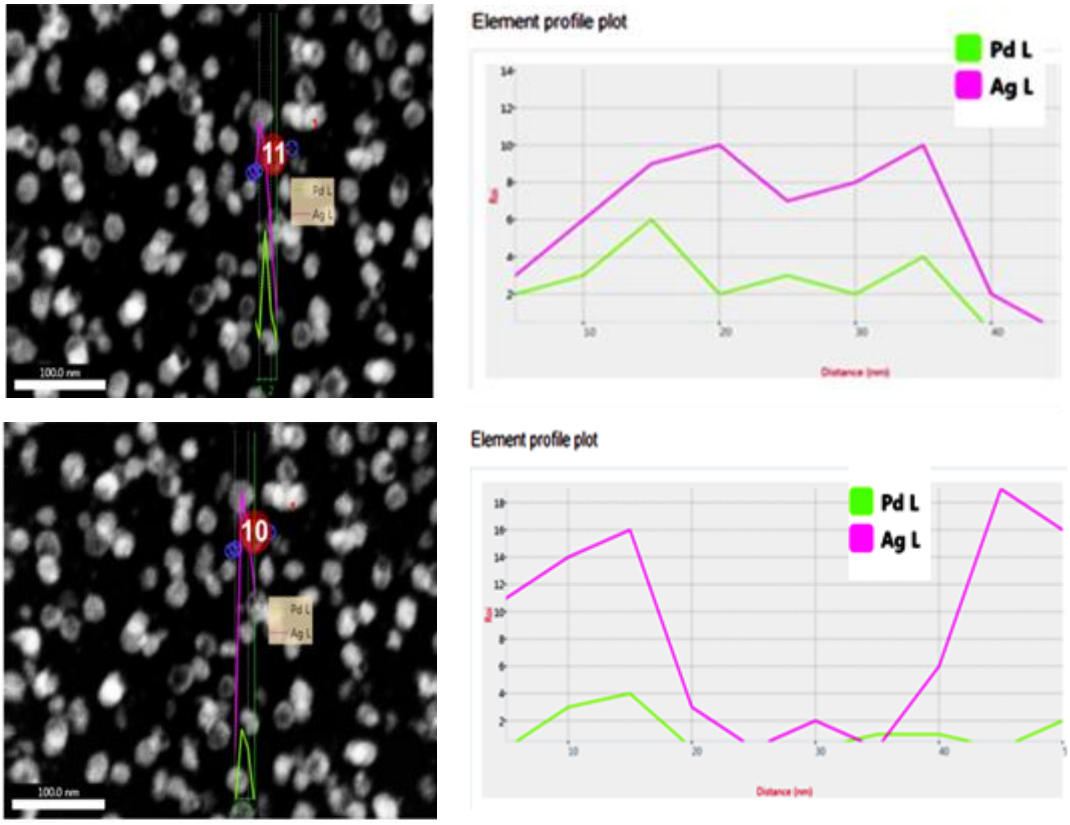

Figure 2.9. *HAADF image with EDX line profile recorded in different directions on the Ag-Pd hollow nanoparticles in Ag-Pd-PVA (prepared by treating with 0.25 mM K_2PdCl_4 solution) thin film.*

Table 2.2. *The Ag/Pd weight ratios inferred from the EDX spectra recorded at different points on the Ag-Pd-PVA thin film fabricated with 0.25 mM K_2PdCl_4 and the average value.*

Position	Weight % of Pd	Weight % of Ag	Ag/Pd weight ratio
1	24.78	75.22	3.04
2	17.00	83.00	4.88
3	14.36	85.64	5.96
4	21.21	78.79	3.71
5	23.00	77.00	3.34
6	21.73	78.27	3.60
		Average	4.09

Box 2.2. ICP-OES analysis of the metal content present in Ag-Pd-PVA thin film

The Ag-Pd-PVA film (concentration of K_2PdCl_4 solution spread = 0.25 mM) coated on a 3.5 × 1.5 cm^2 glass plate was dissolved in 69% nitric acid. The solution was diluted to 100 mL and ICP-OES analysis was carried out. The metal content found are provided below.

Metal	Concentration of the solution analyzed (ppm)	Total weight in the film (µg)	Atom content in the film (µmol)
Pd	0.0881	8.81	0.0828
Ag	0.386	38.6	0.358

The Ag/Pd weight (atom) ratio from the ICP analysis is: 4.38 (4.32).

The catalysis (Suzuki-Miyaura reaction) study employed two Ag-Pd-PVA films (total surface area = 2 × 3.5 × 1.5 = 10.5 cm^2). Therefore the amount of Pd used = 0.165 µmol *ie.* 17.6 µg.

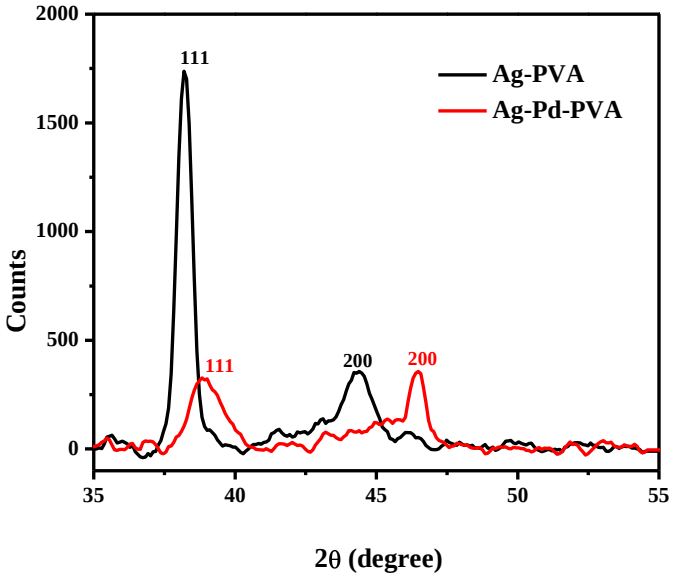

Figure 2.10. *X-ray diffraction patterns of thick films of Ag-PVA and Ag-Pd-PVA prepared by treating with 0.25 mM K_2PdCl_4 solution.*

of ~ 4:1 (Table 2.2); this is consistent with the ratio obtained from the ICP-OES analysis (Box 2.2). X-ray diffraction (XRD) of the Ag-Pd-PVA film (Fig. 2.10) shows clear peak shifts with respect to the Ag-PVA film and the peak positions are in good agreement with the electron diffraction and lattice imaging from TEM discussed above.

The hollow morphology of the bimetallic nanoparticles is similar to that reported for Ag-Au[42] and Ag-Pd[43] prepared through solution routes; it is relevant to note that the protocol we have developed for Ag-Pd is considerably simpler and faster than that reported earlier. The steps involved in the formation of the bimetallic nanoparticles can be visualized based on the spectroscopy and microscopy observations described above; Fig. 2.11 is a schematic illustration of the complete process. The Ag nanoparticles immobilized inside the polymer thin film serve as a sacrificial template for the galvanic displacement reaction with the incoming Pd^{2+} ions. When the concentration of Pd atoms is low, they form small domains on the Ag nanoparticles. At higher concentrations, regions of Ag-Pd alloy are formed. With increasing Pd content, the concentration of Ag atoms near the surface is reduced and the Ag atoms from within the

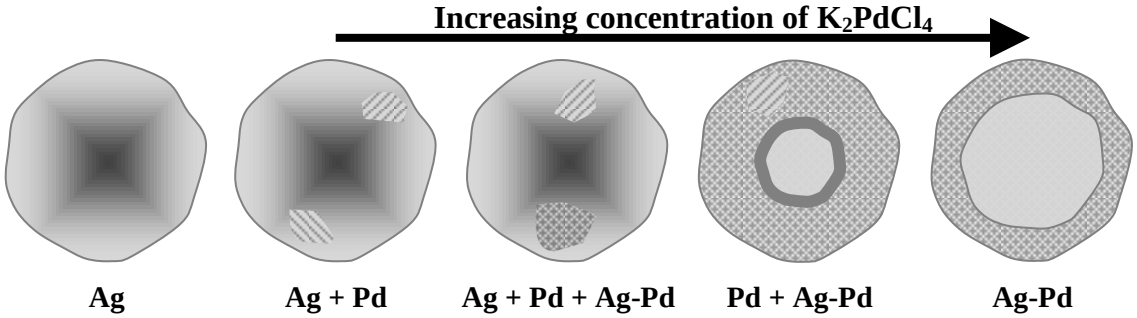

Figure 2.11. *Schematic of the in situ formation of hollow Ag-Pd nanoparticles starting from Ag nanoparticles, inside PVA thin film.*

particle start diffusing outward and forming the alloy. Difference in the rates of diffusion of Ag atoms outward and that of Pd^{2+} ions inward (reminiscent of the Kirkendall effect)[9,44] leads to the formation of hollow spaces within the nanoparticles.

2.4 Catalysis Studies

In order to demonstrate the utility of the bimetallic nanoparticle as a catalyst, we have deployed it in the Suzuki-Miyaura coupling reaction of iodobenzene with phenylboronic acid. The reaction was carried out in a glass tube with a ground glass stopper, provided with a magnet bar for stirring (Fig. 2.12). The procedure is similar to that using the Pd-PVA thin film 'dip catalyst' developed earlier.[35] In a typical reaction, 2 mmol K_2CO_3 was taken in the tube and 1 mmol of iodobenzene, 1.2 mmol of phenylboronic acid and 18 mL of ethanol were added. Two glass plates coated with the Ag-Pd-PVA film (each one having an area of 3.5 × 1.5 cm^2) were placed together, with the films on the exposed faces, and tied together at the ends with a Teflon tape. The catalyst was suspended in the reaction mixture using a Teflon thread hung from the ground glass stopper. The reaction tube was closed and introduced in an oil bath maintained at the desired temperature, typically 80^oC. The reaction mixture was stirred using a magnetic stirrer. Progress of the reaction was monitored by analyzing 0.2 mL samples removed periodically from the reaction mixture, using gas chromatograph-mass spectrometer (GC-MS).

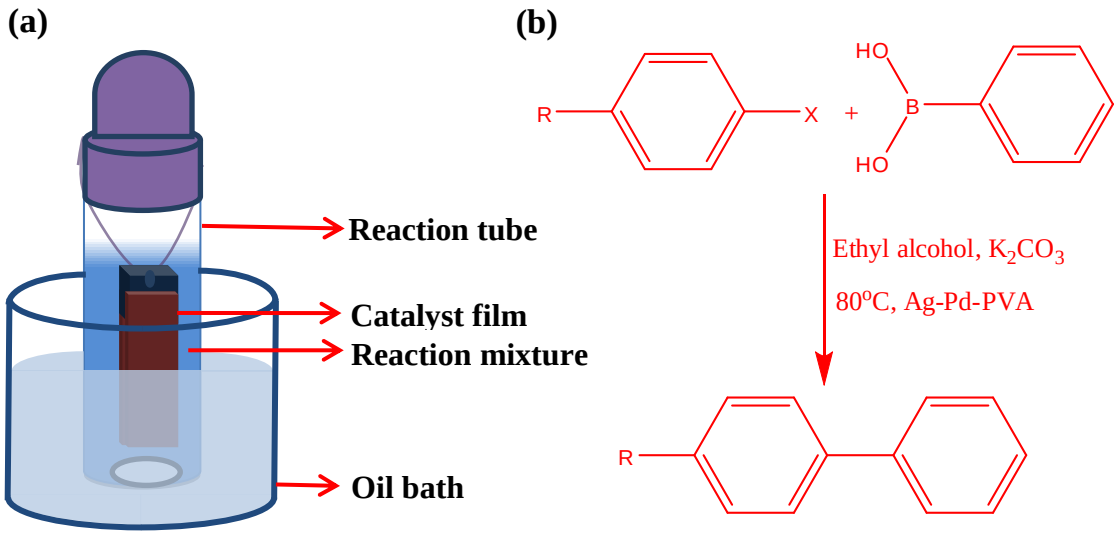

Figure 2.12. ***(a)*** *Schematic of reaction setup used to study the Suzuki-Miyaura reaction using the Ag-Pd-PVA 'dip catalyst';* ***(b)*** *Scheme of the reaction.*

The Pd content in the dip catalyst film of Ag-Pd-PVA was determined by ICP-OES analysis to be ~17.6 µg (Box 2.2). The reaction mixture was heated at 80°C with constant stirring using a magnetic pellet. A 1 mmol scale reaction using this catalyst (0.165 µmol Pd) was completed in ~ 2.5 h. The turn-over number (TON) and turn-over frequency (TOF) for the reaction work out to be 6,061 and 2,424 h^{-1} respectively. These figures are considerably superior to those observed with most of the Pd nanoparticle based catalysts; in particular, it is approximately twice that obtained in one reaction cycle with the Pd-PVA film reported from our laboratory earlier.[43] With the current formulation of the Ag-Pd-PVA thin film, it is not possible to reuse the catalyst efficiently in several cycles; this issue needs to be addressed for realizing practical applications. We have explored the feasibility of using the Ag-Pd-PVA thin film having the same composition as above for the Suzuki-Miyaura reaction with other substrates. While ineffective with chlorobenzene, it is found to catalyze the reaction of bromobenzene as well as its 4-nitro, 4-methoxy and 4-acetyl derivatives. For 1 mmol scale reactions of the latter, the TON and TOF obtained are ~ 2,400 and ~ 800 h^{-1} respectively. It is likely that further optimization of the Ag/Pd and metal/polymer ratios

in these nanocomposite thin films is required to enhance the catalytic efficiency for a wide range of substrates.

2.5 Summary

We have described in this chapter, the optimization of an efficient and facile method for the controlled fabrication of hollow bimetallic Ag-Pd nanoparticles using the *in situ* approach to the fabrication of metal-polymer nanocomposite thin films. A simple technique is developed for the *in situ* synthesis of relatively large Ag nanoparticles, with a fairly narrow size range is achieved by the introduction of catalytic amounts of Cu^{2+}. Exposure of the Ag nanoparticles embedded within the polymer film to K_2PdCl_4 solution under ambient conditions is shown to be a quick, mild and convenient approach to the generation of bimetallic particles through the galvanic displacement reaction; the process is investigated in detail, using spectroscopy, microscopy and diffraction tools. Reaction on the Ag nanoparticles acting as sacrificial templates leads to a hollow morphology which is of special interest in applications such as catalysis. Utility of the hollow bimetallic nanoparticle-embedded polymer thin film as an efficient catalyst for the Suzuki-Miyaura reaction of iodobenzene with phenylboronic acid is demonstrated. The soft-chemical methodology developed for the *in situ* fabrication of alloy nanoparticles within solid polymer films is quite general and can easily be extended to other bimetallic and multimetallic systems, as will be demonstrated in later chapters.

References

1. Katz. E.; Willner, I. *Angew. Chem. Int. Ed.* **2004**, *43*, 6042-6108.
2. Xia, Y.; Xiong, Y.; Lim B.; Skrabalak, S. E. *Angew. Chem. Int. Ed.* **2009**, *48*, 60-103.
3. Mori. K.; Yamashita, H. *Phys. Chem. Chem. Phys*. **2010**, *12*, 14420-14432.
4. Sau, T. K.; Rogach, A. L.; Jackel, F.; Klar, T. A.; Feldmann, J. *Adv. Mater.* **2010**, *22*, 1805-1825.
5. Sevonkaev, I.; Privman, V.; Goia, D. *J. Solid State Electrochem.* **2013**, *17*, 279-297.
6. Major, K. J.; De, C.; Obare, S. O. *Plasmonics* **2009**, *4*, 61-78.
7. Muñoz-Flores, B. M.; Kharisov, B. I.; Jiménez-Pérez, V. M.; Martínez, P. E.; López, S. T. *Ind. Eng. Chem. Res.* **2011**, *50*, 7705-7721.
8. Liu, X.; Liu, X. *Angew. Chem. Int. Ed.* **2012**, *51*, 3311-3313.
9. Gonzalez, E.; Arbiol, J.; Puntes, V. F. *Science* **2011**, *334*, 1377-1380.
10. Ferrando, R.; Jellinek, J.; Johnston, R. L. *Chem. Rev.* **2008**, *108*, 845-910.
11. Logsdail, A. J.; Johnston, R. L. *J. Phys. Chem. C* **2012**, *116*, 23616-23628.
12. Toshima, N.; Yonezawa, T. *New J. Chem*. **1998**, 1179-1201.
13. Chen, J.; Wiley, B.; McLellan, J.; Xiong, Y.; Li, Z. Y.; Xia, Y. *Nano Lett.* **2005**, *5*, 2058-2062.
14. Dhital, R. N.; Kamonsatikul, C.; Somsook, E.; Bobuatong, K.; Ehara, M.; Karanjit, S.; Sakurai, H. *J. Am. Chem. Soc.* **2012**, *134*, 20250-20253.
15. Yang, J.; Yang, J.; Ying, J. Y. *ACS Nano* **2012**, *6*, 9373-9382.
16. Feng, L.; Gao, G.; Huang, P.; Wang, K.; Wang, X.; Luo, T.; Zhang, C. *Nano Biomed. Eng.* **2010**, *2*, 258-267.

17. Puebla, R. A. A.; Ross, D. J.; Nazri, G. A.; Aroca, R. F. *Langmuir*, **2005**, *21*, 10504-10508.

18. Tao, F.; Grass, M. E.; Zhang, Y.; Butcher, D. R.; Aksoy, F.; Aloni, S.; Altoe, V.; Alayoglu, S.; Renzas, J. R.; Tsung, C.; Zhu, Z.; Liu, Z.; Salmeron, M.; Somorjai, G. A. *J. Am. Chem. Soc*. **2010**, *132*, 8697-8703.

19. Wang, F.; Li, C.; Chen, H.; Jiang, R.; Sun, L.D.; Li, Q.; Wang, J.; Yu, J. C.; Yan, C. H. *J. Am. Chem. Soc.* **2013**, *135*, 5588-5601.

20. Tedsree, K.; Li, T.; Jones, S.; Chan, C. W. A.; Yu, K. M. K.; Bagot, P. A. J.; Marquis, E. A.; Smith, G. D. W.; Tsang, S. C. E. *Nat. Nanotechnol.* **2011,** *6*, 302-307.

21. Kim, K.; Kim, K. L.; Shin, K. S.; *J. Phys. Chem. C* **2011,** *115*, 14844-14851.

22. Ferrer, D.; Castro, A. T.; Gao, X.; Guzman, S. S.; Mendez, U. O.; Yacaman, M. J. *Nano Lett.* **2007,** *7*, 1701-1705.

23. Zhang, X.; Zhang, G.; Zhang, B.; Su, Z. *Langmuir* **2013,** *29*, 6722-6727.

24. Senapati, S.; Ahmad, A.; Khan, M. I.; Sastry, M.; Kumar, R. *Small* **2005,** *1*, 517-520.

25. Son, S. U.; Jang, Y.; Park, J.; Na, H. B.; Park, H. M.; Yun, H. J.; Lee, J.; Hyeon, T. *J. Am. Chem. Soc.* **2004,** *126*, 5026-5027.

26. Intartaglia, R.; Das, G.; Bagga, K.; Gopalakrishnan, A.; Genovese, A.; Povia, M.; Fabrizio, E. D.; Cingolani, R.; Diaspro, A.; Brandi, F. *Phys. Chem. Chem. Phys*. **2013,** *15*, 3075-3082.

27. Haug, J.; Dubiel, M.; Kruth, H.; Hofmeister, H. *J. Phys. Conf. Ser.* **2009,** *190*, 012124 (1-4).

28. Cheng, C. Y.; Thiagarajan, S.; Chen, S. M. *Int. J. Electrochem. Sci.* **2011**, *6*, 1331-1341.

29. Mirdamadi-Esfahani, M.; Mostafavi, M.; Keita, B.; Nadjo, L.; Kooyman, P.; Remita, H. *Gold Bull.* **2010**, *43*, 49-56.

30. Gümeci, C.; Cearnaigh, D. U.; Casadonte, D. J.; Korzeniewski, C. *J. Mater. Chem. A* **2013,** *1,* 2322-2330.

31. Heilmann, A. *Polymer Films with Embedded Metal Nanoparticles,* Springer-Verlag, New York, **2002**.

32. Ramesh, G. V.; Porel, S.; Radhakrishnan, T. P. *Chem. Soc. Rev.* **2009,** *38,* 2646-2656.

33. Porel, S.; Singh, S.; Harsha, S. S.; Rao, D. N.; Radhakrishnan, T. P. *Chem. Mater.* **2005,** *17,* 9-12.

34. Hariprasad, E.; Radhakrishnan, T. P. *Chem. Eur. J.* **2010,** *16,* 14378-14384.

35. Hariprasad, E.; Radhakrishnan, T. P. *ACS Catal.* **2012,** *2,* 1179-1186.

36. Zhou, X.; Huang, Y.; Xing, W.; Liu, C.; Liao, J.; Lu, T. *Chem. Commun.* **2008,** 3540-3542.

37. Slanac, D. A.; Hardin, W. G.; Johnston, K. P.; Stevenson, K. J. *J. Am. Chem. Soc.* **2012,** *134,* 9812-9819.

38. Zhang, S.; Metin, Ö.; Su, D.; Sun, S. *Angew. Chem. Int. Ed.* **2013,** *52,* 3681-3684.

39. Yuan, X.; Chen, Y. *Analyst* **2012**, *137***,** 4516-4523.

40. Gong, J.; Luo, L.; Yu, S.; Qian, H.; Fei, L. *J. Mater. Chem.* **2006**, *16*, 101-105.

41. He, J.; Ichinose, I.; Kunitake, T.; Nakao, A.; Shiraishi, Y.; Toshima, N. *J. Am. Chem. Soc.* **2003**, *125***,** 11034-11040.

42. Zhang, Q.; Xie, J.; Lee, J. Y.; Zhang, J.; Boothroyd, C. *Small* **2008**, *4,* 1067-1071.

43. Liu, H.; Qu, J.; Chen, Y.; Li, J.; Ye, F.; Lee, J. Y.; Yang, J. *J. Am. Chem. Soc.* **2012**, *134*, 11602-11610.

44. Wang, W.; Dahl, M.; Yin, Y. *Chem. Mater.* **2013**, *25,* 1179-1189.

CHAPTER 3

In Situ Fabricated Silver/Silver Chloride-Polymer Nanocomposite Thin Film: An Appraisal of the Efficient and Reusable Photocatalyst

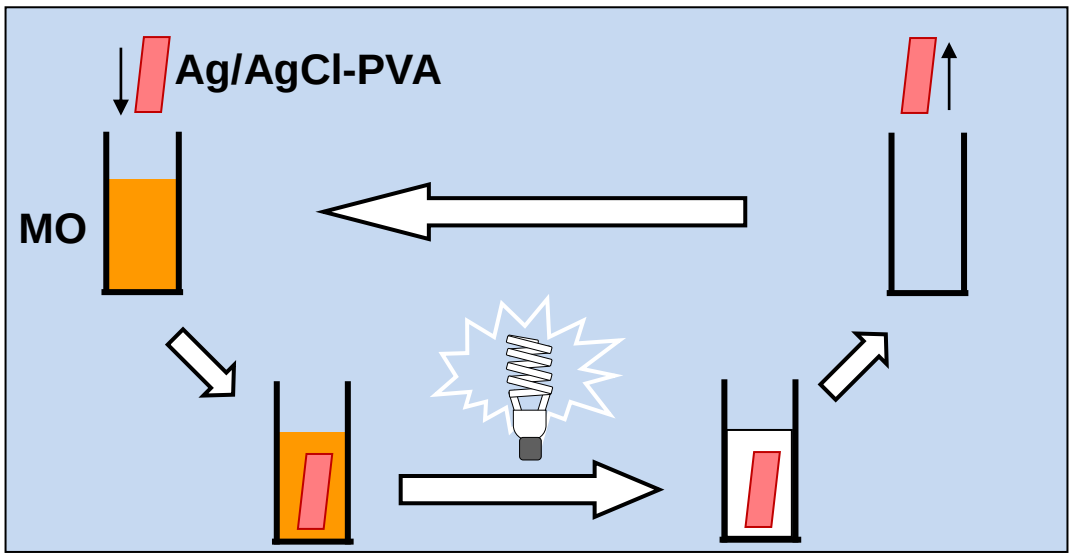

Silver–silver chloride nanocomposite-embedded poly(vinyl alcohol) thin film fabricated through a facile in situ process is shown to be a highly efficient and reusable plasmonic photocatalyst for methyl orange degradation. The thin film 'dip catalyst' could be monitored easily through the recycle runs to unravel the fate of the catalyst.

Paper published

Rao, V. K.; Radhakrishnan, T. P. *Mater. Res. Bull*. **2017**, *87*, 193-201.

Scope

This chapter provides an overview of the development of a general approach for the fabrication of a metal-semiconductor nanoparticle-embedded polymer thin films, its use as a photocatalyst and the in situ monitoring of the catalyst during repeated uses. Silver/silver chloride (Ag/AgCl) nanocomposite is a versatile plasmonic photocatalyst studied extensively in recent times; however, its stability and evolution through catalytic runs have not been explored. We have developed a simple protocol for the in situ fabrication of nanocomposite thin films of Ag/AgCl in poly(vinyl alcohol) (PVA). AgCl-PVA film formed first was photo-irradiated in water to form Ag/AgCl-PVA; the fabrication is monitored through spectroscopy, microscopy and chemical analysis. Photocatalytic application of Ag/AgCl-PVA was demonstrated by its efficient degradation of methyl orange under low power visible light; the 'dip catalyst' nature of the film facilitated several efficient reuses. Significantly, the thin film form facilitated rigorous monitoring of the composite through the reuse cycles; a small but steady evolution of the AgCl to Ag was revealed. In addition to the facile in situ fabrication of an efficient nanocomposite thin film plasmonic photocatalyst, the study projects a convenient approach to evaluate its fate through multiple reuses.

3.1 Introduction

Metal-semiconductor composite nanostructures are prime candidates for photocatalytic applications as described in Sec. 1.4. Nanoparticles of noble metals such as gold, silver and copper in particular, exhibit strong light absorption in the visible regime, and the metal-semiconductor interface promotes facile separation of charge carriers generated through the light absorption; these electrons and holes induce reductive and oxidative reactions leading to efficient photocatalysis. Exploitation of this general principle has led to burgeoning research efforts in the design and fabrication of plasmonic photocatalysts.[1-4]

The versatility of Ag/AgCl composite is illustrated by the wide variety of ways in which it has been fabricated and deployed for the photo-decomposition of typical dye molecules like methyl orange (MO). The most common methodology has been to prepare microparticles, microspheres and microrods of AgCl, followed by photo-irradiation to reduce it partly to Ag.[5-7] Similar strategies have been used to synthesize cubic cage, hollow and frame structures of Ag/AgCl.[8-11]. Laser ablation and chemical reduction have also been employed to form Ag.[12,13] In a slightly different approach, the AgCl nanoparticle formation occurs concomitantly with the formation of Ag, the latter through chemical reduction[14,15] or photo-induced reduction under ambient light[16-18]. Similar protocols have been used to fabricate Ag/AgCl film at the air-water interface,[19] in cellulose acetate membrane,[20] and on *g*-C_3N_4,[21] graphene,[22] and graphene oxide[23] nanosheets. The reverse structures of AgCl/Ag have been formed by first preparing Ag nanoporous films,[24] nanoparticles,[25] nanowires,[26-28] and nanotubes,[29] followed by chemical oxidation of the surface atoms. Many of the studies listed above have explored the possibility of reusing the photocatalyst. However, the colloidal nature of the catalyst and loss during recovery has limited the number of efficient reuses; most have reported 4 or 5, and the maximum is 10,[5,17,19] with significant decrease of efficiency towards the end in some of the cases. Reason for the latter has not been explored in any detail. In all the reported studies, an excess of the photocatalyst has been deployed for the MO decomposition, the catalyst/MO mol ratio being typically ~ 900 – 50. The relatively large quantity used hinders an unambiguous and systematic evaluation of the fate of the catalyst through multiple uses; further, the large size of the composite nanoparticles (0.1 μm – 2 μm) makes it difficult to discern any minor changes occurring in them during the use.

We have developed a simple *in situ* method for the fabrication of Ag/AgCl composite nanostructure within a solid polymer thin film and explored its utility as ‘dip catalyst’ (Sec. 1.6.1) in the photocatalytic process. The ease of fabrication, potential efficiency and reusability, and the convenience of monitoring the thin film catalyst through the reuse cycles form the prime objectives. The initial step was to fabricate AgCl nanoparticles embedded in a PVA thin film through the formation of the salt in an

aqueous solution of the polymer, followed by spin coating. A short thermal annealing of the film at relatively low temperatures, followed by photo-irradiation in water led to the formation of Ag nanoparticles on the AgCl nanostructures within the polymer film. Choice of PVA was dictated by its hydrogel character and swelling in aqueous medium that facilitate ready access of the reaction system to the catalyst without unfavorable leaching of the latter. The Ag/AgCl-PVA thin film was shown to be an efficient plasmonic catalyst for the decomposition of MO, using relatively low power, exclusively visible light from a commercial fluorescent lamp, under ambient conditions. The photocatalyst film could be retrieved from a reaction run, washed and reinserted into the next recycle; ten repeat uses of the same 'dip catalyst' film with high dye decomposition efficiency were demonstrated. Most importantly, the nanocomposite thin film nature allowed systematic monitoring of the photocatalyst between uses, and revealed a small but steady shift in the Ag/AgCl composition. This is consistent with the reduction of AgCl under photo-irradiation[30,31] and electron beam irradiation,[32] and provides a direct view of the gradual inactivation of the catalyst.

3.2 Fabrication of Ag-AgCl-PVA Thin Film

We have carried out several experiments to identify the optimal route to fabricate polymer thin film with embedded nanocomposites of Ag and AgCl. One of the approaches explored was to generate Ag nanoparticles inside the PVA thin film by the *in situ* reduction procedure developed in our laboratory as discussed in Sec. 1.5,[33] followed by the partial conversion of the nanoparticles to AgCl by treating with various chlorinating reagents. Initially, Ag-PVA thin film (Ag/PVA weight ratio, x = 0.8, T = 130^{o}C, t = 30 min) was prepared following the procedure described in Sec. 2.2. The film was then dipped in different reagents like aqueous NaOCl or $FeCl_3$ or exposed to Cl_2 vapors produced by the reaction of $KMnO_4$ with HCl. Formation of AgCl/Ag nanocomposite *in situ* inside the PVA thin film in all the above processes was monitored by the extinction spectra of the Ag-PVA; upon chlorination the extinction due to LSPR of Ag nanoparticles decreases and a new peak or shoulder appears at ~ 255 nm due to the formation of AgCl nanoparticles in the PVA thin film (Fig. 3.1a-c). For

the practical application of photocatalysis, the catalyst film should be stable during the light irradiation. To check the stability of the AgCl/Ag-PVA film, it was subjected to light irradiation for 2 h; whereupon the AgCl was completely reduced back to Ag, which is evident from the increase in the extinction due to Ag and complete disappearance of AgCl band absorption at ~ 255 nm (Fig. 3.1d). Therefore, the AgCl/Ag-PVA was found to be unsuitable for photocatalytic applications.

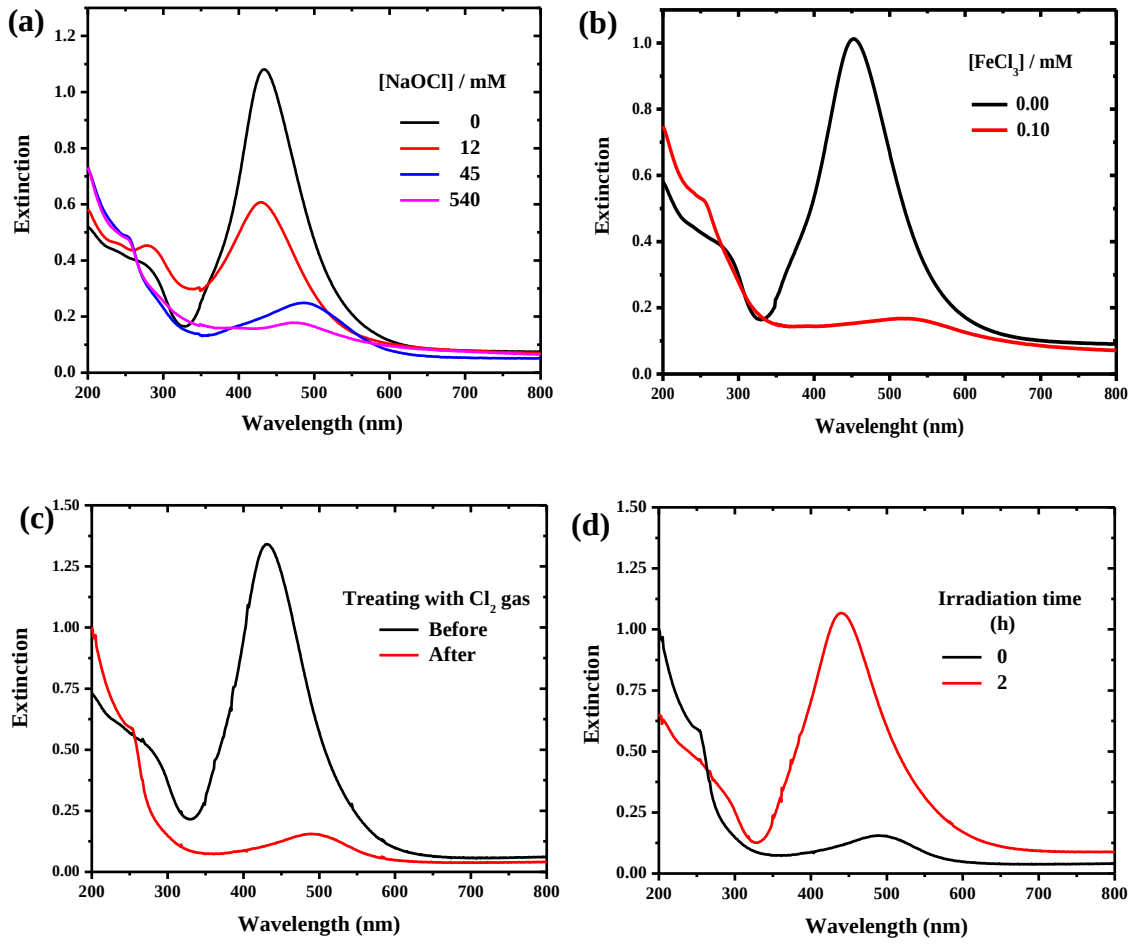

Figure 3.1. *Extinction spectra of AgCl/Ag-PVA thin film fabricated by treating Ag-PVA (x = 0.8) film with aqueous solutions of* ***(a)*** *NaOCl,* ***(b)*** *$FeCl_3$ and* ***(c)*** *Cl_2 vapors; and* ***(d)*** *AgCl/Ag-PVA thin film under photo-irradiation.*

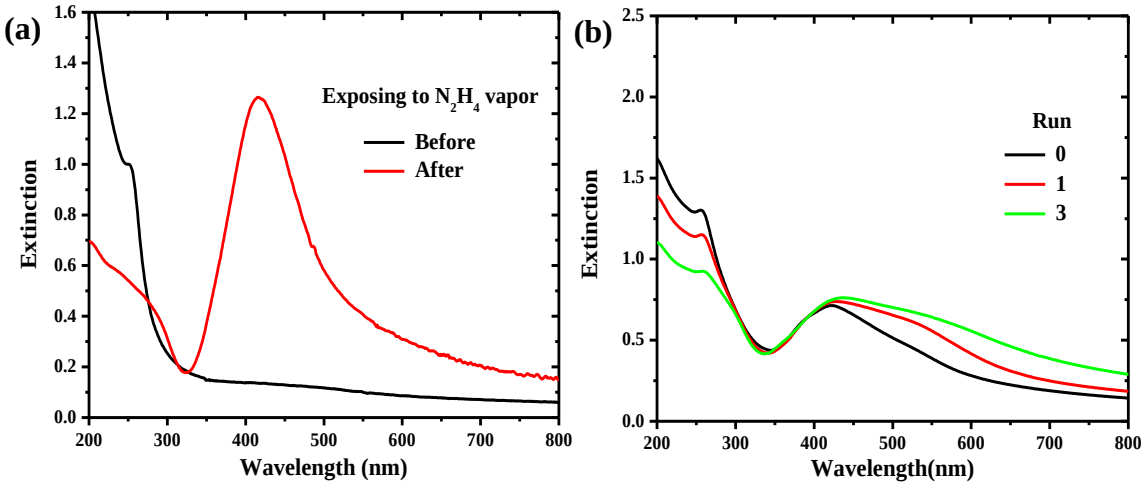

Figure 3.2. *Extinction spectra of **(a)** AgCl-PVA thin film treated with hydrazine and **(b)** Ag/AgCl-PVA thin film (obtained using NaCl) during a few reuses in photocatalysis.*

We then explored the alternate approach of preparing AgCl nanoparticles embedded in a polymer film and converting it partially to Ag. AgCl nanoparticles were generated by mixing $AgNO_3$ with NaCl or HCl (1:1 mol ratio) in an aqueous solution of PVA and spin-coating the film followed by heating at 130^{o}C for 30 min. Subsequently, reduction of the AgCl by chemicals such as hydrazine (N_2H_4) vapor as well as photo-irradiation was investigated. Upon N_2H_4 vapor exposure for 5 min, the AgCl was completely converted to Ag; disappearance of the peak at ~ 250 nm and simultaneous appearance of peak at 415 nm due to the LSPR of Ag nanoparticles (Fig. 3.2a) were observed. Photo-irradiation of the AgCl-PVA film (prepared by $AgNO_3$ and NaCl in 1:1 mol ratio) immersed in water, for 5 h by two 85W compact fluorescent lamps, produced Ag/AgCl nanocomposite. However, the film obtained was unstable and showed signs of degradation within a couple of runs of photocatalysis; this was attributed to the solubility of the PVA thin film because of the absence of cross-linkage in the PVA. Fig. 3.2b shows the drastic decrease in absorbance of AgCl within three runs; this indicates that a fraction of the AgCl converts to Ag, and some leaching out from the film. These experiments ruled out the feasibility of using hydrazine as a reducing agent or NaCl as the chloride source in the two step synthesis of Ag/AgCl-PVA thin film photocatalyst.

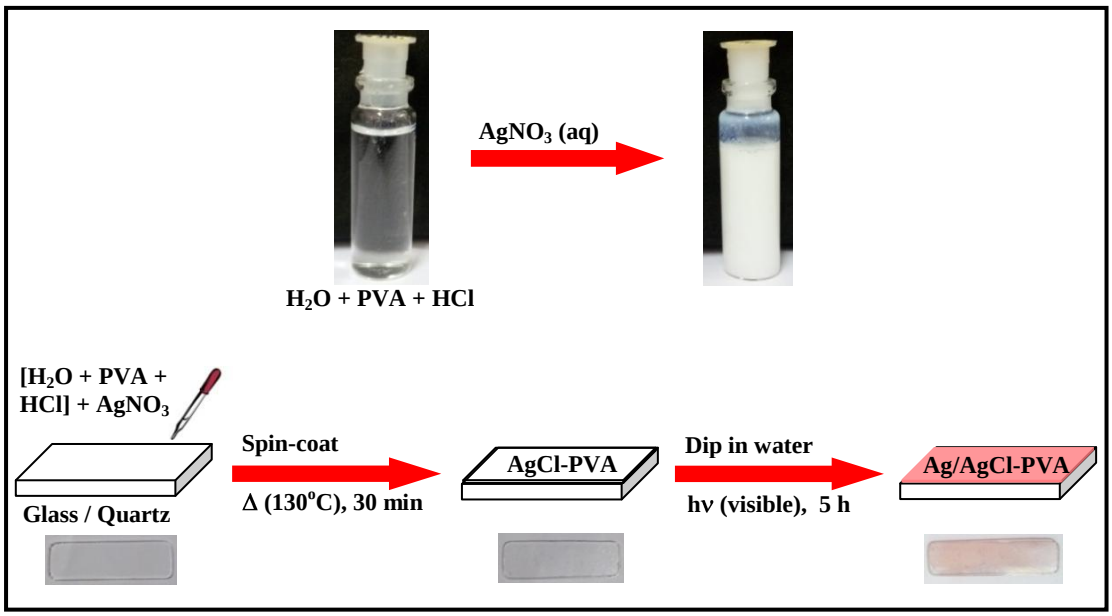

Figure 3.3. *Fabrication of AgCl-PVA followed by Ag/AgCl-PVA thin film; photographs of the solutions and films on quartz substrate (along with the schematic of the protocol) are shown.*

We have finally adopted the optimal protocol (Fig. 3.3) that consists of (i) fabrication of AgCl-PVA by spin coating an aqueous solution of (PVA+HCl)+$AgNO_3$ followed by thermal treatment, and (ii) photo-irradiation of AgCl-PVA in water to yield Ag/AgCl-PVA. For the specific case of Ag/PVA weight ratio, x = 1 and Ag:Cl mol ratio = 1:1, 0.45 g of PVA dissolved in 9.0 ml of water was mixed with 0.36 ml of 12 M HCl (4.32 mmol), stirred for 5 min and 0.72 g of $AgNO_3$ (4.24 mmol) dissolved in 1.5 ml of water was added to yield a pale white dispersion (Fig. 3.3); protected from light, stirring was continued for 30 min. The AgCl formed, remained in a stable colloidal state in the presence of PVA. The AgCl-PVA solution was spin-coated on glass/quartz substrate at 500 rpm for 10 s followed by 3000 rpm for 10 s. Subsequently, the film was heated at 130^{o}C for 30 min in a hot air oven under ambient atmosphere. It is pertinent to note that mixing HCl with PVA in solution and the thermal treatment of the AgCl-PVA film in the first stage, possibly facilitate partial cross-linking of the polymer matrix, leading to enhanced stability of the final 'dip catalyst' film which does not show any leaching through repeated uses. The AgCl-PVA thin film on glass/quartz substrate,

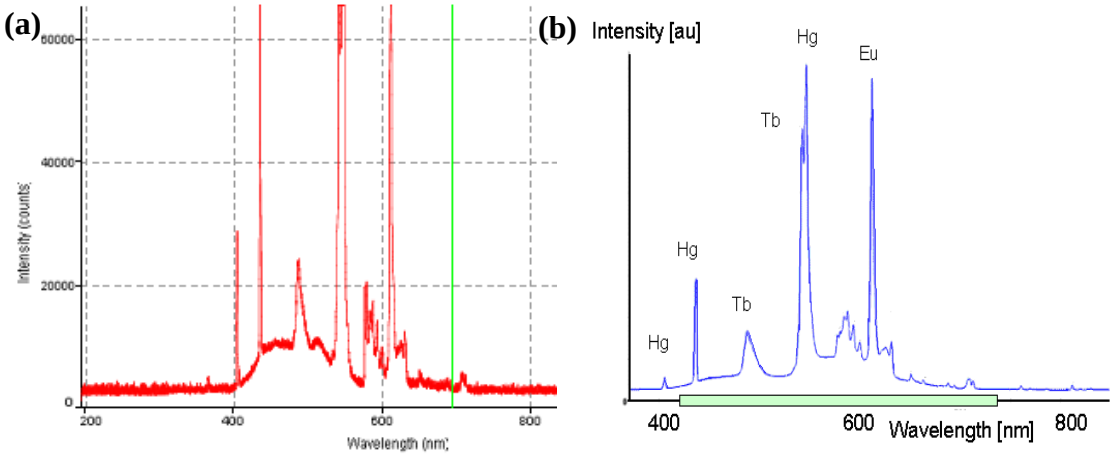

Figure 3.4. ***(a)*** *Emission spectra of the compact fluorescent lamp used in the fabrication of Ag/AgCl-PVA as well as its photocatalytic application and* ***(b)*** *reported spectrum of the lamp (adapted from http://www.tf.uni-kiel.de/matwis/amat/admaten/kap5/backbone/r526.html)*

was immersed in water and irradiated with two commercial 85 W compact fluorescent lamps for 5h; the lamp has no emission in the UV region (lamp profile is shown in Fig. 3.4). The Ag/AgCl-PVA film formed was removed and dried under vacuum.

3.3 Spectroscopy, Microscopy and Chemical Analysis of AgCl-PVA and Ag/AgCl-PVA Thin Films

UV-visible absorption spectrum of the AgCl-PVA film formed in the first stage shows the characteristic semiconductor band absorption rising below 300 nm with a shoulder peak at ~ 255 nm (Fig. 3.5a). These spectra resemble those reported for AgCl nanoparticles formed in emulsions and polymer solutions[13,34-36] and clearly indicate the formation of the nanoparticles inside the PVA thin film. Tauc plots (Fig. 3.5b,c) reveal a direct band gap of 5.11 eV and an indirect band gap of 3.21 eV for AgCl, close to the values reported earlier;[13,36-38] the shoulder peak at 4.86 eV may be attributed to an excitonic absorption.

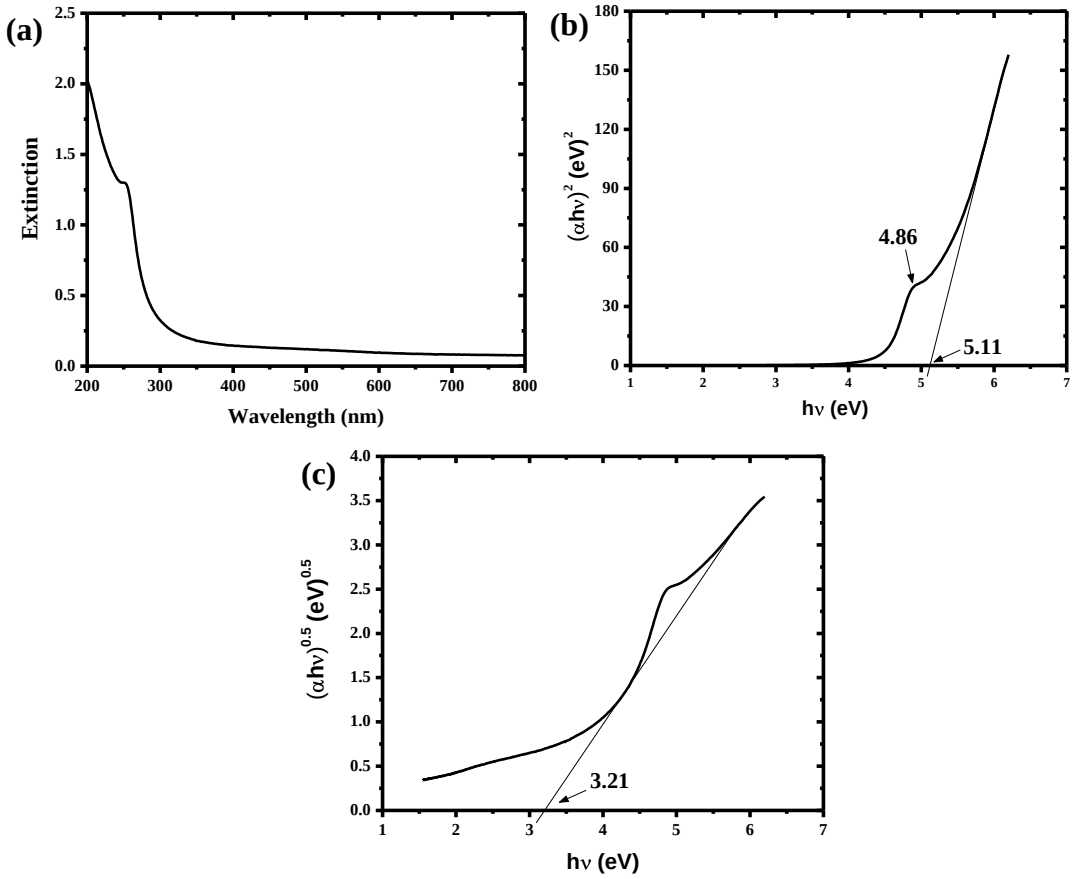

Figure 3.5. (a) *Extinction spectrum of AgCl-PVA film; and Tauc plots for the* ***(b)*** *direct and* ***(c)*** *indirect band gap of the AgCl (an approximate interpolation across the exciton peak is used to evaluate the gap).*

The dry AgCl-PVA film is stable under extended photo-irradiation by visible light, with no discernible change in its absorption spectrum (Fig. 3.6a). However, when the film immersed in pure water was irradiated with visible light (similar to some of the reported methods),[39] Ag nanoparticles were generated inside the film, as seen from the LSPR extinction appearing in the spectrum, growing with time and saturating in ~ 5 h (Fig. 3.6b). The weak absorption of AgCl extending slightly into the visible range may initiate the process; the initial Ag nanoparticles formed could enhance the light absorption and through electron transfer, catalyze further reduction, as discussed later. It is likely that the aqueous medium with its high dielectric constant reduces the recombination of the charge carriers photo-generated by the indirect band gap

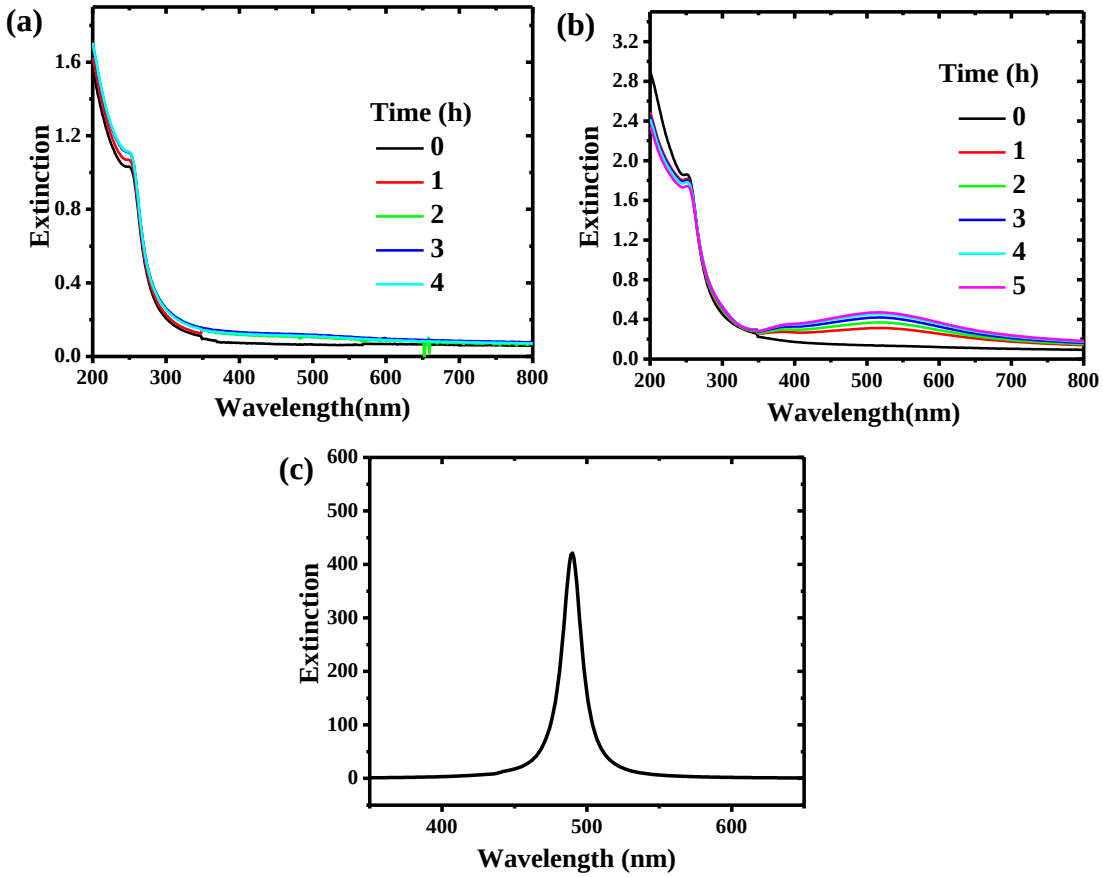

Figure 3.6. *Extinction spectrum of AgCl-PVA films irradiated by two 85 W compact fluorescent lamp in **(a)** dry state, **(b)** immersed in water, recorded at different time intervals and **(c)** calculated Mie scattering spectrum for Ag in an AgCl environment.*

Table 3.1. *Atom % of Ag and Cl in the AgCl and Ag/AgCl-PVA thin films fabricated, estimated using ICP-OES/ IC, EDX (TEM) and EDX (FE-SEM) analysis; data for the Ag/AgCl-PVA after several uses in the photocatalytic reaction are provided.*

Thin film		Mol ratio Ag:Cl					
		ICP-OES/IC		TEM-EDX		FESEM-EDX	
		Ag	Cl	Ag	Cl	Ag	Cl
AgCl-PVA		57	43	53	47	51	49
Ag/AgCl-PVA	before use	65	35	55	45	55	45
	after 1 use	-	-	59	41	63	37
	after 5 uses	78	22	67	33	65	35
	after 7 uses	82	18	-	-	-	-
	after 10 uses	85	15	-	-	-	-

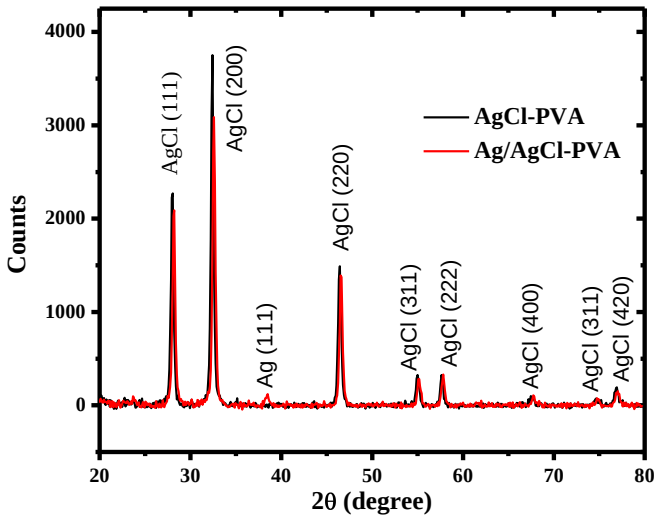

Figure 3.7. *X-ray diffraction patterns of AgCl-PVA and Ag/AgCl-PVA thin films.*

absorption, facilitating the reduction of Ag^+ ions. LSPR extinction of Ag nanoparticles in aqueous medium typically has λ_{max} at ~ 400 nm. Shift of the peak in the present film to ~ 500 nm is likely to be due to the AgCl environment; this is supported by a Mie scattering model calculation of the LSPR spectrum (Fig. 3.6c) for a Ag sphere of 10 nm radius with an AgCl environment (refractive index 2.06).[40] It should also be noted that when strong reducing agents like hydrazine is used, the reduction of AgCl is complete, and the resulting Ag nanoparticles show the extinction maximum at ~ 415 nm (Fig. 3.2a). Change in the AgCl absorption (Fig. 3.6b) accompanying the formation of Ag is small, suggesting that it is primarily the Ag^+ ions adsorbed on the AgCl nanoparticles or present in the polymer thin film that are reduced to form Ag nanoparticles. This is supported by the elemental analysis (using ICP-OES and IC) of the film before and after the irradiation (Table 3.1). Different kinds of chemical analysis showed that the AgCl-PVA has an Ag:Cl ratio slightly higher than 1:1 suggesting the presence of additional Ag^+ than that present in AgCl; the Ag/AgCl-PVA shows an Ag:Cl ratio of ~ 2:1, equivalent to ~ 1:1 ratio of Ag:AgCl (Table 3.1). X-ray diffraction pattern recorded for the AgCl-PVA thin film before and after irradiation in water are shown in Fig. 3.7. The initial pattern corresponds to crystalline AgCl and the emergence of the additional peak

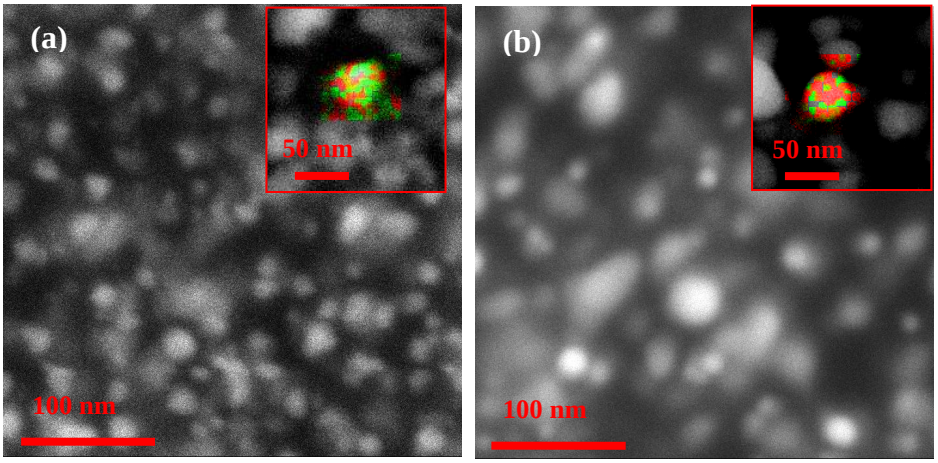

Figure 3.8. *FESEM images of **(a)** AgCl-PVA thin film and **(b)** Ag/AgCl-PVA thin film; scale bar = 100 nm. EDX spectra based mapping of Ag (red) and Cl (green) in single particles is shown in the insets.*

at $2\theta = 38.5^{o}$ for the film after irradiation indicates the formation of Ag nanoparticles (see also the electron diffraction analysis below).

FESEM and TEM imaging combined with EDX spectroscopy and electron diffraction allowed further characterization of the Ag/AgCl nanostructures formed in the synthesis and their status following catalytic application to be discussed later. Fig. 3.8a,b show the FESEM images of the AgCl-PVA film before and after irradiation. Nearly spherical particles with diameters ~ 10 – 50 nm are seen in the AgCl-PVA thin film; EDX data reflecting the composition in the image area shows an Ag:Cl ratio of 1:1, and the mapping shows the particles to be AgCl. Upon irradiation, some larger particles are formed, presumably due to the formation of Ag; the EDX analysis indeed shows an enhancement of the Ag:Cl ratio (Table 3.1),[31] which is also reflected in the mapping. Increase in Ag:Cl ratio results from the decrease in the Cl content relative to Ag in the film, which may be understood as follows. Reduction of AgCl to Ag during the irradiation of AgCl-PVA film immersed in water is accompanied by the oxidation of OH^- in water and leaching of Cl^- out of the film to form HCl. This is confirmed by the decrease in the pH of the aqueous medium down to ~3.8, and the formation of appreciable Cl^- content in it (tested by adding $AgNO_3$) as the photo-irradiation proceeds.

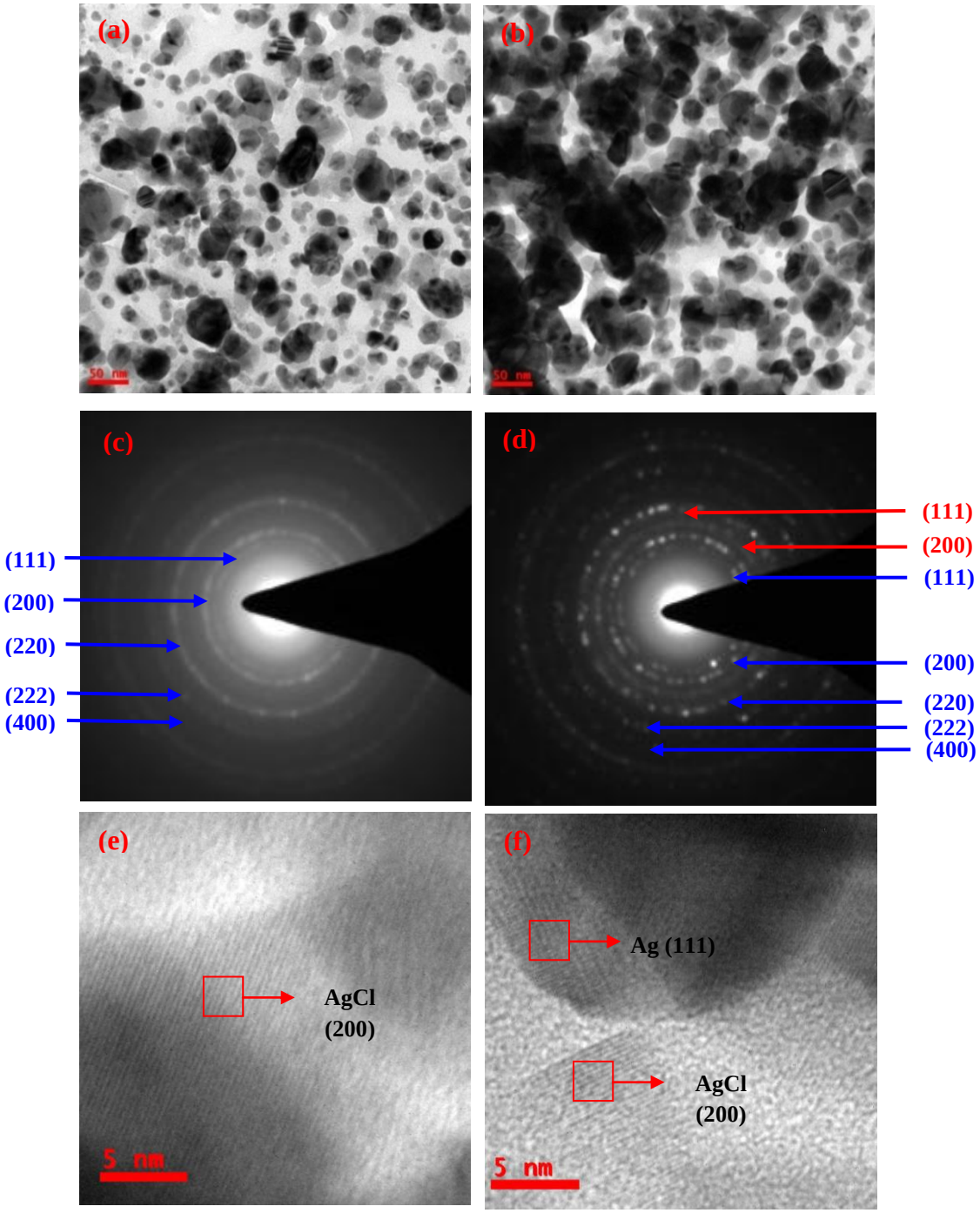

Figure 3.9. *TEM images (scale bar = 50 nm) of* ***(a)*** *AgCl-PVA and* ***(b)*** *Ag/AgCl-PVA thin films;* ***(c)*** *and* ***(d)*** *the corresponding electron diffraction patterns (the diffraction spots are indexed to AgCl (blue) and Ag (red) nanoparticles);* ***(e)*** *and* ***(f)*** *the corresponding lattice images (scale bar = 5 nm) (relevant lattice planes observed in the high resolution images are indicated).*

Fig. 3.9a,b show the TEM images of the nanocomposite thin films; the changes observed upon irradiation are consistent with the FESEM images. Further support for the formation of Ag nanoparticles is obtained from the electron diffraction patterns; while Fig. 3.9c shows diffraction exclusively from cubic AgCl (JCPDS file no: 02-0848): 3.18 Å (1 1 1), 2.78 Å (2 0 0), 1.94 Å (2 2 0), 1.58 Å (2 2 2), and 1.38 Å (4 0 0); Fig. 3.9d shows the presence of AgCl and Ag; the diffraction can be indexed to cubic Ag (JCPDS file no: 01-1164): 2.35 Å (1 1 1), 2.03 Å (2 0 0) and 1.43 Å (2 2 0) along with that of AgCl. The higher magnification TEM images in Fig. 3.9e,f reveal lattice spacing values consistent with the observations from the electron diffraction patterns; notably the Ag and AgCl nanoparticles in the Ag/AgCl-PVA film are in intimate contact. EDX data collected with the TEM images are consistent with that discussed in the case of the FESEM images (Table 3.1). The electron microscopy images together with the EDX and electron diffraction analysis thus confirm the two stages of fabrication of the nanocomposite thin films, AgCl-PVA followed by Ag/AgCl-PVA, the latter with ~ 1:1 ratio between Ag and AgCl, consistent with the ICP-OES and IC analysis.

3.4 Photocatalysis Studies

We have investigated the photocatalytic activity of Ag/AgCl-PVA thin film in the MO degradation under visible light irradiation. A schematic of the experimental setup is shown in Fig. 3.10. The photocatalytic reaction was carried out in a glass tube, equipped with a magnet bar for stirring, placed in a glass container provided with water circulation jacket, and the assembly was placed on a magnetic stirrer. Two 85 W fluorescent lamps (same as those used in the fabrication of the catalyst film) were placed on either side of the reaction setup at a distance of ~ 8 cm. The entire assembly was placed inside an enclosure.

In a typical reaction, 4 ml of a 10 μM aqueous solution of MO was taken in the reaction tube and four quartz plates coated with the Ag/AgCl-PVA film (each 4 cm^2) were placed in it; the total amount of catalyst is 7 μmol (Box 3.1). The reaction system

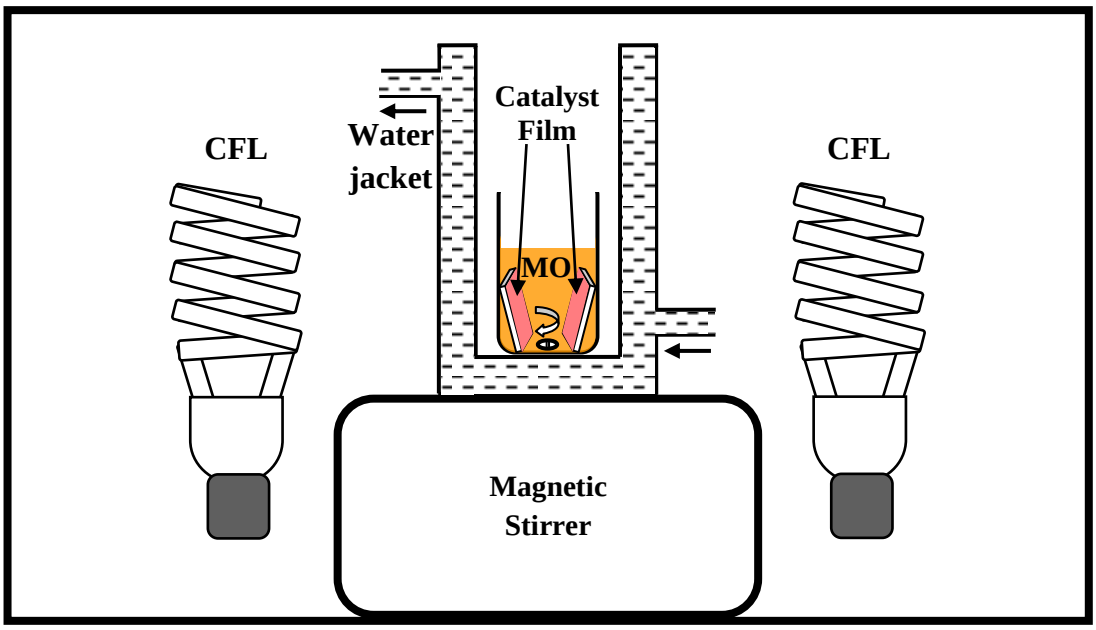

Figure 3.10. *Schematic of the photocatalysis experiment setup. (CFL = Compact fluorescent lamp)*

was irradiated for 60 min with constant stirring; the power available at the reaction mixture was measured using a calibrated photoresistor and found to be 100 mW/cm^2. The jacket of circulating water ensured that no thermal contribution to the reaction occurred, as confirmed by monitoring the temperature of the reaction mixture, which was found to remain at ~ 28^{o}C. Progress of the reaction was followed by recording the absorption spectrum of the MO solution at regular time intervals; there is no interference from catalyst as it is confined in the polymer film, and no leaching occurs as proved by monitoring the Ag/AgCl-PVA catalyst film through repeat uses, using spectroscopy and microscopy. After a reaction run, the catalyst film was simply taken

Box 3.1. Amount of catalyst used in the photocatalytic degradation of MO

Weight of Ag in two films (each 4 cm^2) determined by ICP-OES = 379 μg

Weight of Cl in two films (each 4 cm^2) determined by IC = 66 μg

The composition corresponds to a molecular formula $Ag_{0.46}[AgCl]_{0.54}$

out, dipped in water to remove any reactant/product material sticking on it, and dried under vacuum for ~ 30 min; it was then ready for insertion into another reaction run.

3.4.1 *Kinetic Studies*

We have investigated the kinetics of degradation of MO using Ag/AgCl-PVA thin film having Ag/PVA weight ratio of 1.0 and Ag/AgCl mol ratio of ~ 1.0. The absorption spectrum was recorded at regular intervals during irradiation, to monitor the degradation of MO. Fig. 3.11a shows the profile of a typical reaction run; the peak decays steadily with irradiation time. The plot in Fig. 3.11b shows that the reaction catalyzed by the Ag/AgCl-PVA thin film follows first order kinetics with respect to the dye concentration with a rate constant of 0.045 min^{-1}. In a reaction with 40 nmol of MO using 7 μmol of catalyst, the extent of degradation was found to be ~ 93% in 1 h. The apparent quantum efficiency defined [41,42] using the initial rate of decomposition of the dye and the total incident power is 4.7 nM J^{-1} (Box 3.2). Unlike most of the earlier studies in this area which employed relatively high power (300 – 500 W) lamps with UV-Visible emission (requiring filters to remove UV light), we have experimented specifically with lower power, commercially available compact fluorescent lamps, showing emission exclusively in the visible range. Mol ratio of the catalyst to the dye (for one run of the reaction) extracted from the earlier reports where this information is available, ranges from ~ 50 – 900 (Table 3.2); the ratio in our case is 175 and therefore among the more efficient in the group. Similar conclusion can be drawn about the time taken for the reaction.

Box 3.2. Calculation of apparent quantum efficiency for MO degradation

Initial concentration of MO = 10 μM

Rate constant = 0.045 min^{-1} = 7.5×10^{-4} s^{-1}

Initial rate of degradation of MO by Ag/AgCl-PVA = 7.5 nM s^{-1}

Optical power incident at the reaction sample = 100 mW cm^{-2}

Total optical power on the catalyst (4×4 cm^2) = 1.6 W

Apparent quantum efficiency = (Initial rate/Total power) = **4.7 nM J^{-1}**

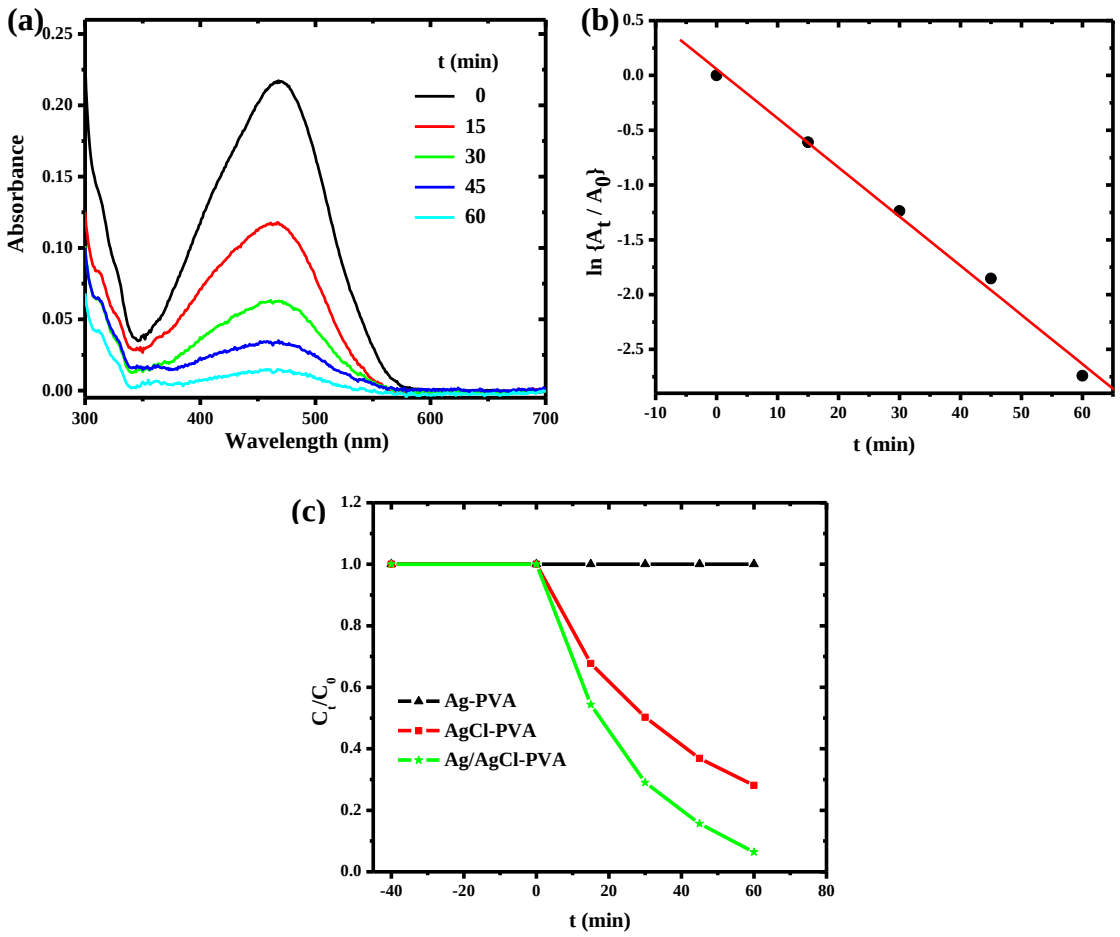

Figure 3.11. ***(a)*** *Optical absorption spectra of MO solution as a function of time (t) during the photocatalytic degradation, using Ag/AgCl-PVA.* ***(b)*** *Plot of the logarithm of the normalized absorbance (A) of the peak at 468 nm as a function of time (t); the least square fit to a straight line is also shown.* ***(c)*** *Decomposition of MO dye in presence of Ag-PVA, AgCl-PVA and Ag/AgCl-PVA thin films under visible-light irradiation; change of concentration (C) of the dye with time (0 corresponds to switching on the light) is shown.*

The control experiment with Ag-PVA showed no reaction (Fig. 3.11c). AgCl-PVA catalyzes the reaction at a lower rate than Ag/AgCl-PVA; AgCl is evidently a poorer photocatalyst, and Ag/AgCl that could enhance the rate forms only gradually under the photo-irradiation. Photo-degradation of dyes by Ag-AgCl through the

Table 3.2. *Comparison of the Ag/AgCl-PVA thin film with earlier reported Ag/AgCl catalysts used in the photo-decomposition of MO.*

Ref.	Lamp used for Irradiation		Time for one run (min)	Number of uses	Catalyst/MO mol ratio	
	Type	Power (W)			one run	total runs
9	Xe	300	30	8[a]	57	7
13	Xe	300	20	4	51	13
28	LED	?	150	9[d]	125	14
29	Xe	500	10	4	64	16
Ag/AgCl-PVA (this work)	CFL	170	60	10[b]	175	18
10	W	500	30	5[b]	116	23
5	Xe	300	15	10	229	23
17	Xe	500	8	10[a]	229	23
19	Xe	500	15	10[d]	230	23
16	Xe	500	24	5	159	32
8	Xe	300	6	6	230	38
6	W	300	40	5[a]	229	46
14	Xe	300	180	5[a]	229	46
18	Xe	500	1.5	4	229	57
20	Xe	500	160	4[c]	229	57
26	Xe	300	8	1	58	58
12	Xe	500	24	4[a]	230	58
25	Xe	55	120	5[b]	394	79
28	Xe	300	6	1	115	113
11	Xe	500	18	4	456	114
24	Xe	300	60	3[c]	574	191
15	Halogen	?	18	4[e]	916	229

Percentage of MO degradation at the end of multiple uses (first use: 90 - 100%) :
[a] 95% [b] 80% [c] 75 % [d] 50 % [e] large decrease

excitation of plasmons in Ag by visible light leading to formation of an electron, followed by ultrafast electron transfer to AgCl has been discussed in earlier reports.[8,12,17] The band gap of AgCl (Fig. 3.5) does not support efficient absorption of

Table 3.3. *Mass spectral data of the MO dye solution before and after photocatalytic reaction revealing the photo-degradation products.*

	m/z (main peaks)	**Structure (M)**
Reactant solution	303 [M-2]	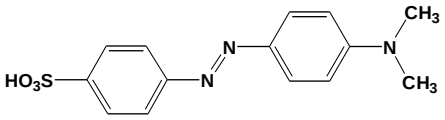
Product solution	202 [M]	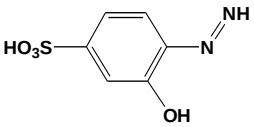
	173 (M-1) (& 348 [2M])	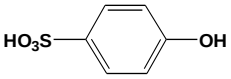
	156 [M-1] (& 334 [2M+Na-3])	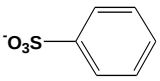
	97 [M-1]	H_2SO_4
	62 [M-1]	HNO_3

visible light; as suggested by the mechanism referred to above, the Ag nanoparticles in the Ag/AgCl- PVA film with their strong LSPR extinction, act effectively as dye-sensitizers and absorb visible light. Subsequent electron transfer to the conduction band of AgCl leads to the separation and stabilization of electron-hole pairs that finally carry out efficient dye degradation. Liquid chromatography-mass spectrometry (LC-MS)

analysis of the reaction product solution indicated typical fragments expected from the degradation of MO. The fragments and their corresponding *m/z* values along with the characterization of the reactant are summarized in Table 3.3.[43,44]

3.4.2 *Catalyst Recycling and Monitoring*

The unique advantage of the 'dip catalyst' is the ease with which it can be retrieved from a reaction system and reintroduced into another batch of the reaction after a simple wash; this is very much easier than the other methods of catalyst separation commonly employed, such as ultracentrifugation, filtration, magnetic separation etc. Equally important is the fact that the thin film nature of the 'dip catalyst' allows its convenient monitoring between successive reaction runs, by direct spectroscopy and microscopy. The extent of MO degradation achieved in 60 min in ten successive runs of the reaction using the same set of Ag/AgCl-PVA films is shown in Fig. 3.12. It is pertinent to note that the mol ratio of catalyst to dye over the ten runs works out to be ~ 18, which may be compared to the corresponding values in the earlier reports in the range 7 – 230 (Table 3.2). The photocatalytic application experiments thus demonstrate that the Ag/AgCl-PVA thin films show similar dye degradation

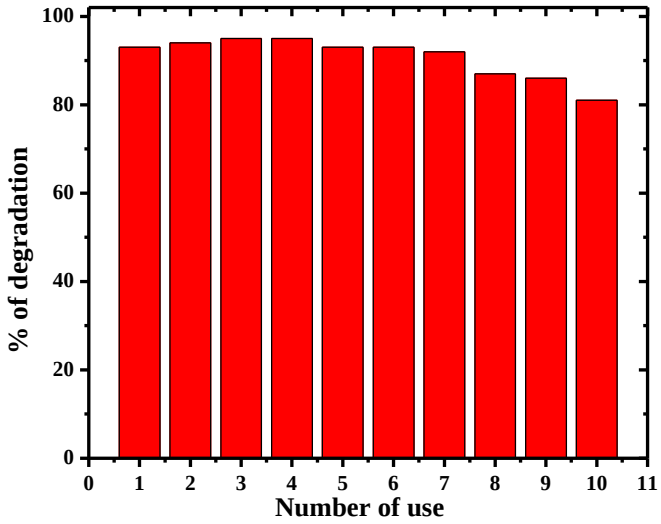

Figure 3.12. *Reuse of the Ag/AgCl-PVA thin film 'dip catalyst' in the degradation of MO; percentage of degradation at 60 min of reaction in each use is shown.*

capability and recyclability as some of the best formulations of the same catalyst developed earlier; as noted above, there are very few of those formulations that allowed recycling up to ten times as in the case of our 'dip catalyst'.

The high catalyst/dye ratio in the large number of earlier studies made it difficult to assess any changes or degradations that may be occurring in the Ag/AgCl system during its photocatalytic application. As mentioned earlier, AgCl does get reduced to Ag under photo-irradiation as well as e-beam irradiation;[37-39] in fact the former is commonly employed in the fabrication of the Ag/AgCl composite including our protocol (Fig. 3.3). The relatively small ratio of catalyst/dye used in our application and the thin film nature of the catalyst made its monitoring convenient through multiple runs. Extinction spectrum of the film recorded after successive pairs of runs (Fig. 3.13) shows a small but steady evolution (this may be contrasted with the strong decay in about 3 runs shown in Fig 3.2b); decrease in the UV absorption and a concomitant increase in the visible range with a clear isosbestic point at ~ 290 nm is suggestive of a gradual and directed shift in the Ag/AgCl composition. This observation as well as the elemental analysis indicates that there is no catalyst leaching during the reaction runs. It appears that even though the photo-generated charge carriers in the semiconductor-metal nanocomposite are effectively used in the degradation of MO, a fraction also contributes to the gradual reduction of part of the AgCl to Ag; this is indeed, an extension of the effect exploited for the initial fabrication of the nanocomposite thin film. It is relevant to note here that some of the earlier reports[5,6,11,19,45] of the fabrication of Ag/AgCl nanocomposite involved photo-irradiation of the AgCl in the presence of the same dye, decomposition of which is explored subsequently, using the fabricated Ag/AgCl. Broadening of the absorption in the visible range (Fig. 3.13) with increase in intensity in the 350 – 450 nm and > 600 nm ranges, is indicative of the formation of small Ag nanoparticles as well as the aggregation of the particles; many of the incipient nanoparticles with free surfaces are likely to add on to the existing particles leading to aggregate formation. These spectral observations are supported by the FESEM and TEM images Figs. 3.14 and 3.15. The electron diffraction pattern and high resolution TEM images (Fig. 3.15c-f) show the Ag and AgCl nanoparticles continue to coexist.

The gradual transition of part of the AgCl to Ag is clearly revealed in the elemental analysis which shows a parallel increase in the Ag:Cl ratio (Table 3.1). ICP-OES and IC analysis indicate that the Ag:AgCl ratio is ~ 2.5:1 after five uses of the Ag/AgCl-PVA thin film; the ratio increases to 3.6:1 and 4.7:1 after seven and ten uses

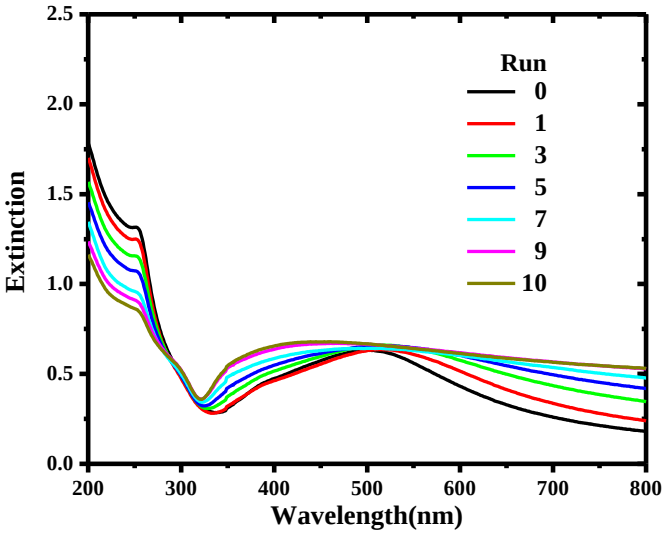

Figure 3.13. *Extinction spectra of the Ag/AgCl-PVA thin film through the reuse runs in the photocatalytic degradation of MO.*

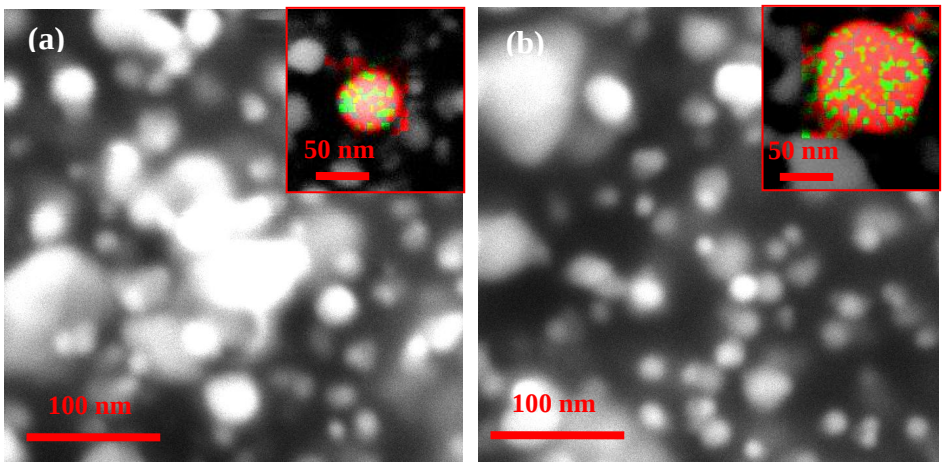

Figure 3.14. *FESEM images of Ag/AgCl-PVA thin film **(a)** after 1 use and **(b)** after 5 uses; scale bar = 100 nm. EDX spectra based mapping of Ag (red) and Cl (green) in single particles is shown in the insets.*

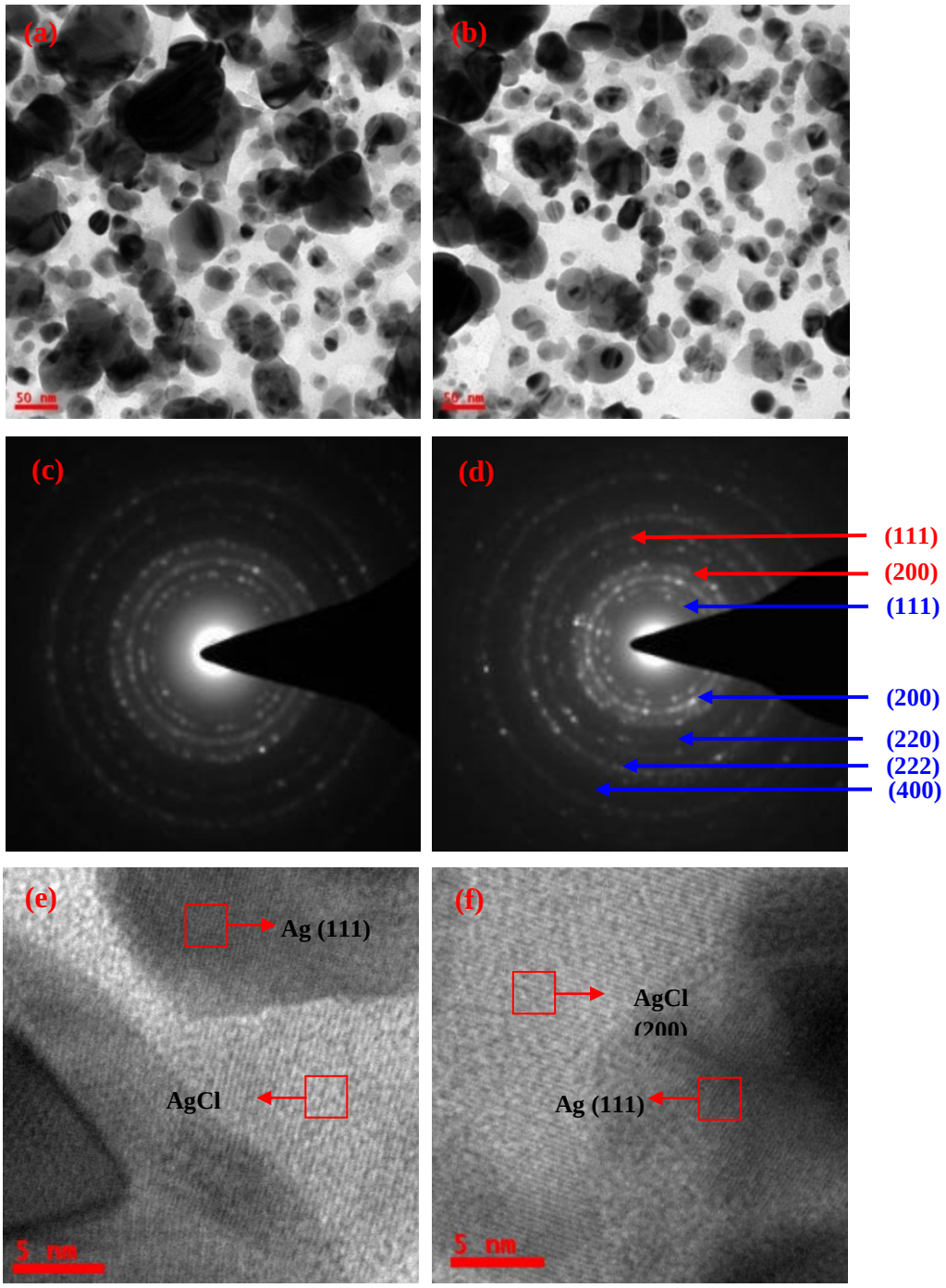

Figure 3.15. *TEM images (scale bar = 50 nm) of Ag/AgCl-PVA thin film **(a)** after 1 use and **(b)** after 5 uses; (c) and (d) the corresponding electron diffraction patterns (the diffraction spots are indexed to AgCl (blue) and Ag (red) nanoparticles); (e) and (f) the corresponding lattice images (scale bar = 5 nm) (relevant lattice planes observed in the high resolution images are indicated).*

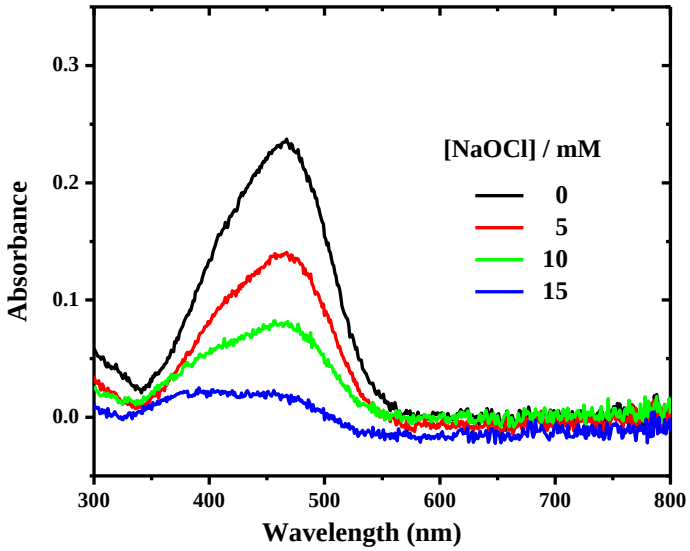

Figure 3.16. *Optical absorption spectra of MO (10 µM, 4 ml) solution treated with varying concentrations of NaOCl (recorded after 60 min of addition).*

respectively (Table 3.1). As the high catalytic efficiency of Ag/AgCl-PVA thin film shows signs of decline after the seventh use (Fig. 3.12), it is concluded that an Ag:AgCl ratio higher than ~3.5:1 is not desirable for the efficient photocatalytic degradation of MO.

It has been reported recently that the shift of AgCl to Ag due to photo-irradiation can be reversed by adding NaOCl into the reaction system;[31] consequent enhancement in the degradation of formic acid, but no reuse of the catalyst, was demonstrated in that study. We have checked the effect of NaOCl on catalyst stability as well as on MO degradation and observed that even though addition of NaOCl does retard the change in the Ag/AgCl-PVA film, it also oxidizes MO thus interfering in the degradation of the dye (Fig. 3.16); it is well known that peracids and NaOCl can oxidize MO and azo dyes in an aqueous medium.[46,47] Thus, addition of NaOCl does not help in demonstrating the utility of Ag/AgCl in the present instance.

Our study clearly shows that the gradual reduction of AgCl together with the aggregation of the Ag nanoparticles impair the photocatalytic activity after extended reuse of the Ag/AgCl catalyst; decrease in the effective surface area of individual

particles as well as the interface region between the metal and semiconductor particles are likely to contribute to this. Further optimization of the size and structure of the nanocomposite particles can provide improved stability and enhanced photocatalytic activity, allowing extended application of the Ag/AgCl-PVA thin film.

3.5 Summary

We have developed a facile *in situ* protocol for the fabrication of Ag/AgCl-PVA thin film with detailed characterization at each stage of the nanocomposite formation. The thin film was shown to serve as an efficient plasmonic photocatalyst for the degradation of MO dye, affording multiple, efficient reuses in the form of a 'dip catalyst'. The thin film form of the nanocomposite catalyst facilitated its concomitant monitoring by spectroscopy and microscopy, and the relative amount of catalyst and substrate employed in our studies allowed clear demonstration of how the Ag/AgCl system undergoes subtle changes over repeated uses which eventually can lead to the decline of catalytic activity. This study should prove useful in evaluating the current status of the metal-semiconductor nanocomposite based photocatalysts, and progressing towards even more efficient and sustainable designs.

References

1. Wang, P.; Huang, B.; Dai, Y.; Whangbo, M. *Phys. Chem. Chem. Phys.* **2012**, *14*, 9813–9825.
2. Liu, Z.; Hou, W.; Pavaskar, P.; Aykol, M.; Cronin, S. B. *Nano Lett.* **2011**, *11*, 1111– 1116.
3. Liu, Y. P.; Fang, L.; Lu, H. D.; Liu, L. J.; Wang, H.; Hu, C. Z. *Catal. Commun.* **2012**, *17*, 200–204.
4. Kuai, L.; Geng, B.; Chen, X.; Zhao,Y.; Luo, Y. *Langmuir* **2010**, *26*, 18723–18727.
5. Wang, P.; Huang, B.; Qin, X.; Zhang, X.; Dai, Y.; Wei, J.; Whangbo, M. *Angew. Chem. Int. Ed.* **2008**, *47*, 7931–7933.
6. Wang, P.; Huang, B.; Lou, Z.; Zhang, X.; Qin, X.; Dai, Y.; Zheng, Z.; Wang, X. *Chem. Eur. J.* **2010**, *16*, 538–544.
7. Dong, L.; Liang, D.; Gong, R. *Eur. J. Inorg. Chem.* **2012**, 3200–3208.
8. Tang, Y.; Jiang, Z.; Xing, G.; Li, A.; Kanhere, P. D.; Zhang, Y.; Sum, T. C.; Li, S.; Chen, X.; Dong, Z.; Chen, Z. *Adv. Funct. Mater.* **2013**, *23*, 2932–2940.
9. Han, C.; Ge, L.; Chen, C.; Li, Y.; Zhao, Z.; Xiao, X.; Li, Z.; Zhang, J. *J. Mater. Chem. A* **2014**, *2*, 12594–12600.
10. Wu, S.; Shen, X.; Ji, Z.; Zhu, G.; Chen, C.; Chen, K.; Bu, R.; Yang, L. *CrystEngComm.* **2015**, *17*, 2517–2522.
11. Han, L.; Wang, P.; Zhu, C.; Zhai, Y.; Dong, S. *Nanoscale* **2011**, *3*, 2931–2935.
12. Lin, Z. Y.; Xiao, J.; Yan, J. H.; Liu, P.; Li, L. H.; Yang, G. W. *J. Mater. Chem. A* **2015**, *3*, 7649–7658.
13. Song, J.; Roh, J.; Lee, I.; Jang, J. *Dalton Trans.* **2013**, *42*, 13897–13904.
14. Xu, H.; Li, H.; Xia, J.; Yin, S.; Luo, Z.; Liu, L.; Xu, L. *ACS Appl. Mater. Interfaces* **2011**, *3*, 22–29.
15. Kulkarni, A. A.; Bhanage, B. M. *ACS Susatain. Chem. Eng.* **2014**, *2*, 1007–1013.

16. Zhu, M.; Chen, P.; Ma, W.; Lei, B.; Liu, M. *ACS Appl. Mater. Interfaces* **2012**, *4*, 6386–6392.

17. Cai, B.; Wang, J.; Gan, S.; Han, D.; Wu, Z.; Niu, L. *J. Mater. Chem. A* **2014**, *2*, 5280–5286.

18. Xu, Z.; Han, L.; Hu, P.; Dong, S. *Catal. Sci. Technol.* **2014**, *4*, 3615–3619.

19. Han, L.; Xu, Z.; Wang, P.; Dong, S. *Chem. Commun.* **2013**, *49*, 4953−4955.

20. Zhou, Z.; Peng, X.; Zhong, L.; Wu, L.; Cao, X.; Sun, R. C. *Carbohydr. Polym.* **2016**, *136*, 322–328.

21. Zhang, S.; Li, J.; Wang, X.; Huang, Y.; Zheng, M.; Xu, J. *ACS Appl. Mater. Interfaces* **2014**, *6*, 22116−22125.

22. Zhang, H.; Fan, X.; Quan, X.; Chen, S.; Yu, H. *Environ. Sci. Technol.* **2011**, *45*, 5731–5736.

23. Zhu, M.; Chen, P.; Liu, M. *Langmuir* **2013**, *29*, 9259−9268.

24. Li, Y.; Ding, Y. *J. Phys. Chem. C* **2010**, *114*, 3175–3179.

25. Chen, X. Y.; Hou, J. J.; Yang, H.; Xu, Z. L.; *J. Environ. Chem. Eng.* **2016**, *4*, 1068–1075.

26. Bi, Y.; Ye, J. *Chem. Commun.* **2009**, 6551–6553.

27. Zhu, M.; Chen, P.; Liu, M. *J. Mater. Chem.* **2012**, *22*, 21487–21494.

28. Ge, J.; Wang, X.; Yao, H. B.; Zhu, H.W.; Peng, Y. C.; Yu, S. H. *Mater. Horiz.* **2015**, *2*, 509–513.

29. Sun, L.; Zhang, R.; Wang, Y.; Chen, W. *ACS Appl. Mater. Interfaces* **2014**, *6*, 14819–14826.

30. Luckey, G. W. *J. Chem. Phys.* **1955**, *23*, 882–890.

31. Garg, S.; Rong, H.; Miller, C. J.; Waite, T. D. *J. Phys. Chem. C* **2016**, *120*, 5988–5996.

32. Wu, Y. A.; Li, L.; Li, Z.; Kinaci, A.; Chan, M. K. Y.; Sun, Y.; Guest, J. R.; McNulty, I.; Rajh, T.; Liu, Y. *ACS Nano* **2016,** *10*, 3738–3746.

33. Porel, S.; Singh, S.; Harsha, S. S.; Rao, D. N.; Radhakrishnan, T. P. *Chem. Mater.* **2005,** *17*, 9–12.

34. Husein, M.; Rodil, E.; Vera, J. *Langmuir* **2003**, *19*, 8467–8474.

35. Cheng, D.; Xia, H.; Chan, H. S. O. *Langmuir* **2004**, *20*, 9909–9912.

36. Wang, G.; Mitomo, H.; Matsuo, Y.; Shimamoto, N.; Niikura, K.; Ijiro, K. *J. Mater. Chem. B* **2013**, *1*, 5899–5907.

37. Glaus, S.; Calzaferri, G. *Photochem. Photobiol. Sci.* **2003**, *2*, 398–401.

38. Ueta, M.; Kanzaki, H.; Kobayashi, K.; Toyozawa, Y.; Hanamura, E. Excitonic Processes in Solids, in Springer Series in Solid State Sciences, Ed. Fulde, P. Springer-Verlag, Berlin, **1986**, p.310–530.

39. Liang, Y.; Lin, S.; Liu, L.; Hu, J.; Cui, W. *Mater. Res. Bull.* **2014**, *60*, 382-390.

40. II-VI and I-VII Compounds; Semimagnetic Compounds, Eds. Madelung, O.; Rössler, U.; Schulz, M. Springer, Berlin Heidelberg, **1999**, p. 1-7.

41. Buriak, J. M; Kamat, P. V.; Schanze, K. S. *ACS Appl. Mater. Interfaces* **2014**, *6*, 11815-11816.

42. Hoffmann, M. R.; Martin, S. T.; Choi, W.; Bahnemannt, D. W. *Chem. Rev.* **1995**, *95*, 69-96.

43. Baiocchi, C.; Brussino, M. C.; Pramauro, E.; Prevot, A. B.; Palamisano, L.; Marcì, G. *Int. J. Mass Spectrom.* **2002**, *214*, 247-256.

44. Patra, A. K.; Kundu, S. K.; Bhaumik, A.; Kim, D. *Nanoscale* **2016**, *8*, 365-377.

45. Zhu, Y.; Liu, H.; Yang, L.; Liu, J. *Mater. Res. Bull.* **2012**, *47*, 3452-2458.

46. Oakes, J.; Gratton, P. J. *J. Chem. Soc. Perkin Trans.* **1998**, *2*, 2563–2568.

47. Kanazawa, H.; Harata, Y. *Sci. Rep. Fukushima Univ.* **1993**, *51*, 31-35.

CHAPTER 4

Tuning the SERS Response with Silver-Gold Nanoparticle-Embedded Polymer Thin Film Substrates

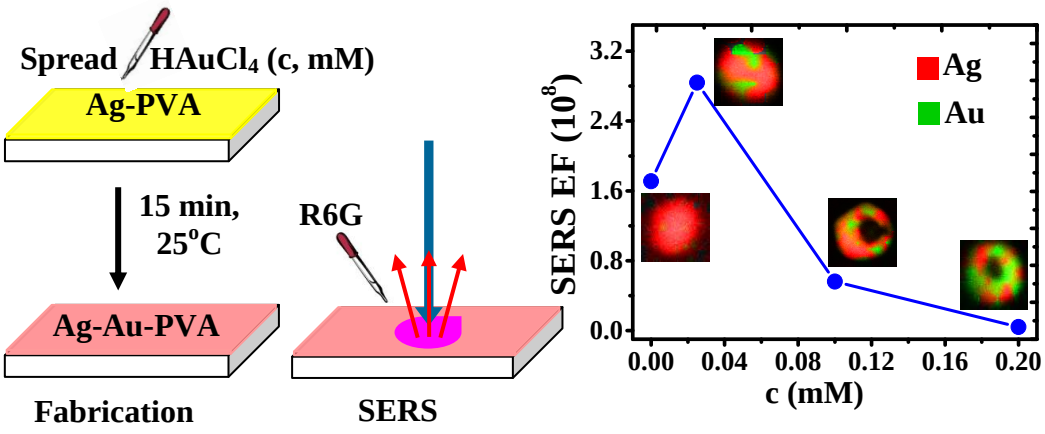

Ag-Au nanoparticle- embedded polymer thin films are fabricated and the composition dependence of SERS efficiency is explored.

Paper published

Rao, V. K.; Radhakrishnan, T. P. *ACS Appl. Mater. Interfaces* **2015**, *7*, 12767-12773.

Scope

In this chapter we extend the methodology developed in chapter 2, to the fabrication of bimetallic silver-gold (Ag-Au) nanoparticles embedded in a polymer thin film, and investigate their utilisation as surface enhanced Raman scattering (SERS) substrate; the topic of special interest is the dependence of SERS enhancement on the Ag-Au composition. Development of facile routes to the fabrication of thin film substrates with tunable SERS efficiency, and identification of the optimal conditions for maximizing the enhancement factor (EF) are significant in terms of both fundamental and application aspects of SERS. We fabricated polymer thin films with embedded bimetallic nanoparticles of Ag-Au by the simple 2-stage protocol described in chapter 2. Ag nanoparticles were formed in the first stage, by the in situ reduction of silver nitrate by the poly(vinyl alcohol) (PVA) film through mild thermal annealing, without any additional reducing agent. In the second stage, aqueous solutions of chloroauric acid spread on the Ag-PVA thin film under ambient conditions, lead to the galvanic displacement of Ag by Au in situ inside the film, and the formation of Ag-Au particles. Evolution of the morphology of the bimetallic nanoparticles into hollow cage structures, and the distribution of Au on the nanoparticles were revealed through electron microscopy and energy dispersive X-ray spectroscopy. The localized surface plasmon resonance (LSPR) extinction of the nanocomposite thin film evolves with the Ag-Au composition; theoretical simulation of the extinction spectra provided insight into the observed trends. The Ag-Au-PVA thin films were shown to be efficient substrates for SERS. The EF follows the variation of the LSPR extinction vis-à-vis the excitation laser wavelength, but with an offset, and the maximum SERS effect was obtained at very low Au content; experiments with Rhodamine 6G showed EFs of the order of 10^8 and a limit of detection of 0.6 pmol. The study presented in this chapter describes a facile and simple fabrication of a nanocomposite thin film that can be conveniently deployed in SERS investigations, and the utility of the bimetallic system to tune and maximize the EF.

4.1 Introduction

Surface enhanced Raman scattering (SERS) is a phenomenon of great interest and impact from both fundamental science and analytical application perspectives.[1,2] Many of the basic as well as application requirements for realizing efficient SERS response highlighted in Sec. 1.6.3 can be met using *in situ* fabricated metal-polymer nanocomposite thin films.[3,4] The method developed in our laboratory which allows the generation of a homogeneous distribution of nanoparticles of noble metals such as silver,[5] gold[6] and palladium,[7] and also uncommon materials like nanodrops of mercury,[8] within a thin polymer film, through the *in situ* reduction of the metal ions by the polymer has been described in Sec. 1.5.1. The protocol was extended to generate bimetallic nanoparticles of Ag-Pd as described in chapter 2.[9]

Here we described a protocol similar to that used for Ag-Pd nanoparticles, now optimized for the fabrication of Ag-Au nanoparticles with systematically varied composition, *in situ* inside poly(vinyl alcohol) (PVA) thin film. Ag-PVA thin film containing a uniform distribution of Ag nanoparticles was fabricated in the first stage by the reduction of $AgNO_3$ inside solid PVA film catalysed by a small amount of $Cu(NO_3)_2$. Spreading the required amount of $HAuCl_4$ solution on the Ag-PVA film under ambient conditions followed by simple washing, led to the formation of Ag-Au-PVA thin film. The LSPR peak could be tuned from ~ 430 to ~ 760 nm by increasing the concentration of the $HAuCl_4$ solution up to ~ 0.15 mM; the trends could be analysed through spectral simulations. Evolution of the composition and morphology of the alloy nanoparticles is explored using ICP analysis, TEM, FE-SEM and EDX spectroscopy and mapping. SERS experiments were conducted using Rhodamine 6G (R6G) as the probe molecule on the substrates having varying Ag-Au composition and exhibiting a smoothly evolving LSPR peak. With 488 nm excitation laser, the EF was found to increase briefly with increasing Au content but then fall off at higher values. We discussed the relation with the LSPR peaks of the substrates.

4.2 Ag-Au-PVA Thin Film

4.2.1 *Fabrication of Ag-Au-PVA Thin Film*

We have fabricated Ag-Au-PVA thin film using the two-stage fabrication (Fig. 4.1) methodology similar to that developed for the *in situ* generation of Ag-Pd nanoparticles embedded in PVA film in chapter 2. In the first stage, Ag-PVA thin film with Ag/PVA weight ratio (x) =0.8 and 1.4 wt % of Cu^{2+} was fabricated on the glass/ quartz/ Si wafer substrates as discussed in Sec. 2.2, relatively large (30 - 40 nm) Ag nanoparticles were formed in the thin film.[9] In the second stage, bimetallic nanoparticles of Ag-Au were prepared by the galvanic displacement of Ag by Au atoms using the following procedure. Aqueous solutions of ~ 0.5 mL of $HAuCl_4$ with concentrations ranging from 0.005 – 0.200 mM was spread uniformly on the Ag-PVA film and kept for 15 min under ambient temperature (~ 25°C) conditions, inside a closed petri dish to avoid evaporation. The film was then washed with ~ 1 mL of water to remove the unreacted $HAuCl_4$ solution present on the film as well as byproducts such as Ag^+ and HCl, and dried under vacuum.

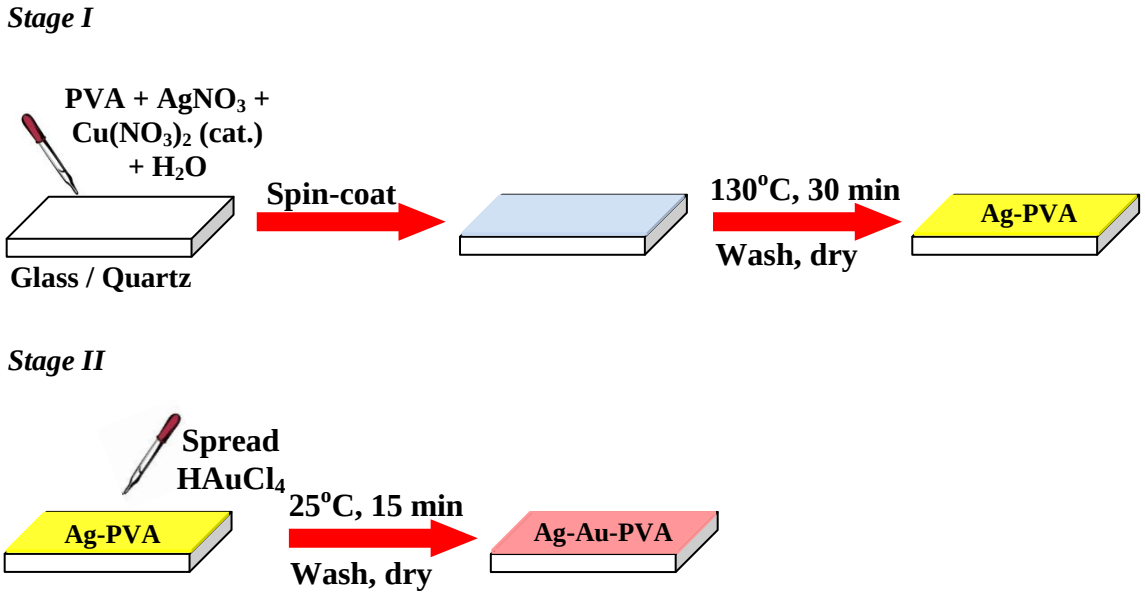

Figure 4.1. *Schematic showing the in situ synthesis of Ag-PVA followed by Ag-Au-PVA thin film.*

4.2.2 *Spectroscopy, Microscopy and Chemical Analysis of Ag-Au-PVA Thin Film*

Thickness of the final films was measured using a surface profilometer, and it was found to be ~ 200 nm. The Ag-Au composition of the Ag-Au-PVA thin films, were estimated by ICP-OES analysis and EDX spectroscopy together with imaging in TEM as well as FESEM (Table 4.1). The expected trend of increasing Au content with increasing concentrations of $HAuCl_4$ is found to be similar in all the cases; the difference in observed values is discussed later. The values from ICP-OES analysis represent to bulk composition; the maximum Au content is found to be ~ 5.4 atom% in the film fabricated with c = 0.2 mM.

We have examined the systematic evolution of the LSPR extinction of the metal-polymer nanocomposite thin films as the nanoparticles change from pure Ag to Ag-Au with increasing Au content (Fig. 4.2). The peak at 434 nm observed with the original Ag-PVA shifts gradually up to 761 nm in the case of Ag-Au-PVA prepared using a 0.15 mM solution of $HAuCl_4$ (Table 4.2). There is a concomitant and steady decrease in the intensity of the extinction peak; this is mainly a consequence of the relatively lower extinction coefficient of Au compared to Ag.

Table 4.1. *Atom % of Au with respect to the total metal (Au+Ag) content in the Ag-Au-PVA thin films fabricated by spreading different concentrations (c, mM) of $HAuCl_4$ on Ag-PVA(x=0.8) thin films, estimated using ICP-OES, EDX (TEM) and EDX (FESEM) analysis.*

c (mM)	Atom% of Au		
	ICP-OES	EDX (TEM)	EDX (FESEM)
0.025	1.62	2.77	1.25
0.050	2.43	4.73	5.65
0.100	3.00	11.51	10.25
0.200	5.37	24.01	16.25

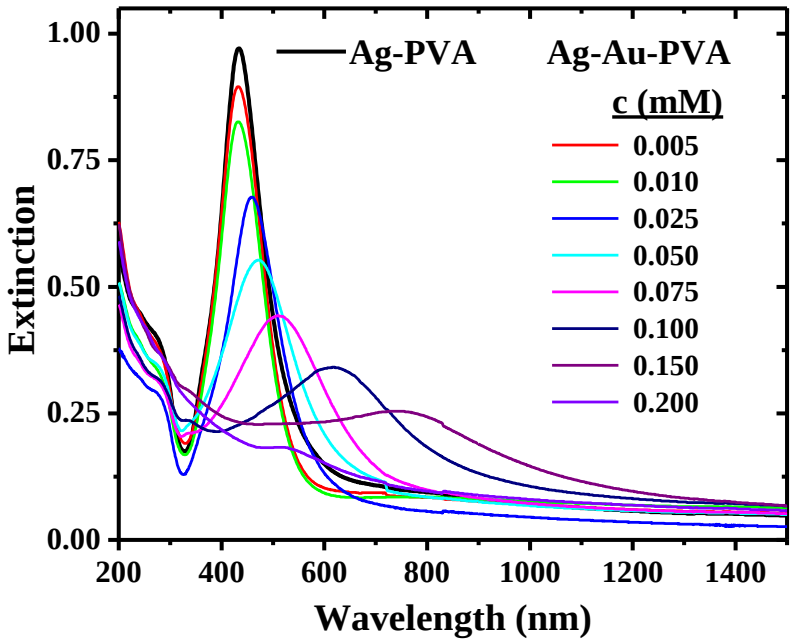

Figure 4.2. *Optical extinction spectra of Ag-PVA and Ag-Au-PVA thin films formed by treating Ag-PVA with different concentrations (c, mM) of $HAuCl_4$ solution.*

In order to gain insight into the evolution of the spectral profiles and peak shifts, we have carried out computational simulation of the LSPR extinction spectra of spherical hollow Ag-Au nanoparticles with different sizes and compositions using the DDSCAT software (Version 7.3), that employs the discrete dipole approximation.[10,11] The 'CONELLIPS' option was used to specify the target geometry of hollow spheres; the inner and outer radii were chosen based on the average values observed in the relevant TEM images shown later. The inner sphere was chosen to be vacuum and the shell, Ag_pAu_q alloy, where p and q are the mol fractions of Ag and Au (values determined from the EDX analysis in TEM were used in the computation, however, those based on the other analyses lead to similar spectral profiles and variations). Optical constants, n and k of Ag_pAu_q alloy at wavelength λ were estimated as the weighted average of the values of pure Ag and Au:

$$n_{Ag_pAu_q}(\lambda) = p * n_{Ag}(\lambda) + q * n_{Au}(\lambda),$$

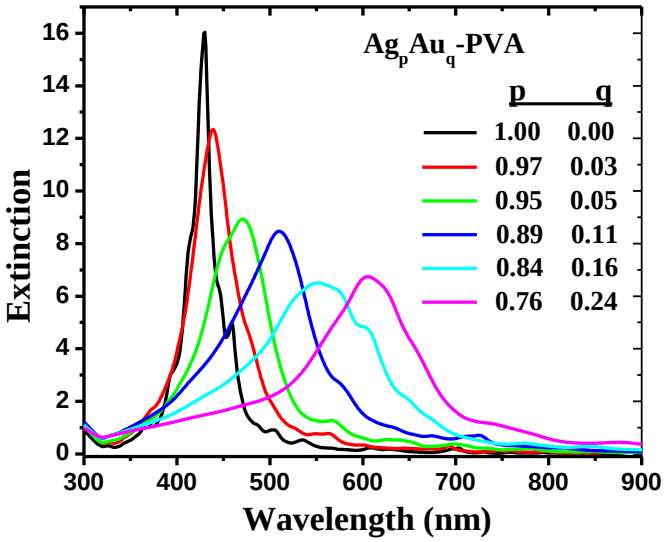

Figure 4.3. *LSPR extinction spectra simulated for spherical hollow Ag_pAu_q nanoparticles with different inner and outer radii (see Table 4.2) in PVA matrix.*

Table 4.2. *λ_{max} of the LSPR spectra simulated for spherical hollow Ag_xAu_y nanoparticles with different compositions and outer (alloy) / inner (vacuum) radii, in PVA matrix; the compositions and radii are chosen based on the EDX and TEM measurements on the Ag-Au nanoparticles in PVA fabricated using different concentrations (c, mM) of $HAuCl_4$. λ_{max} of the experimental LSPR spectra of the respective Ag-Au-PVA thin films are also shown.*

c (mM)	Ag_pAu_q		Outer radius (nm)	Inner radius (nm)	λ_{max} (nm) (simulation) (Fig. 4.3)	λ_{max} (nm) (experiment)
	p	q				
0.000	1.00	0.00	15	0	430	434
0.025	0.97	0.03	20	0	439	459
0.050	0.95	0.05	20	10	470	473
0.100	0.89	0.11	25	15	510	628
0.150	0.84	0.16	25	18	552	761
0.200	0.76	0.24	25	20	605	522

and similarly, k.[12] PVA (refractive index = 1.55) was used as the ambient medium. Formation of hollow structures with decreasing shell thickness causes significant red shift and broadening of the LSPR peak (Fig. 4.3). The red shift observed in the films with relatively low fractions of Au (fabricated with c ≤ 0.05mM) is in good agreement with the computed values; however at larger fractions of Au, the computed values are significantly lower than that observed experimentally (Table 4.2). In order to understand the latter discrepancy, we have carried out simulations for spherical hollow Au nanoparticles following similar procedure as above. The inner sphere was chosen to be vacuum (air) and the shell to be pure Au. The outer radius was fixed at 25 nm, and different inner radii were considered. The simulated spectra are shown in Fig. 4.4; the data in Table 4.3 suggest strong red shift of the peak as Au shells with decreasing thickness are formed. These computations on hollow Au spheres suggest that the red shifts of observed peaks with respect to the simulated are for c = 0.1 – 0.15 mM in table 4.2 may be due to the formation of thin Au shells through partial separation of Au. On further increase of Au (c = 0.20 mM), the LSPR peak blue shifts to ~ 522 nm (Fig 4.2), indicative of extinction due to solid Au nanostructures with no noticeable intensity due to Au-Ag; this could be due to the formation of Au patches over the Ag-Au

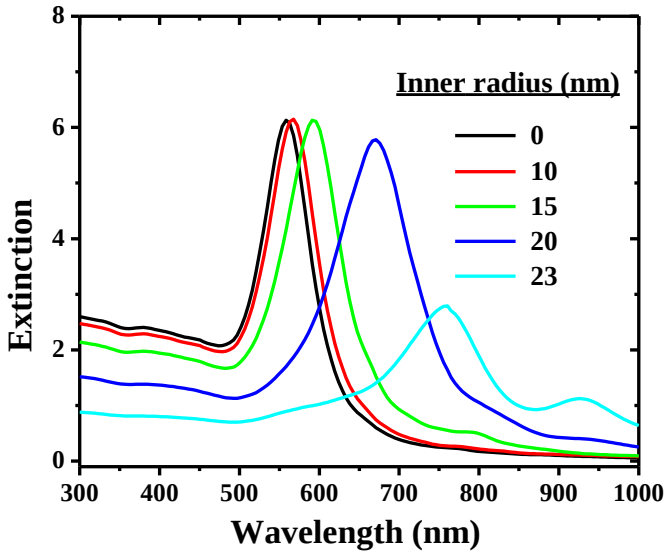

Figure 4.4. *LSPR extinction spectra simulated for spherical hollow Au nanoparticles with outer radius of 25 nm and different inner radii, in PVA matrix.*

Table 4.3. *λ_{max} of the LSPR spectra simulated for spherical hollow Au nanoparticles with outer radius of 25 nm and different inner radii, in PVA matrix.*

Inner radius (nm)	**λ_{max} (nm) (simulation) (Fig. 4.4)**
0	558
10	568
15	591
20	671
23	760, 925

nanoparticle. It is pertinent to note that several earlier studies have reported similar observations of blue shift in the LSPR peak of Ag-Au nanoparticles upon enhancing the Au content significantly, and attributed it to the fragmentation of the nanostructures.[13-16] Tuning of the LSPR peak forms the basis for the SERS studies discussed later.

Evolution of the morphology of the nanoparticles with increasing Au content is revealed by the TEM images in Fig. 4.5; selected area electron diffraction shows that these particles are crystalline. Formation of the hollow cage structures at higher Au content is seen in the more magnified images. The presence of Ag and Au in Ag-Au nanoparticles cannot be confirmed by electron diffraction and lattice images because of the similar lattice spacing values of the two metals. It is confirmed by EDX mapping of the nanoparticles discussed below. The hollow structures appear to result from the Kirkendall effect[17] arising due to the different rates of diffusion of the two kinds of atoms/ions involved; similar observations have been made earlier with Ag-Pd[9] as well as Ag-Au[13] nanoparticles. The increasing surface roughness could support applications such as catalysis or SERS. The FE-SEM images of the Ag-Au nanoparticles embedded in the PVA thin film (Fig. 4.6) reveal morphological changes similar to that observed in the TEM images. The area mapping of single particles shows graphically, the

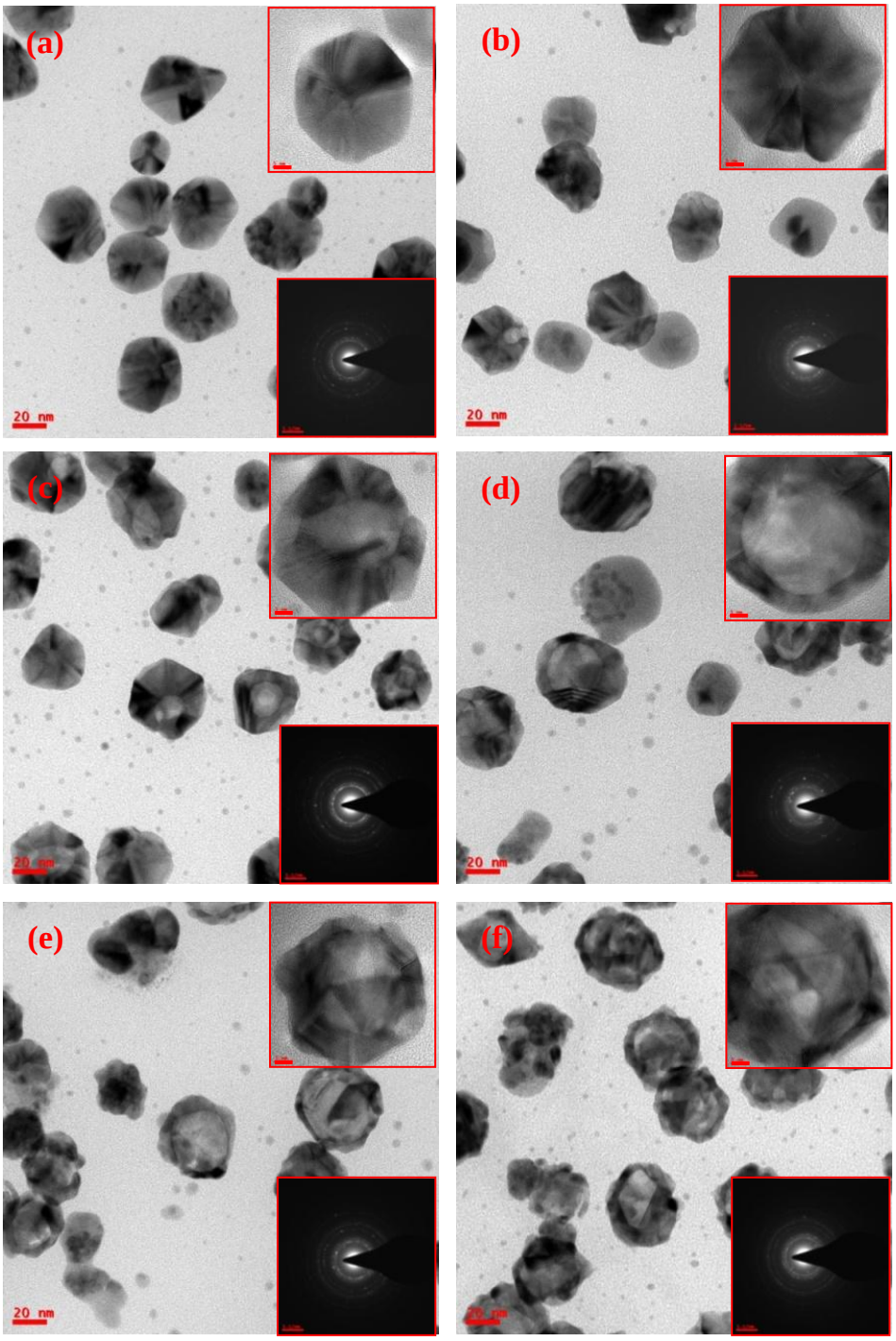

Figure 4.5. *TEM images of **(a)** Ag-PVA and Ag-Au-PVA thin films formed by treating Ag-PVA with different concentrations (c, mM) of $HAuCl_4$ solution: **(b)** 0.025, **(c)** 0.05, **(d)** 0.10, **(e)** 0.15 and **(f)** 0.20. Scale bar = 20 nm; magnified images (scale bar = 5 nm) of single particle and electron diffraction pattern are shown in the inset.*

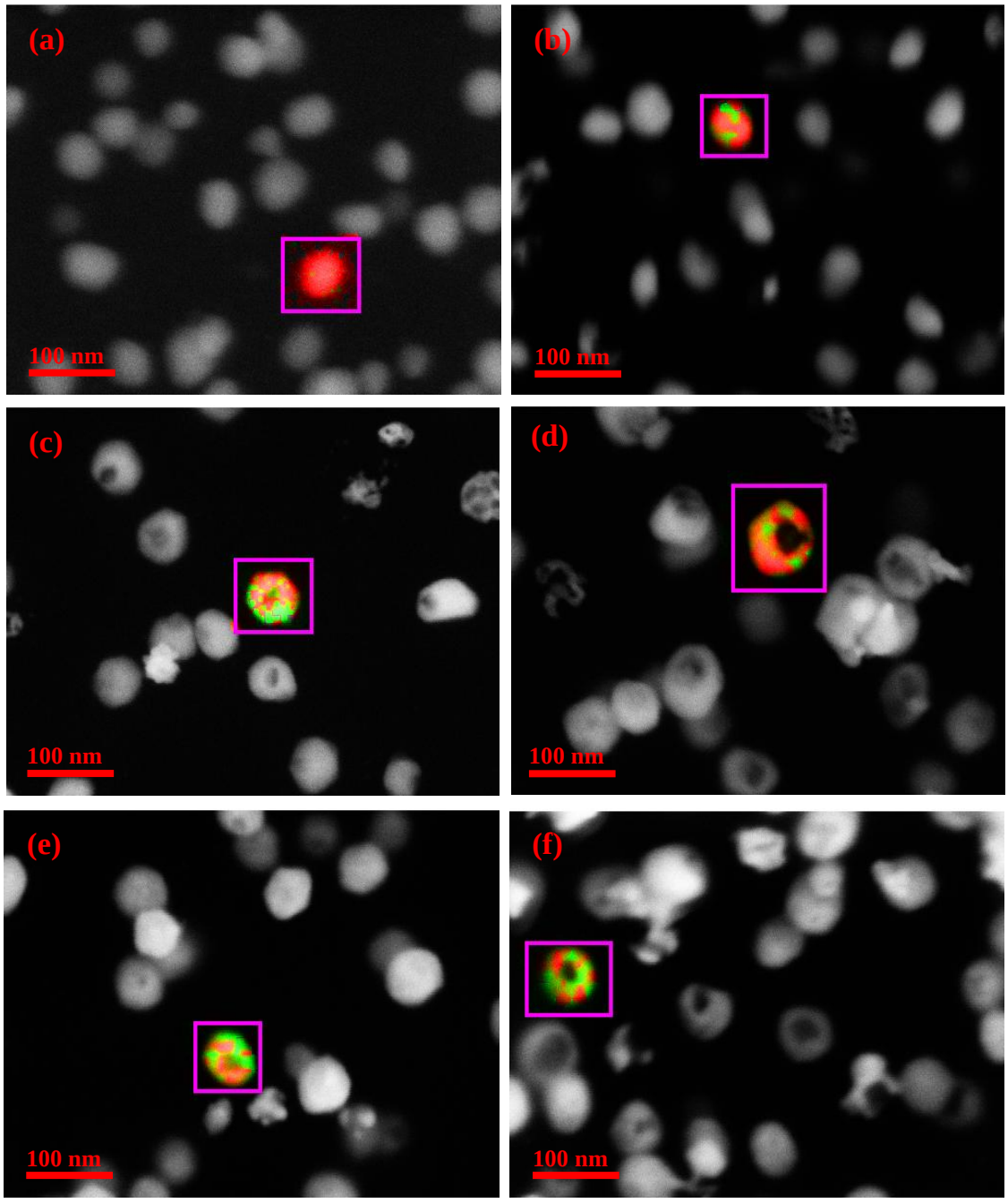

Figure 4.6. *FE-SEM images combined with EDX area mapping, of* ***(a)*** *Ag-PVA and Ag-Au-PVA thin films formed by treating Ag-PVA with different concentrations (c, mM) of* $HAuCl_4$ *solution:* ***(b)*** *0.025,* ***(c)*** *0.05,* ***(d)*** *0.10,* ***(e)*** *0.15 and* ***(f)*** *0.20; scale bar = 100 nm. The EDX mapping shows Ag (red) Au (green) regions in a selected particle.*

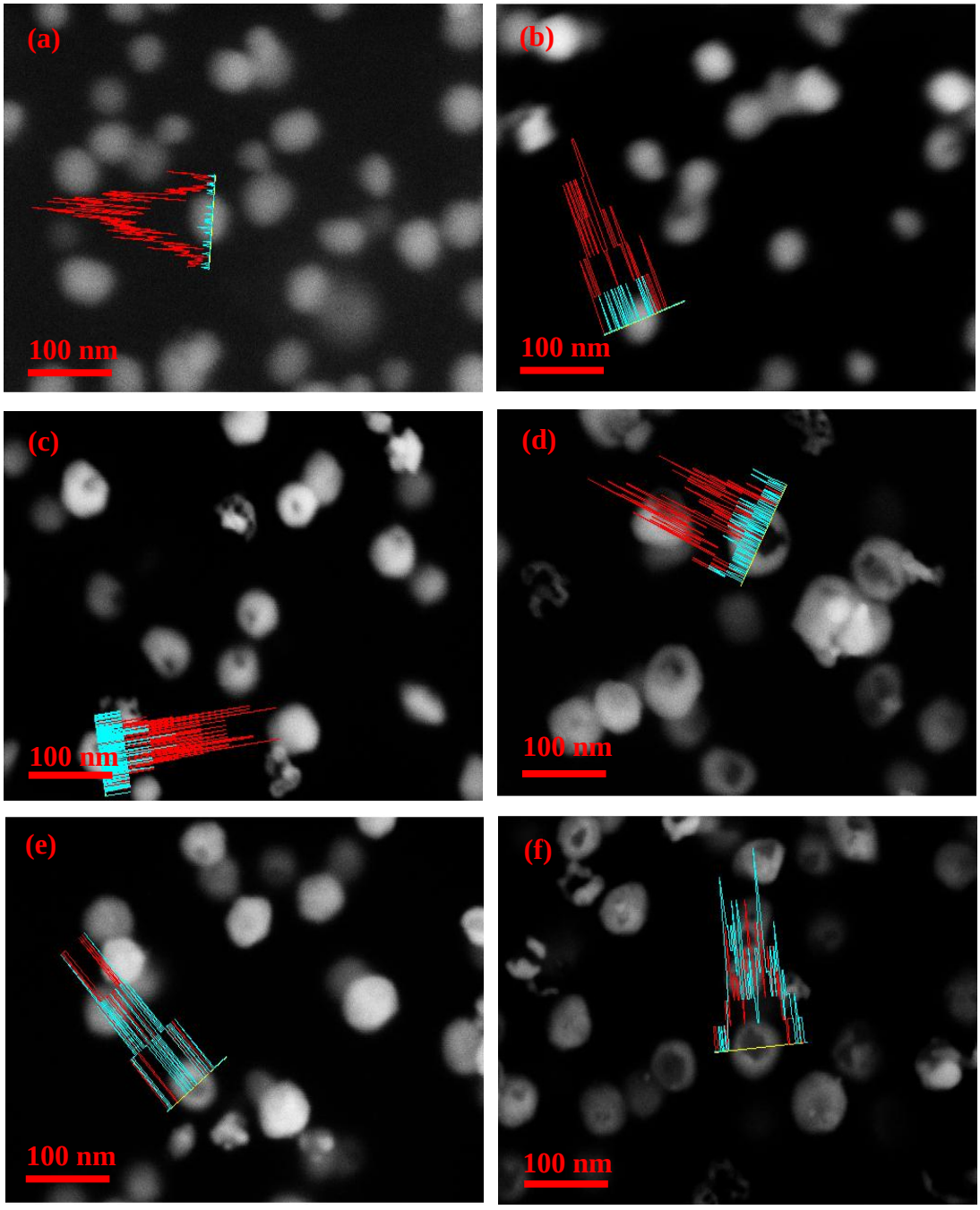

Figure 4.7. *FE-SEM images combined with EDX line mapping (red - Ag; cyan - Au) of* ***(a)*** *Ag-PVA and Ag-Au-PVA thin films formed by treating Ag-PVA with different concentrations (c, mM) of* $HAuCl_4$ *solution:* ***(b)*** *0.025,* ***(c)*** *0.05,* ***(d)*** *0.10,* ***(e)*** *0.15 and* ***(f)*** *0.20. Scale bar = 100 nm.*

increasing Au content and the distribution of Au on the Ag nanoparticles (Fig. 4.6). The EDX line profile is consistent with the hollow structure of the particles and provides insight into the elemental distribution (Fig 4.7). Quantitative estimates of the Au content across the series follow the same trend as observed from the ICP analysis, but show relatively higher values (Table 4.1); such differences are well-known[18] and attributable to the fact that the EDX probes primarily the surface composition whereas the ICP analyzes the total content.

4.3 SERS Studies

The protocol we have optimized for the preparation of samples on the SERS substrate is particularly convenient, as the analyte solution is simply spread on the nanocomposite thin film and allowed to get absorbed in the polymer film, and get adsorbed on the bimetal nanoparticles; this may be contrasted with methods such as incubation required in some of the earlier studies.[19,20] We have conducted the SERS experiments using different substrates including Ag-PVA as well as Ag-Au-PVA (with different Au content) coated on silicon wafer. Rhodamine 6G (R6G) was used as the analyte molecule; 20 µL of a 4.5 µM solution of R6G in methanol was spread uniformly on the substrate and dried under ambient atmosphere. A WITec model Alpha 300 R Raman microscope (with AFM) was used for recording the Raman spectra, with 0.5 s integration time and 10 accumulations, through a 20× aperture (NA = 0.4). A 488 nm laser was used as the excitation source. The laser intensity was maintained constant in all measurements, 100 µm detecting fiber was used to collect the spectra. Raman spectrum for the bulk material used as the reference, was recorded using a small R6G microcrystal placed on the Si wafer.

The spectra of R6G recorded using the Ag-Au-PVA thin films with low Au content were found to increase slightly in intensity with time and reach steady values after ~ 24 h; the relative SERS intensities across the substrates with different compositions remain the same, however. As the LSPR spectra of these Ag-Au-PVA films are reproducible over several days, we believe that the spectral changes occur due to the progress of the analyte adsorption on the nanoparticles reaching equilibrium over

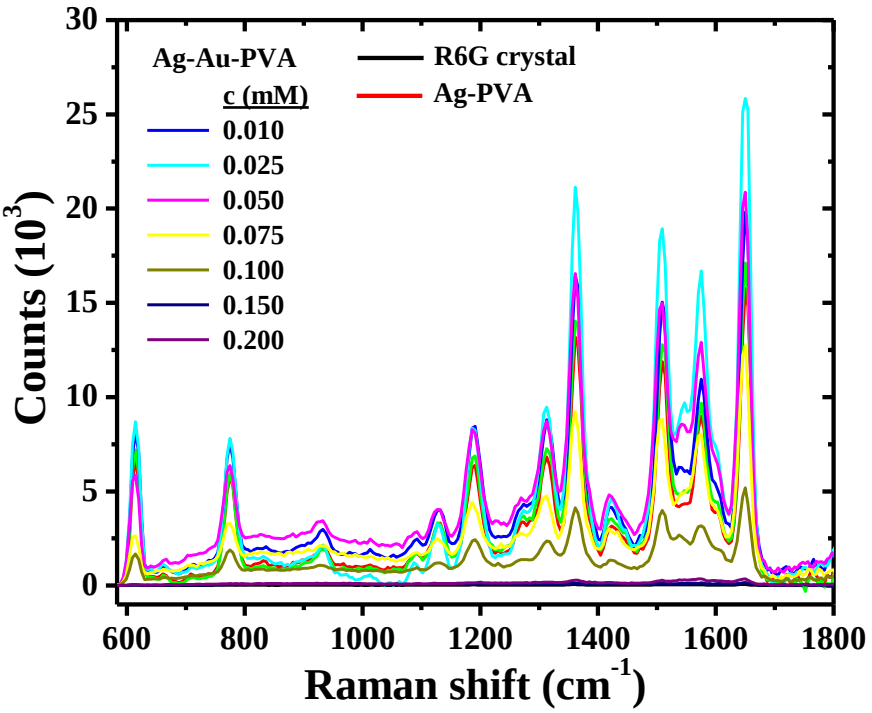

Figure 4.8. *Raman spectra of R6G microcrystals and solution adsorbed on Ag-PVA thin film and Ag-Au-PVA thin films formed by treating Ag-PVA with different concentrations (c, mM) of $HAuCl_4$ solution.*

several hours. The Raman spectra of R6G recorded on different substrates after 24 h are displayed in Fig. 4.8. Peaks in the spectrum of the reference R6G sample spectrum are hardly visible, but can be discerned on magnification, allowing the quantitative estimation of the EF. A relatively low spectral profile is obtained with Ag- PVA as the substrate. With increasing Au content, intensities of all the peaks increase, reach a maximum and thereafter decrease steadily.

4.3.1 *Calculation of SERS Enhancement Factor*

The number of molecules in the reference sample (N_{Bulk}) was determined using the focal volume of the laser spot incident on the microcrystal and the density of the material. The number of molecules in the sample (N_{SERS}) was estimated by considering the total number of molecules spread on the substrate, assuming a homogeneous distribution across the thin film and the fraction falling within the laser spot area.

Box 4.1 : Derivation of N_{Bulk} / N_{SERS}

Laser spot diameter, $W_o = \frac{1.22\lambda}{NA}$ Focal depth: $Z_o = \left(\frac{2\pi}{\lambda}\right) W_o^2$

Focal volume: $\tau = \left(\frac{\pi}{2}\right)^{1.5} W_o^2 Z_o$

N_{Bulk} = ((Focal volume * Density)/ (Molecular weight))*N_A

N_{SERS} = (Laser spot area/Substrate area) * (N_A * Volume * Concentration)

$$\frac{N_{Bulk}}{N_{SERS}} = \frac{\left(\frac{\pi}{2}\right)^{1.5} w_o^2 \left(\frac{2\pi}{\lambda}\right) w_o^2 \frac{\rho}{M} N_A}{\frac{\pi}{4} w_o^2 \frac{N_A VC}{A}} = \left(\frac{\pi}{2}\right)^{1.5} \left(\frac{8}{\lambda}\right) w_o^2 \frac{\rho}{M} \frac{A}{VC} = \frac{\pi^{1.5}}{\lambda} w_o^2 A \frac{\rho}{w}$$

$$\frac{N_{Bulk}}{N_{SERS}} = \frac{\pi^{1.5}}{\lambda} \left(\frac{1.22\lambda}{NA}\right)^2 A \frac{\rho}{w} = 100 \times \pi^{1.5} \times 1.22^2 \frac{\lambda}{NA^2} \times A \times \frac{\rho}{w} = \frac{2344\lambda}{NA^2} \times A \times \frac{\rho}{w}$$

Where λ is wavelength of the laser light (nm), *NA* is Numerical Aperture, *A* is Area of the film (cm^2), *w* and ρ are the weight of the analyte present in the solution spread on the film (ng) and density of the analyte crystal (g cm^{-3}) respectively.

Intensity of the aromatic C-C stretch vibration of molecules in the reference sample at 1645 cm^{-1} (I_{Bulk}) and in the solutions spread on the Ag-PVA and Ag-Au-PVA substrates at 1650 cm^{-1} (I_{SERS}) were used to estimate the enhancement factor, EF =(N_{Bulk} / N_{SERS})×(I_{SERS} /I_{Bulk}). N_{Bulk} / N_{SERS} was determined as shown in Box 4.1. Table 4.4 lists the specific parameters used in an experiment; the value obtained of N_{Bulk} / N_{SERS} for R6G in the present experiment was found to be 6.4×10^5. As N_{SERS} includes all the probe molecules in the focal volume and not just a monolayer on the nanoparticles, the EF we report is the lower bound of this value. Intensity of the 1645 - 1650 cm^{-1} peak for the reference, I_{Bulk} is found to be 58.88 (Fig 4.8). The EF estimated for the different substrates are collected in Table 4.5; the EF values are typically ~10^8.

Table 4.4. P*arameters used for the estimation of $N_{Bulk}/N_{SERS.}$ for R6G on the Ag-Au-PVA film.*

Parameter	λ (nm)	ρ (g cm^{-3})	w (ng)	NA (20x)	A (cm^2)
Values	488	1.28	43.11	0.4	3

Table 4.5. *Estimation of the SERS enhancement factor (EF) for R6G analyte on Ag-Au-PVA thin film substrates fabricated by spreading different concentrations (c, mM) of $HAuCl_4$ on Ag-PVA thin films.*

c (mM)	**I_{1650}**	**I_{SERS}/I_{Bulk}**	**EF (10^8)**
0.000	15764.58	268	1.71
0.005	17117.10	291	1.86
0.010	19822.16	337	2.15
0.025	27579.22	468	2.84
0.050	20870.31	354	2.27
0.075	12748.13	217	1.39
0.100	5182.47	88	0.56
0.150	161.85	3	0.02
0.200	355.65	6	0.04

4.3.2 *Correlating the Enhancement Factors with LSPR of Substrate*

We have looked at different parameters, to understand the variation of the EF with changing the Au amount in Ag-Au-PVA thin films, like extinction and resonance condition between excitation laser and LSPR of the subtrates. Fig. 4.9 shows the variation of the EF with the concentration (c, mM) of $HAuCl_4$ used in the fabrication of the substrate. The maximum value of 2.84×10^8 is ~70% higher than that obtained with Ag-PVA as the substrate, and is achieved using the Ag-Au-PVA thin film substrate containing 1.62 atom% of Au (based on ICP-OES analysis), corresponding to c = 0.025 mM. Fig. 4.9 shows also the plot of $|\Delta\nu|^{-1}$ against c; $\Delta\nu = \nu_I - \nu_{LSPR}$ (Table 4.6) where ν_I corresponds to the frequency of the excitation laser (λ = 488 nm) and ν_{LSPR} is the frequency of the LSPR peak for each substrate (Fig. 4.2). The maximum EF is obtained with the substrate having an LSPR peak that is slightly blue-shifted with respect to the

excitation laser, rather than with the substrate that has a nearly resonant LSPR (*ie.* with the lowest $\Delta\nu$). This observation is similar to that reported earlier with Au nanosphere[21] and nanostar[22] based colloidal substrates; however, we believe that the maximization of the enhancement off-resonance with respect to the exciting radiation does not arise due to a competition between the extinction and enhancement effects for the following reasons. In the present case, we are working with a planar substrate rather than a colloidal suspension. More importantly, the extinction is found to gradually decrease as the Au content increases (Fig. 4.2) consistent with the simulations based on hollow alloy nanoparticles described above. A subtle trade-off between resonance and extinction appears to lead to the maximization of the SERS EF. Incorporation of small but increasing amounts of Au into Ag moves the LSPR peak closer to the excitation wavelength, but concomitantly decreases the extinction peak intensity; the opposing impacts of the two factors leads to a maximization of the EF at an intermediate Au content. Similar observation in an earlier study,[23] of maximum SERS response with Ag-Au core-shell nanoparticles having intermediate composition, has been attributed to the maximization of pinhole formation. In the present case, as the thickness of the

Table 4.6. *LSPR peak wavelength (λ_{max}), magnitude of the frequency difference between the exciting laser and the LSPR peak ($|\Delta\nu|$) of Ag-PVA and Ag-Au-PVA prepared using different concentrations (c, mM) of $HAuCl_4$ solution.*

c (mM)	**λ_{max} (nm)**	**$|\Delta\nu|$ (cm^{-1})**
0.000	434	2549. 7
0.005	434	2549. 7
0.010	434	2549. 7
0.025	459	1294.7
0.050	473	649.9
0.075	517	1149.4
0.100	628	4568.2
0.150	761	7351.2
0.200	522	1334.7

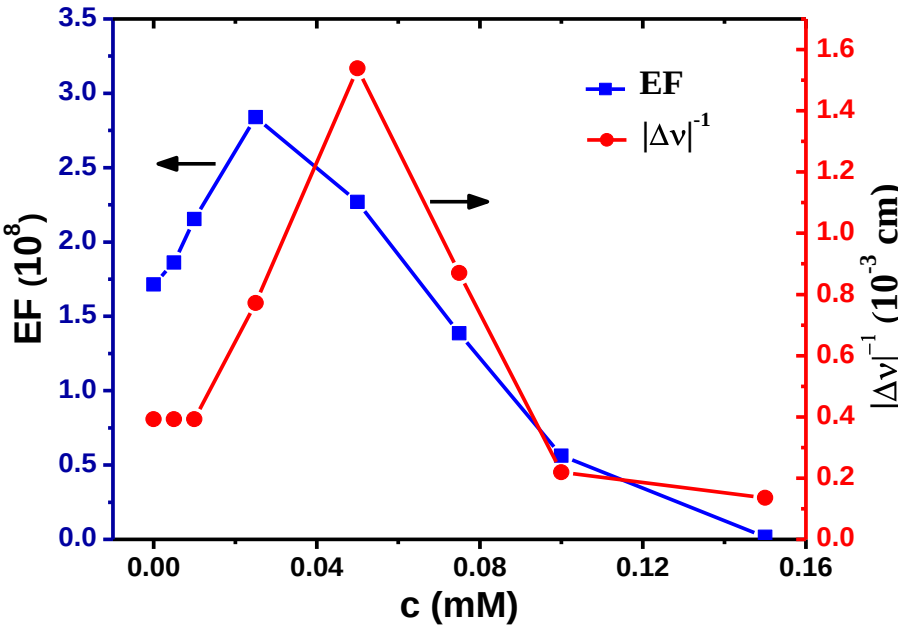

Figure 4.9. *Plot of the SERS EF and $|\Delta\nu|^{-1}$ against the concentration (c, mM) of $HAuCl_4$ used to prepare the Ag-Au-PVA thin film (c = 0 corresponds to the Ag-PVA thin film); $\Delta\nu = \nu_I - \nu_{LSPR}$ where, ν_I = frequency of the excitation laser, ν_{LSPR} = frequency of the LSPR peak for the Ag-PVA or Ag-Au-PVA thin film.*

nanocomposite film is ~ 200 nm and the Ag-Au nanoparticles are 40 – 50 nm in diameter (slightly larger than the Ag nanoparticles), the close contact of particles can give rise to regions of high local electric field and contribute to enhanced SERS effects.

4.3.3 *Limit of Detection*

SERS experiments on several samples of Ag-Au-PVA substrate and multiple measurements on each sample showed a high level of reproducibility (Table 4.7). Experiments were carried out with different concentrations of R6G solutions on the film having the optimal Au concentration (fabricated with c = 0.025 mM); the spectra recorded and the plot of the intensity of the 1650 cm^{-1} peak as a function of the concentration of the R6G solution, including the standard deviation in each case, are shown in Fig. 4.10. The limit of detection is defined as $3\sigma_{blank}/m$ where σ_{blank} is the standard deviation for blank measurements and *m* is the slope of the intensity-

Table 4.7. *Mean I_{SERS} and the corresponding enhancement factor (EF) with standard deviation for different vibrational peaks of R6G on Ag-Au-PVA (c = 0.025 mM) as the substrate.*

Peak (cm^{-1})	I_{SERS} (mean value)	EF (10^8)
610	10024	3.21±0.68
769	8405	2.15±0.31
1186	9172	1.73±0.32
1361	21532	2.70±0.27
1570	15049	2.35±0.18
1650	26111	2.84±0.12

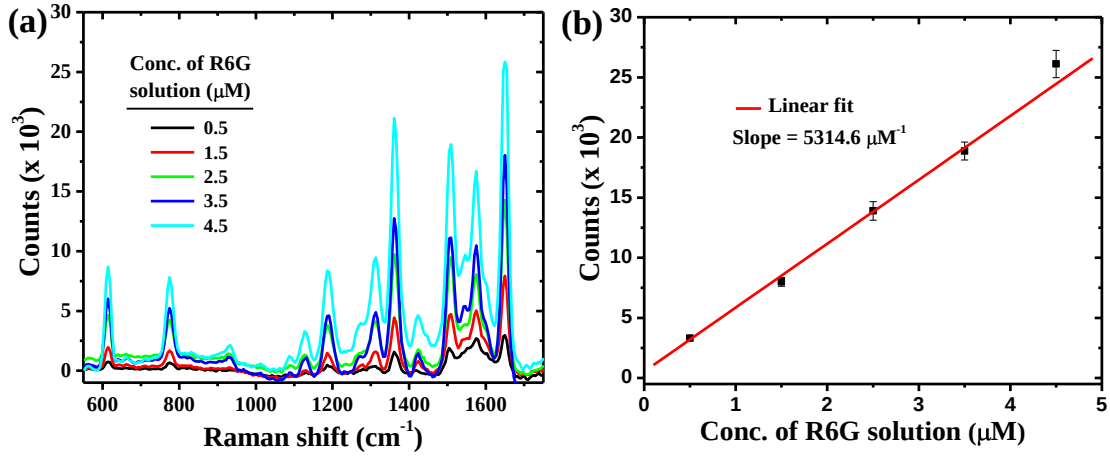

Figure 4.10. ***(a)*** *Raman spectra of R6G solutions with different concentrations adsorbed on Ag-Au-PVA thin film (c = 0.025 mM of $HAuCl_4$) and* ***(b)*** *plot of the intensity of the 1650 cm^{-1} peak as a function of the concentration of R6G solution (the least square fit line is also shown).*

concentration plot.[24,25] σ_{blank} on the Ag-Au-PVA substrate (without probe molecules) was determined by recording the Raman spectra 7 times. The value was estimated to be 52 counts for the intensity at 1650 cm^{-1} (excitation at 488 nm) for R6G. The slope *m* was determined from the calibration plot of signal intensity versus concentration shown in Fig. 4.10b. The LOD estimated for R6G on Ag-Au-PVA is 0.6 pmol. It may be

noted that this value is based on the total solution spread on the substrate; the value would be still lower if only those in the focal volume are considered. The fact that the maximum EF is obtained at very low concentrations of Au in the Ag-Au-PVA, is of great practical utility in terms of cost-effectiveness of the substrate. The ease of fabrication and utilization of the *in situ* fabricated bimetal - polymer nanocomposite thin films is an added benefit.

4.4 Summary

In this chapter we have discussed the *in situ* fabrication of Ag-Au nanoparticles with hollow cage structures and systematically varied composition, embedded within a PVA thin film. The Ag-Au-PVA thin films exhibit systematically tuned LSPR peak across a range of ~ 330 nm. These nanocomposite thin films were used as substrates for SERS experiments with Rhodamine 6G as the analyte molecule. Enhancement factors of ~ 10^8 were obtained. The maximum EF was observed with the substrate having a relatively small Au content. This substrate shows an LSPR extinction peak blue-shifted with respect to the laser excitation wavelength, highlighting the trade-off between the extinction and resonance leading to maximum SERS response. The utility of LSPR tuning in easily fabricated bimetallic nanoparticle-embedded polymer thin films, leading to the fabrication of efficient SERS substrates was demonstrated.

References

1. Campion, A.; Kambhampati, P. *Chem. Soc. Rev.* **1998,** *27,* 241-250.
2. Kneipp, K.; Kneipp, H.; Kneipp, J. *Acc. Chem. Res.* **2006,** *39,* 443-450.
3. Ramesh, G. V.; Porel, S.; Radhakrishnan, T. P. *Chem. Soc. Rev.* **2009,** *38,* 2646−2656.
4. Hariprasad, E.; Radhakrishnan, T. P. *Langmuir* **2013**, *29*, 13050-13057.
5. Porel, S.; Singh, S.; Harsha, S. S.; Rao, D. N.; Radhakrishnan, T. P. *Chem. Mater.* **2005,** *17,* 9−12.
6. Porel, S.; Singh, S.; Radhakrishnan, T. P. *Chem. Commun.* **2005,** 2387–2389.
7. Hariprasad, E.; Radhakrishnan, T. P. *ACS Catal.* **2012,** *2,* 1179−1186.
8. Ramesh, G. V.; Prasad, M. D.; Radhakrishnan, T. P. *Chem. Mater.* **2011**, *23*, 5231-5236.
9. Rao, V. K.; Radhakrishnan, T. P. *J. Mater. Chem. A* **2013,** *1,* 13612−13618.
10. Draine, B. T.; Flatau, P. J. *J. Opt. Soc. Am. A* **1994,** *11*, 1491-1499.
11. DDSCAT (Version 7.3) available from http://code.google.com/p/ddscat/
12. Johnson, P. B.; Christy, R. W. *Phys. Rev. B* **1972**, *6,* 4370−4379.
13. Sun, Y.; Xia, Y. *J. Am. Chem. Soc.* **2004**, *126*, 3892-3901.
14. Yang, J.; Lee, J. Y.; Too, H. *J. Phys. Chem. B* **2005**, *109*, 19208-19212.
15. Zhang, X.; Zhang, G.; Zhang, B.; Su, Z. *Langmuir* **2013**, *29*, 6722−6727.
16. Polavarapu, L.; Liz-Marzán, L. M. *Nanoscale* **2013**, *5*, 4355–4361.
17. Gonzalez, E.; Arbiol, J.; Puntes, V. F. *Science* **2011**, *334***,** 1377-1380.
18. Michalak, I.; Chojnacka, K.; Marycz, K. *Michrochim. Acta*. **2011**, *173*, 65-74.
19. McFarland, A. D.; Young, M. A.; Dieringer, J. A.; Van Duyne, R. P. *J. Phys. Chem. B* **2005,** *109,* 11279−11285.

20. Zhao, J.; Dieringer, J. A.; Zhang, X.; Schatz, G. C.; Van Duyne, R. P. *J. Phys. Chem. C* **2008,** *112*, 19302−19310.

21. van Dijk, T.; Sivapalan, S. T.; DeVetter, B. M.; Yang, T. K.; Schulmerich, M. V.; Murphy, C. J.; Bhargava, R.; Carney, P. S. *J. Phys. Chem. Lett.* **2013,** *4*, 1193−1196.

22. Li, M.; Kang, J. W.; Dasari, R. R.; Barman, I. *Angew. Chem. Int. Ed.* **2014**, *53*, 14115–14119.

23. Cui, Y.; Ren, B.; Yao, J.-L.; Gu, R.-A.; Tian, Z.-Q. *J. Phys. Chem. B* **2006**, *110*, 4002−4006.

24. El-Safty, S. A.; Ismail, A. A.; Matsunaga, H.; Nanjo, H.; Mizukami, F. *J. Phys. Chem. C* **2008**, *112*, 4825-4835.

25. Christian, G. D. *Analytical Chemistry*, 6th ed.; John Wiley & Sons Inc.: New York, 2003.

CHAPTER 5

In Situ Fabricated Copper-Silver Nanoparticle-Embedded Polymer Thin Film as an Efficient Broad Spectrum SERS Substrate

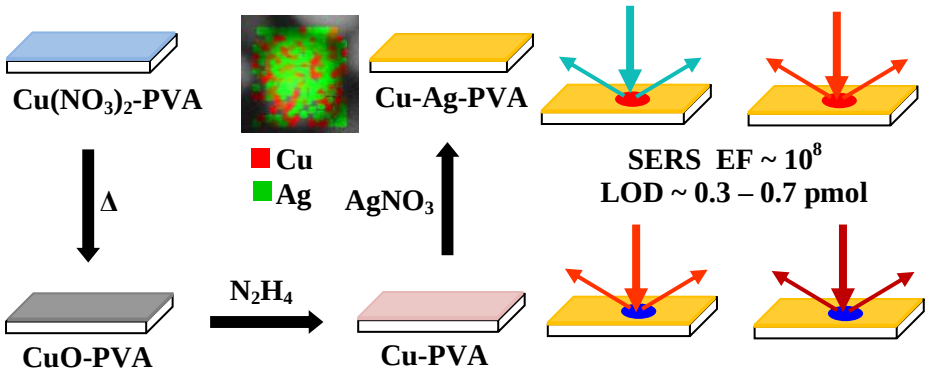

Cu-Ag-polymer nanocomposite thin film fabricated by a novel in situ protocol is an efficient SERS substrate for sensitive detection of different analytes with a range of excitation wavelengths.

Paper published

Rao, V. K.; Ghildiyal, P.; Radhakrishnan, T. P. *J.Phys.Chem. C* (accepted).

Scope

Fabrication of copper as well as copper-silver nanoparticles embedded in polymer thin films and their application in surface-enhanced Raman scattering (SERS) form the subject of this chapter. As discussed in the previous chapter, the thin films of metal-polymer nanocomposites are good candidates for efficient SERS substrates; it would be highly advantageous if they can be fabricated by a cost-effective and facile protocol, and high enhancement factors (EF) can be realized for a range of excitation wavelengths, enabling sensitive detection of different analytes. We have fabricated poly(vinyl alcohol) (PVA) thin films with embedded Cu-Ag nanoparticles through an in situ procedure via step-wise formation of CuO-PVA and Cu-PVA; the fabrication was monitored through the different stages, by spectroscopy, microscopy, electron diffraction and elemental analysis. Choice of the Cu-Ag combination was dictated by its broad plasmonic extinction, favorable cost factor, and chemical stability of the nanocomposite; the hydrogel character of PVA facilitates analyte absorption and contact with the nanoparticles leading to efficient SERS. Cu-Ag-PVA thin film with an optimal composition displays plasmonic extinction over an appreciable part of the visible range and provides EF of the order of 10^7-10^8 for the analytes, Rhodamine 6G and methylene blue, at three different excitation wavelengths; the EF values are significantly higher than that reported earlier, with most of the Cu-Ag based SERS substrates. The novel bimetal-polymer nanocomposite thin film is an efficient SERS substrate providing sub-picomol limits of detection.

5.1 Introduction

Surface enhanced Raman scattering (SERS) is a facile and powerful analytical tool for the sensitive detection of molecules, thanks to the combination of unique Raman spectral signature of molecules with extremely large signal enhancements. The latter is often achieved through the interaction of the molecules with metal nanoparticles and nanostructures, and the field associated with their localized surface plasmon

resonance (LSPR) extinction as discussed in Sec. 1.6.3. Metals such as Au, Ag and Cu with LSPR extinction in the 400 – 700 nm range are suitable for visible light excitation; even though Ag and Cu provide obvious cost advantages, the relatively higher reactivity is a cause for concern in practical applications. The large extinction cross-section associated with silver nanoparticles has been exploited extensively;[1] copper nanoparticles and nanostructures have also been shown to be efficient substrates for SERS.[2,3] As the LSPR extinction of Ag and Cu nanoparticles peak at ~ 400 nm and ~ 600 nm respectively, an optimal combination of the two should provide local field enhancement over a significant part of the visible spectrum, and lead to efficient SERS with different excitation wavelengths;[4] strong dependence of the SERS enhancement factor (EF) on the excitation wavelength is well-established.[5,6] A Cu-Ag nanostructure with appropriate composition would serve as an efficient SERS substrate for different analyte molecules, through resonance effects; practical application would be facilitated if the substrate is stable and in the form of a solid thin film.

Cu and Ag form a binary alloy system with a eutectic at 42 atom% Cu.[7,8] The relatively lower surface energy and larger atomic size of Ag induce phase separation in the alloy, and core-shell structures emerge in nanoparticles within some size limits.[9] Formation of Ag shell on Cu nanoparticles imparts stability against oxidation, as has been shown in the case of air-stable dispersions for inkjet printing.[10] Treatment of Cu with Ag^+ ions is a facile route to deposit Ag on Cu through galvanic displacement; this approach has been adopted in various ways, to fabricate SERS substrates based on the Cu-Ag bimetallic system. The most common protocol involves formation of Ag nano/microstructures with a variety of morphologies, on the surface of Cu in the form of grid,[11] foil,[12-14] plate,[15,16] membrane,[17] layer deposits[18-20] and powder;[21] Ag nanoparticles have been formed also on Cu nanowalls in a microfluidic device.[22] Cu-Ag nanoparticles,[23,24] dendrites[25,26] and core-shell structures[4,27] formed in a fluid phase have also been developed for SERS application. Bimetallic nanoparticles embedded in a suitable thin film matrix that can efficiently absorb analyte molecules, should prove to be a versatile SERS substrate. An optimal substrate that provides high EF for different

analyte molecules employing different excitation wavelengths, remains an important goal.

In situ formation of metal[28-30] and bimetallic[31,32] nanoparticles inside polymer thin films is a facile route to the fabrication of efficient SERS substrates.[33] Fabrication of Ag, Au, Pd and Pt nanoparticles inside a poly(vinyl alcohol) (PVA) thin film by mild thermal annealing using the polymer itself as the reducing and stabilizing agent was discussed in Sec.1.5.[30] This method is ineffective in the case of Cu in view of its relatively lower reduction potential. Therefore, we have optimized a new methodology for the formation of Cu nanoparticle-embedded PVA thin film (Cu-PVA) through the intermediate formation of CuO-PVA. Brief treatment of the Cu-PVA film with $AgNO_3$ solution of varying concentration under ambient conditions led to the formation of Cu-Ag-PVA thin films with different Cu-Ag compositions. The Cu-Ag-PVA thin films provide SERS EF of the order of 10^7-10^8 (higher than that reported earlier, with many of the Cu-Ag based substrates) for two different analyte molecules, with three different laser excitation wavelengths; improved efficiency over the corresponding single metal systems, Cu-PVA and Ag-PVA with similar metal loading was demonstrated.

5.2 Cu-PVA Thin Film

Among the metals fabricated and studied as nanoparticles and nanostructures, Au and Ag dominate significantly above all others. Even though relatively less, nanoparticles of the remaining coinage metal, Cu have also been studied extensively.[34] The lower reduction potential of Cu^+/Cu and Cu^{2+}/Cu compared to Ag^+/Ag or Au^{3+}/Au, necessitates stronger reducing agents for the formation of Cu. The associated ease of oxidation of Cu makes the stabilization of Cu nanoparticles more difficult. However, if formed inside the polymer film, the Cu nanoparticles are likely to be relatively more stable against atmospheric oxidation. Cu nanoparticles can be generated by the direct treatment of Cu^{2+} salts such as $Cu(NO_3)_2$ introduced in a PVA film by strong reducing agents like hydrazine; however, the quality of the Cu-PVA films thus obtained was poor. Therefore, we have developed a two-step protocol (Fig. 5.1) for the fabrication of

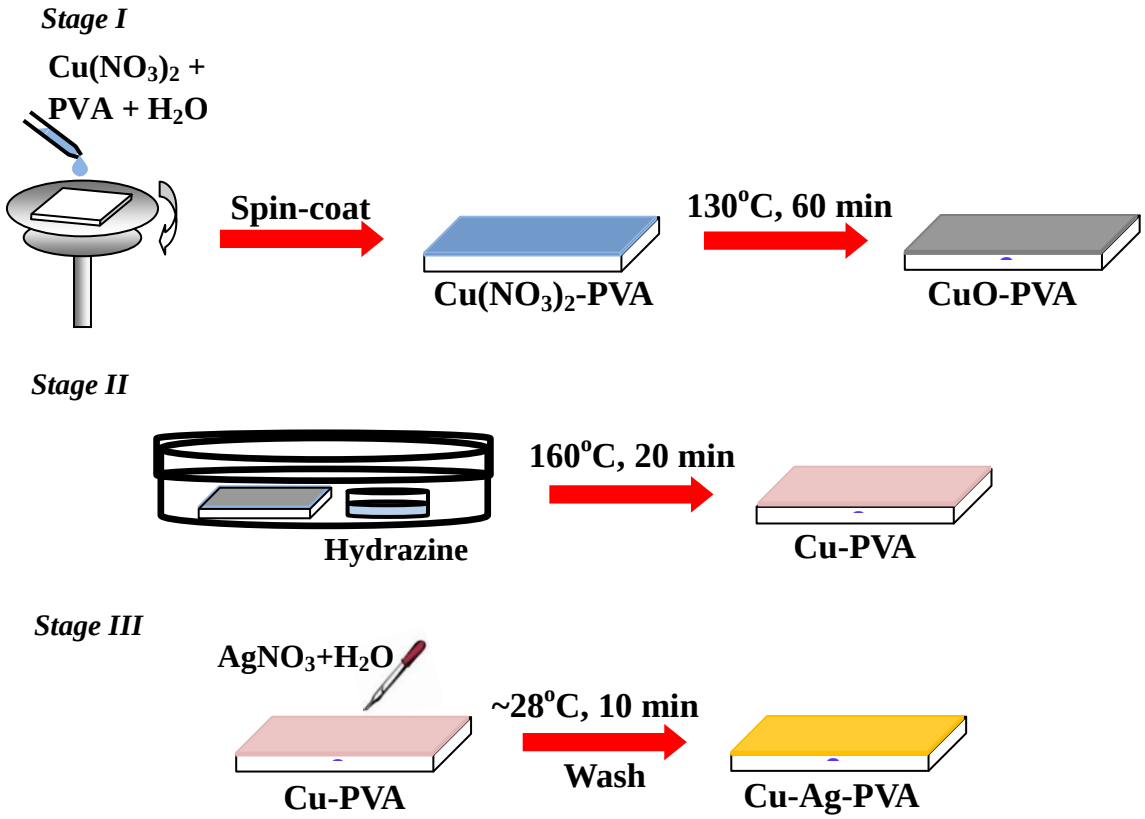

Figure 5.1. *Schematic showing the fabrication of Cu-PVA thin film and its conversion to Cu-Ag-PVA thin film.*

uniform and good quality Cu-PVA thin films. In the first step CuO-PVA was fabricating by thermal annealing of $Cu(NO_3)_2$-PVA which was treated with hydrazine to obtain the Cu-PVA in the second step.

5.2.1 *Fabrication of CuO-PVA Thin Film*

The procedure used for the preparation CuO-PVA thin film is as follows. Required weight of $Cu(NO_3)_2.3H_2O$ dissolved in 1.6 mL of water was mixed with 0.20 g of PVA (average molecular weight = 85 - 146 kDa, % hydrolysis = 99+) dissolved in 4.0 mL of water to prepare different compositions designated using the Cu/PVA weight ratios, x (for example, 76 mg of $Cu(NO_3)_2.3H_2O$ gives x = 0.10). The solution mixture was spin-coated on the glass/ quartz/ Si wafer substrates at 500 rpm for 10 s, followed

by 6000 rpm for 10 s. The film was then heated in a convection oven at 130^{o}C for 60 min.

In order to check the effect of PVA on decomposition, we have carried out control experiments, thermal annealing of pure $Cu(NO_3)_2.3H_2O$ as well as its mixture with PVA, at various temperatures. Color change observed in the pure $Cu(NO_3)_2.3H_2O$ powder heated at 130^{o}C is due to the formation of basic copper nitrate (change from blue to cyan as shown in Fig. 5.2a,b) and the black material obtained when heated at 200^{o}C is cupric oxide (CuO) (Fig 5.2c). Heating the mixture of $Cu(NO_3)_2.3H_2O$ and PVA at 130^{o}C produces a black solid suggesting the formation of CuO (Fig. 5.2e). Thermal decomposition appears to be facilitated by the addition of PVA; this may arise due to the coordination of the alcoholic groups on PVA to Cu^{2+}. Absence of the characteristic red color of Cu_2O rules out the possibility of reduction of Cu^{2+} by PVA during this process.

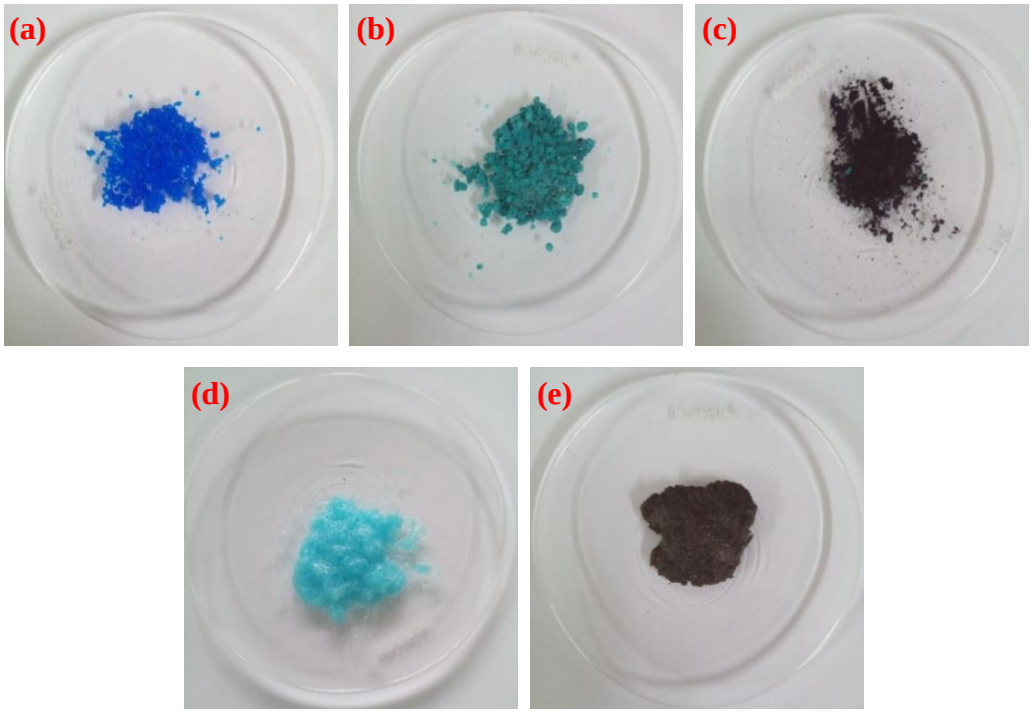

Figure 5.2. *Photographs of $Cu(NO_3)_2{\cdot}3H_2O$: **(a)** Unheated **(b)** heated at 130^{o}C for 120 min; **(c)** heated at 200^{o}C for 60 min; $Cu(NO_3)_2{\cdot}3H_2O$ + PVA: **(d)** Unheated; **(e)** heated at 130^{o}C for 60 min.*

5.2.2 *Spectroscopy and Microscopy Studies of CuO-PVA Thin Film*

We have experimented with spin-coated thin films of $Cu(NO_3)_2$-PVA with three different weight ratios, *x*, heated at 130°C for 60 min. Formation of CuO nanoparticles by the thermal decomposition of $Cu(NO_3)_2$ is clearly demonstrated by the development of the characteristic band absorption starting at 300 - 550 nm, increasing with *x* (Fig. 5.3a). Tauc plots indicate direct band gaps in the range 3.36 – 4.01 eV for the different

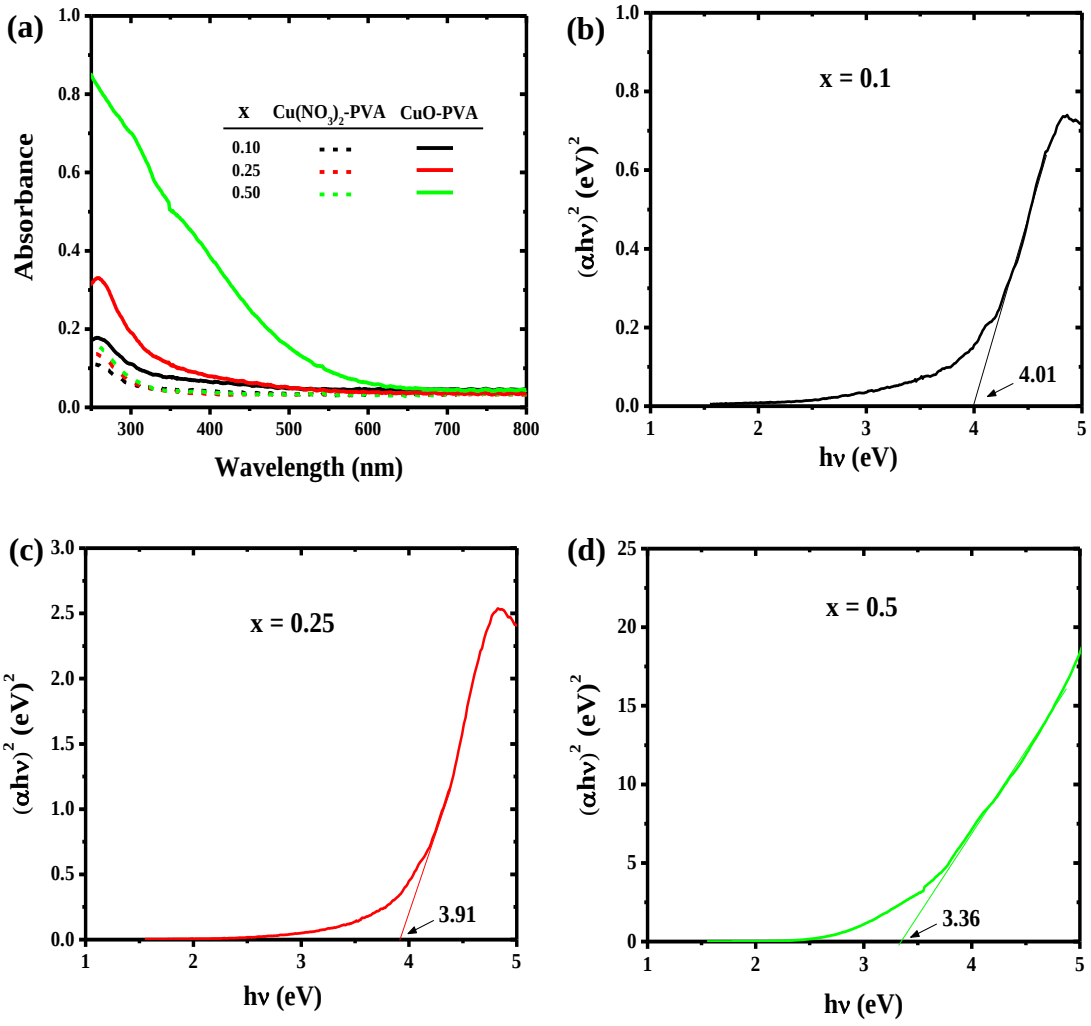

Figure 5.3. *Electronic absorption spectra of* ***(a)*** *$Cu(NO_3)_2$-PVA and CuO-PVA; and Tauc plots for the direct band gap of the CuO-PVA film with different values of x* ***(b)*** *0.1,* ***(c)*** *0.25 and* ***(d)*** *0.50.*

compositions (Fig. 5.3b-d). These values are consistent with those reported for CuO nanoparticles;[35,36] the decrease in the band gap with increasing *x* indicate the effect of particle size increase. TEM images of the films reveal small particles, 1 - 10 nm in size depending on *x* (Fig. 5.4). The high resolution TEM image of the particles in the film with x = 0.5 shows the spacing corresponding to the (110), ($\bar{1}11$), and ($\bar{1}13$) lattice planes of CuO (particles in the case of films with lower *x* are too small to provide lattice resolution images). The electron diffraction pattern shown in the inset of Fig. 5.4c can be indexed to monoclinic CuO (JCPDS file no: 89-2531): 2.76 Å (110), 2.50 Å ($\bar{1}11$), and 1.48 Å ($\bar{1}13$).

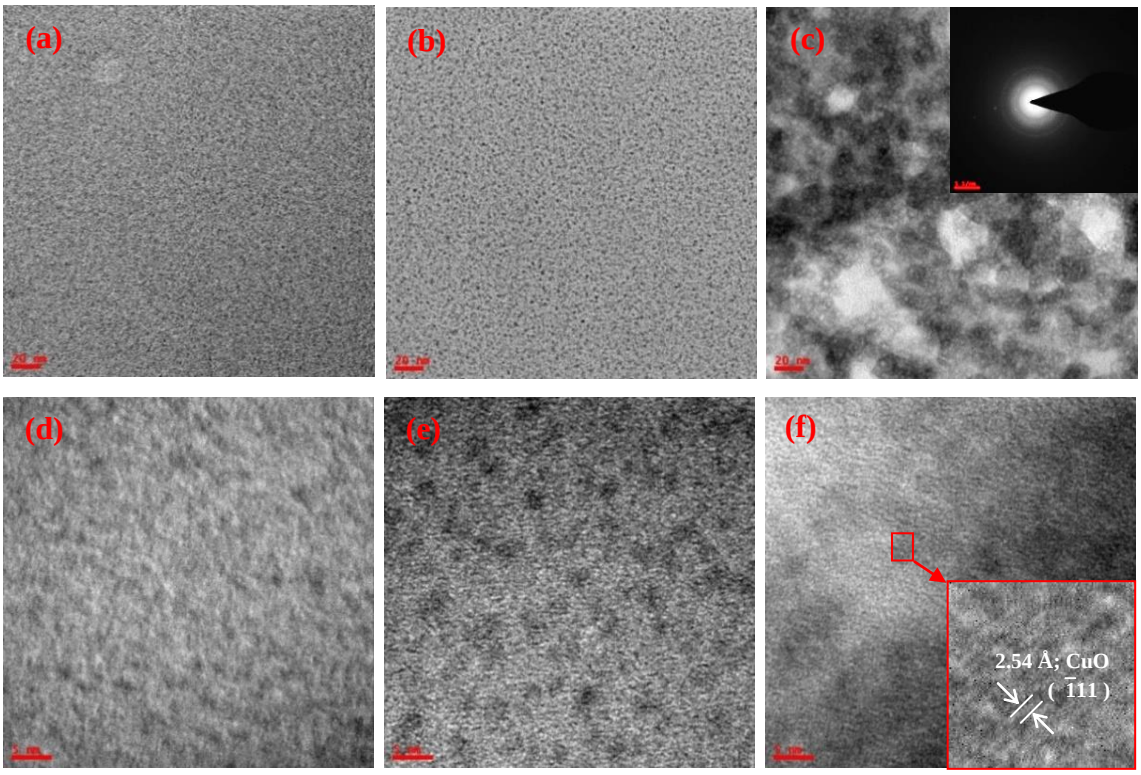

Figure 5.4. *TEM images (scale = 20 nm) of CuO-PVA thin films with weight ratios (x),* ***(a)*** *0.10,* ***(b)*** *0.25 and* ***(c)*** *0.50; the corresponding magnified images (scale = 5 nm) are shown in* ***(d – f)****; electron diffraction pattern and lattice spacing are indicated in the insets in* ***(c)*** *and* ***(f)*** *respectively.*

5.2.3 *Fabrication of Cu-PVA Thin Film*

In the second stage (Fig. 5.1), CuO-PVA thin film could be converted to Cu-PVA thin film by the *in situ* reduction of Cu^{2+} to Cu inside the film, using hydrazine vapor. The fabrication procedure of Cu-PVA thin film was as follows. CuO-PVA film (x = 0.10, 0.25 and 0.50) coated on the substrate was kept in a closed petri dish (150 mm dia, 15 mm high) together with 3 mL of 80 % hydrazine hydrate taken in an open petri dish (50 mm dia, 12 mm high). The whole system was kept in a convection oven at 160^{o}C for 20 min (Fig. 5.1), resulting in the transformation of CuO-PVA to Cu-PVA.

5.2.4 *Spectroscopy and Microscopy Studies of Cu-PVA Thin Film*

The reduction of Cu^{2+} to Cu is probed initially by recording the extinction spectrum of the thin film. The spectra in Fig. 5.5, may be contrasted with the ones in Fig. 5.3a; they show clearly, the emergence of the LSPR peak at ~ 580 – 590 nm due to Cu nanoparticles. The peak intensity is directly related to the value of x; the scattering contribution increases significantly at higher values of x. The LSPR extinction spectrum of Cu-PVA thin film is stable for several hours, but shows small variation

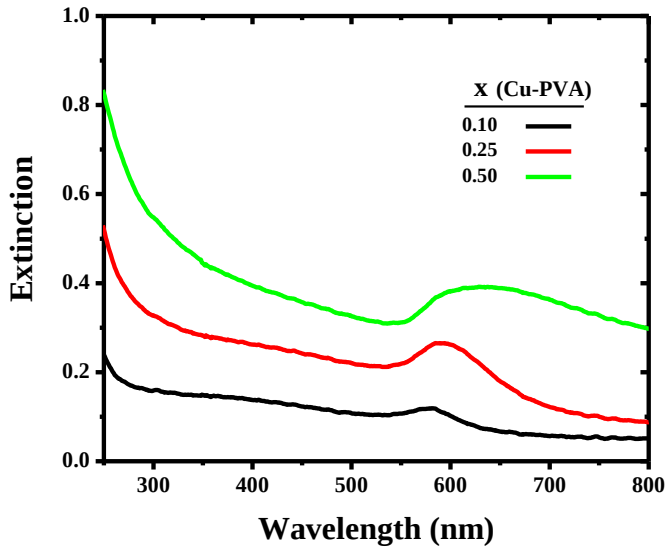

Figure 5.5. *Extinction spectra of Cu-PVA thin films with different weight ratios (x) of Cu/PVA.*

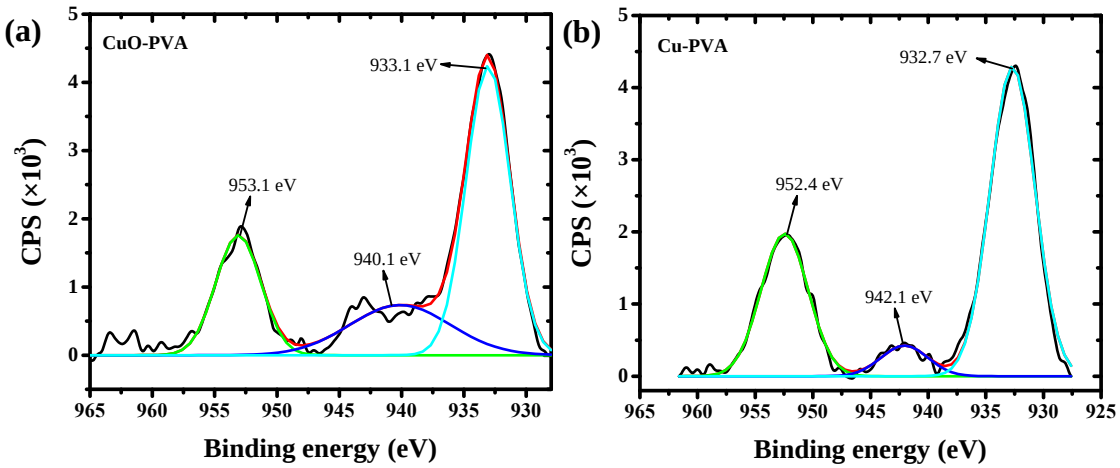

Figure 5.6 *X-ray photoelectron spectra of* ***(a)*** *CuO-PVA and* ***(b)*** *Cu-PVA thin films with x = 0.25.*

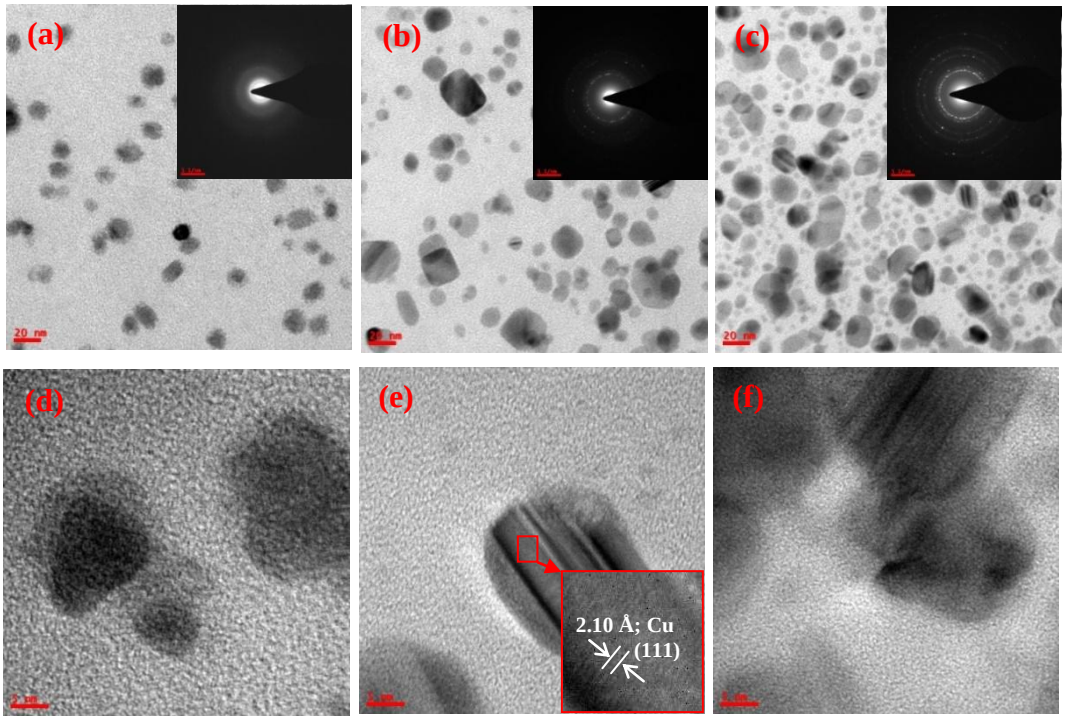

Figure 5.7. *TEM images (scale = 20 nm) of Cu-PVA thin films with weight ratios (x),* ***(a)*** *0.10,* ***(b)*** *0.25 and* ***(c)*** *0.50; the corresponding magnified images (scale = 5 nm) are shown in* ***(d – f)****; electron diffraction pattern and lattice spacing are indicated in the insets in* ***(a-c)*** *and* ***(e)*** *respectively.*

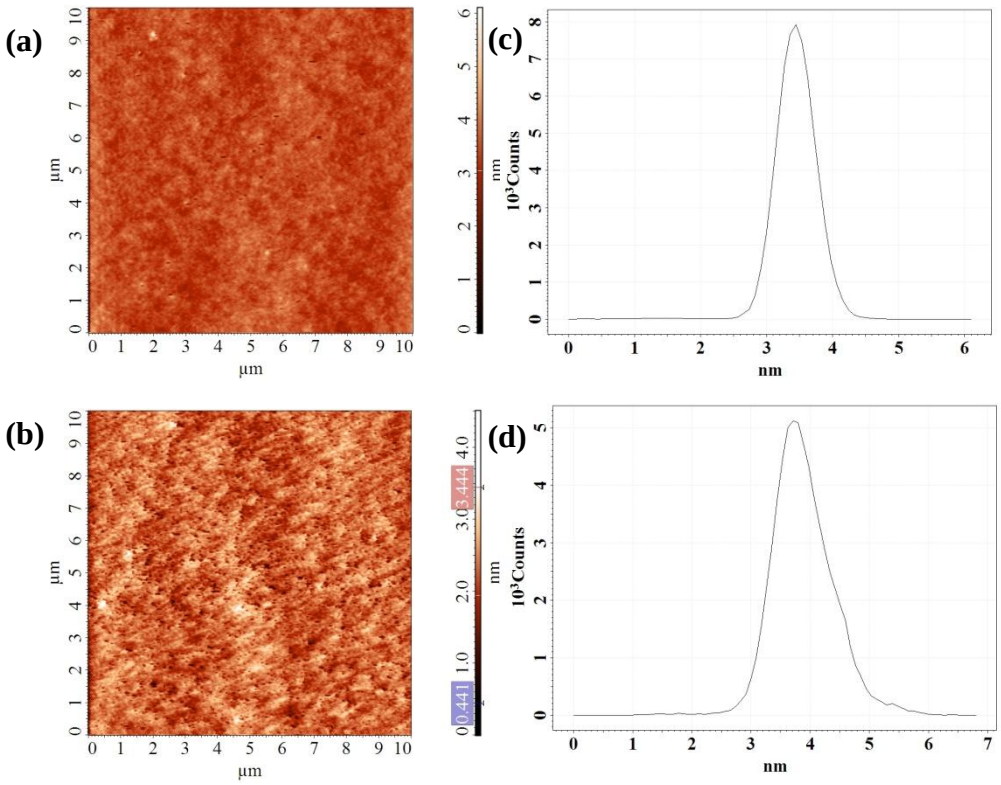

Figure 5.8. *AFM images of* ***(a)*** *CuO-PVA and* ***(b)*** *Cu-PVA thin films;* ***(c)*** *and* ***(d)*** *the corresponding histogram of the surface (height) roughness.*

Table 5.1. *Average roughness with standard deviation (σ) inferred from the AFM images taken at 5 different regions (10 × 10 µm^2) on the CuO-PVA and Cu-PVA thin films.*

Image	**Average roughness (nm)**	
	CuO-PVA	**Cu-PVA**
1	0.63	0.44
2	0.24	0.40
3	0.65	0.41
4	0.26	0.55
5	0.34	0.69
Average for the 5 measurements (σ)	0.42 (0.20)	0.50 (0.12)

over a few days (discussed later). Fig. 5.6 shows the X-ray photoelectron spectra (XPS) of CuO-PVA and Cu-PVA thin films (x = 0.25). The CuO-PVA film shows broad $2p_{3/2}$ and $2p_{1/2}$ peaks with maxima at 933.1 and 953.1 eV and a satellite with peak at ~ 940.1 eV; the broader peak is associated with the presence of Cu(II).[37] Cu-PVA film (x = 0.25) shows $2p_{3/2}$ and $2p_{1/2}$ peaks of Cu at 932.7 and 952.4 eV; the satellite with peak at ~ 942.1 eV appears to be due to the partial oxidation of the Cu in the sample.[10] TEM images of the Cu-PVA films show the presence of Cu nanoparticles with sizes in the range 10 - 30 nm (Fig. 5.7). Identity of Cu is proved by the high resolution TEM image showing the (111) lattice plane of Cu with a spacing of 2.10 Å (Fig. 5.7e). The electron diffraction pattern shown in Fig. 5.7a-c are consistent with Cu: 2.10 Å (111), 1.81 Å (200), 1.28 Å (220) and 1.07 Å (311). AFM images of CuO-PVA and Cu-PVA thin films (Fig. 5.8) reveal an average roughness of 0.42 nm and 0.5 nm respectively, indicating the smooth surface of the films; roughness measured at 5 different regions on the films are collected in Table 5.1.

5.3 Cu-Ag-PVA Thin Film

5.3.1 *Fabrication of Cu-Ag-PVA Thin Film*

We have generated Cu-Ag nanoparticles by treating the Cu-PVA thin films with $AgNO_3$ solution having different concentrations; as the film with x = 0.25 showed the clear plasmon peak due to Cu with relatively low scattering (Fig. 5.5), it was chosen for this third stage of fabrication (Fig. 5.1). 0.5 mL of an aqueous solution of $AgNO_3$ with concentrations (c) ranging from 1 – 30 mM was spread uniformly on the Cu-PVA film and kept for 10 min under ambient temperature (~ 28^oC) inside a closed petri dish to avoid evaporation of the solution. The bimetallic nanoparticles of Cu-Ag are formed by the galvanic displacement of part of the Cu atoms by the Ag atoms. The film was then washed with ~ 1 mL of water to remove any unreacted $AgNO_3$ solution present on the film as well as the byproducts including Cu^{2+} and HNO_3, and dried under ambient atmosphere.

5.3.2 *Spectroscopy, Microscopy and Chemical Analysis of Cu-Ag-PVA Thin Film*

Galvanic displacement of Cu by Ag is revealed by the emergence of the LSPR extinction due to Ag with λ_{max} at ~ 400 – 450 nm (Fig. 5.9). Amplitude as well as width of the extinction and hence the coverage over the 350 – 700 nm increases with the concentration, c up to 12 mM; the spectrum changes very little beyond this point, indicating saturation (in fact the 450 nm peak decreases marginally and more scattering is observed at higher wavelengths). The nanocomposite films are extremely stable as shown by the reproducibility of the extinction spectrum even after several days (Fig. 5.10a,b) or on exposure to O_2 gas (Fig. 5.11a), the stability being attributable to the incorporation of Ag with a higher reduction potential than Cu; exposure to reactive gases like H_2S however does affect the film (Fig. 5.11b). It is seen that the extinction of Cu-PVA shows gradual decrease over a period of a few days indicating relatively lower stability (Fig. 5.10c). X-ray photoelectron spectra of the Cu-Ag-PVA film (Fig. 5.12) shows the Cu $2p_{3/2}$ and $2p_{1/2}$ peaks at 933.1 and 953.0 eV and a weak satellite

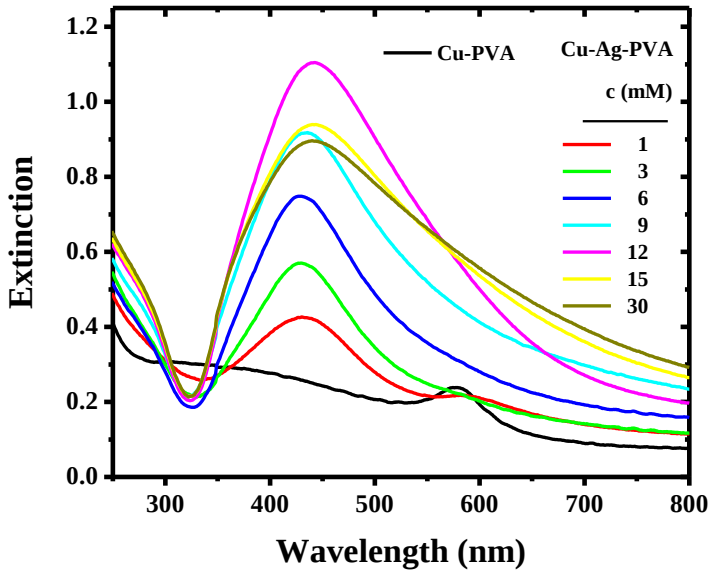

Figure 5.9. *Extinction spectra of Cu-PVA (x = 0.25) and Cu-Ag-PVA thin films fabricated by treating the Cu-PVA film with different concentrations (c, mM) of $AgNO_3$ solution.*

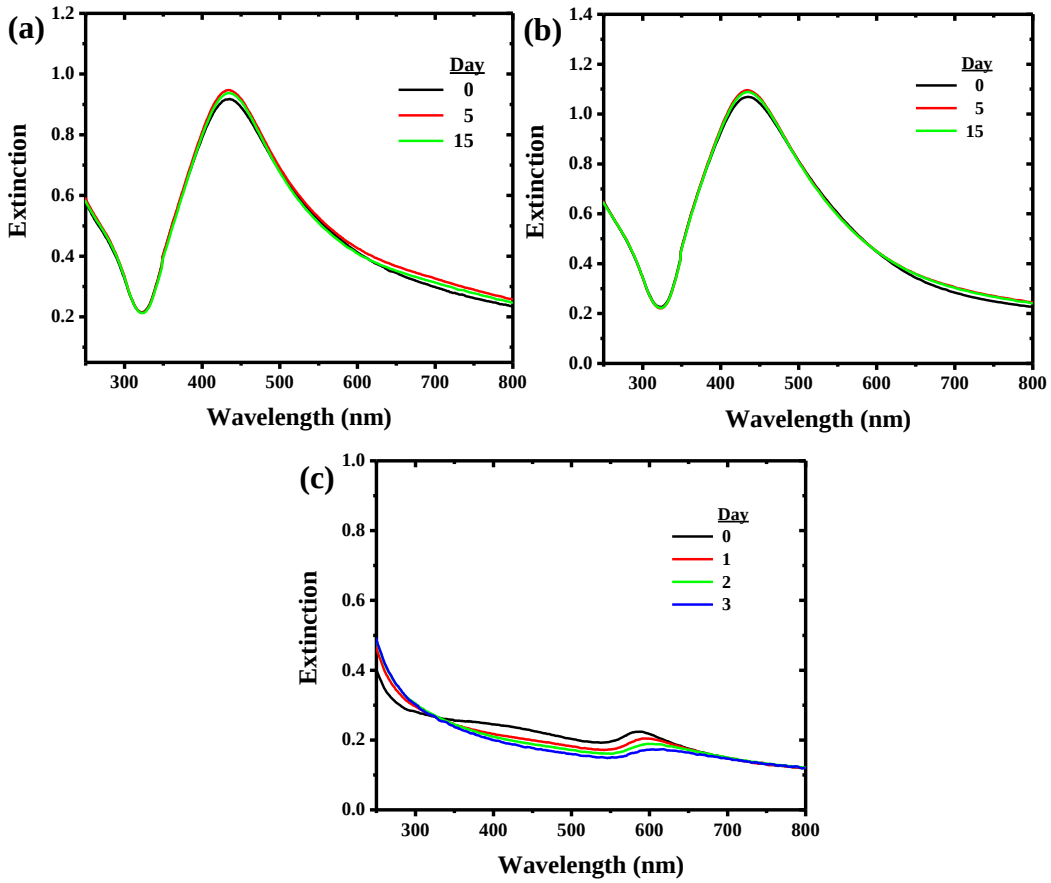

Figure 5.10. *Extinction spectra of Cu-Ag-PVA thin films formed by treating the Cu-PVA with different concentrations (c, mM) of $AgNO_3$ solution:* ***(a)*** *9 and* ***(b)*** *12, and* ***(c)*** *Cu-PVA (x = 0.25), recorded over different time intervals.*

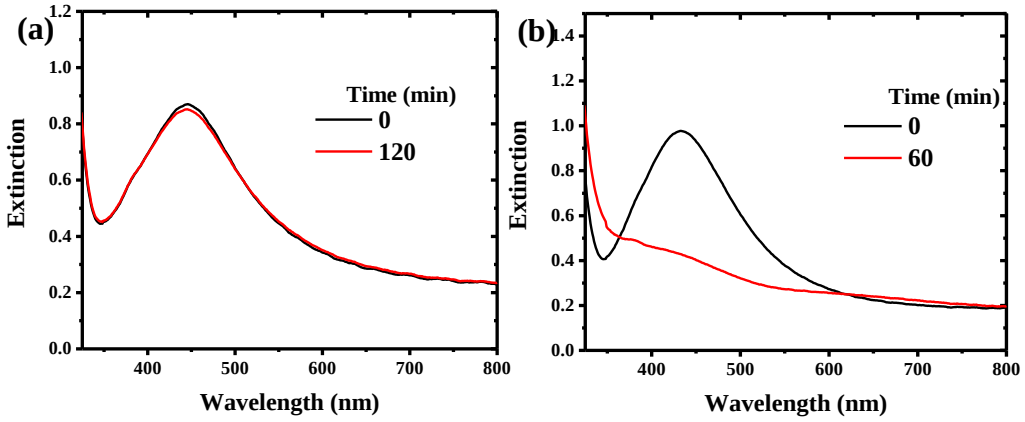

Figure 5.11. *Extinction spectra of Cu-Ag-PVA (x = 0.25, c = 12 mM) thin film exposed to* ***(a)*** *O_2 and* ***(b)*** *H_2S gas.*

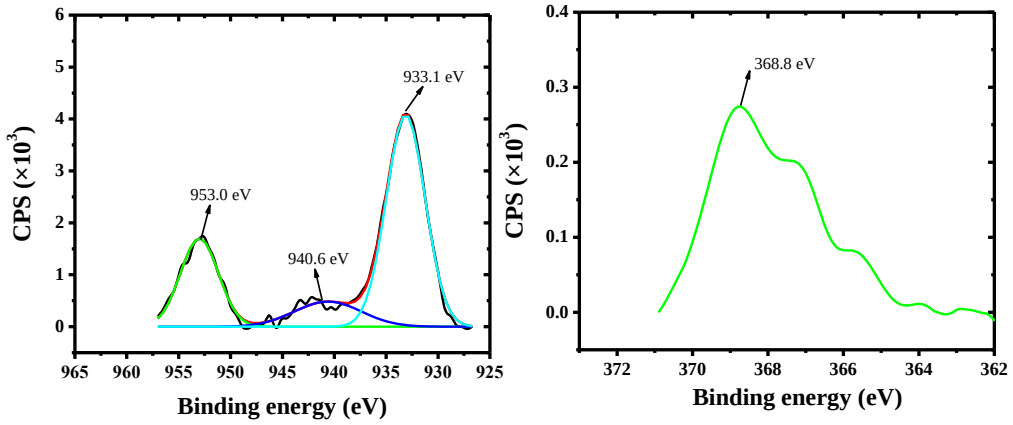

Figure 5.12. *X-ray photoelectron spectra of Cu-Ag-PVA (x = 0.25, c = 12 mM) thin film (two energy region are shown).*

peak at ~ 940.6 eV (most likely due to CuO); peak due to Ag $3d_{5/2}$ is clearly observed at 368.8 eV. The shift in energies observed for the peaks with respect to Cu(0) and Ag(0) may be attributed to the presence of each other.

We have collected the TEM images of the Cu-Ag-PVA thin films in Fig. 5.13 and 5.14; the electron diffraction patterns are shown in the insets of the former, and the latter with higher magnification show the lattice planes. Nearly spherical particles are observed in all cases, with the average particle size increasing from (a) to (e); the spectral changes are consistent with this. The lattice spacing of 2.34 Å can be attributed to the (111) planes of Ag; the spacing of 2.08 – 2.10 Å could be either due to the (200) planes of Ag or the (111) planes of Cu (Table 5.2).[25] EDXS data clearly show the presence of Cu and Ag, with the atom % of Ag in the films fabricated with c = 1 to 12 mM, increasing from 29 to 81 respectively (Table 5.3). The Cu-Ag composition variation can be clearly visualized from the FESEM images combined with EDXS mapping shown in Fig. 5.15; it is also seen that the two elements are distributed fairly evenly throughout the particle. A parallel trend in the Cu-Ag composition is observed in the ICP analysis data obtained using bulk film samples of Cu-Ag-PVA (Table 5.3); differences in the absolute values from EDXS may be attributed to the fact that the latter probes primarily the surface region of the thin films.

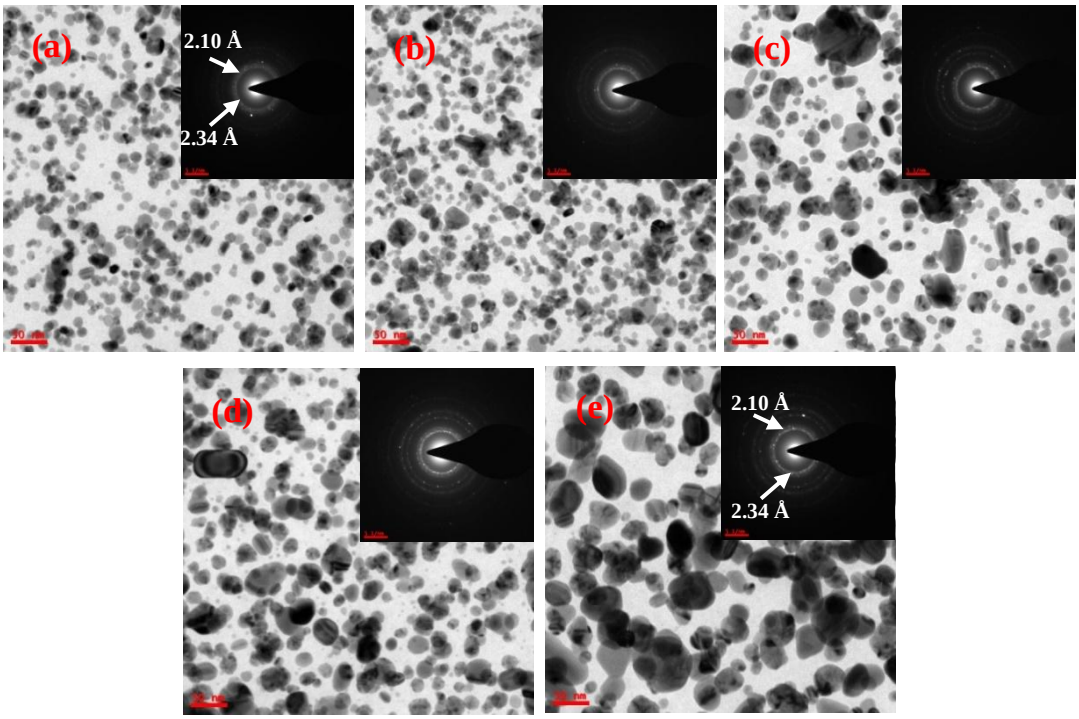

Figure 5.13. *TEM images (scale = 50 nm) of Cu-Ag-PVA thin films fabricated by treating Cu-PVA (x = 0.25) with different concentrations (c, mM) of $AgNO_3$ solution:* ***(a)*** *1,* ***(b)*** *3,* ***(c)*** *6,* ***(d)*** *9 and* ***(e)*** *12. Electron diffraction patterns are indicated in the insets.*

Table 5.2. *Indexing of the electron diffraction pattern and lattice planes shown in Fig. 5.13 and 5.14.*

d (Å)	h k l
2.34	1 1 1 (Ag)
2.10	1 1 1 (Cu)
2.04	2 0 0 (Ag)
1.82	2 0 0 (Cu)
1.43	2 2 0 (Ag)
1.23	2 2 0 (Cu)
	3 1 1 (Ag)
1.04	2 2 2 (Cu)
	4 0 0 (Ag)

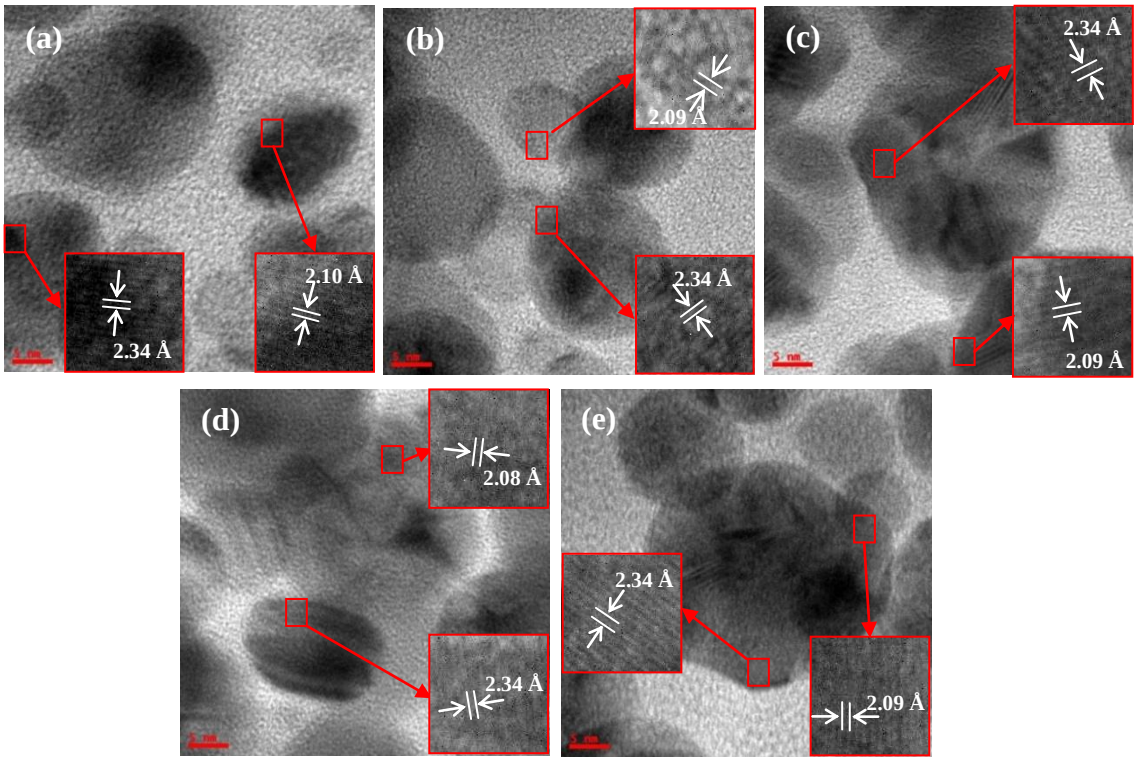

Figure 5.14. *TEM images (scale = 5 nm) of Cu-Ag-PVA thin films fabricated by treating Cu-PVA (x = 0.25) with different concentrations (c, mM) of $AgNO_3$ solution:* ***(a)*** *1,* ***(b)*** *3,* ***(c)*** *6,* ***(d)*** *9 and* ***(e)*** *12; lattice spacing values are indicated and discussed in the text.*

Table 5.3. *Atom % of Cu and Ag in the Cu-Ag-PVA thin films fabricated by spreading different concentrations (c, mM) of $AgNO_3$ on Cu-PVA thin films, estimated using ICP-OES, EDX (TEM) and EDX (FESEM) analysis.*

Substrate		**Atom%**					
		ICP-OES		**EDX (TEM)**		**EDX (FESEM)**	
		Cu	**Ag**	**Cu**	**Ag**	**Cu**	**Ag**
Cu-PVA		100	0	100	0	100	0
Cu-Ag-PVA [c (mM)]	1	78	22	71	29	70	30
	3	-	-	56	44	62	38
	6	54	46	34	66	45	55
	9	45	55	24	76	28	72
	12	35	65	19	81	24	76

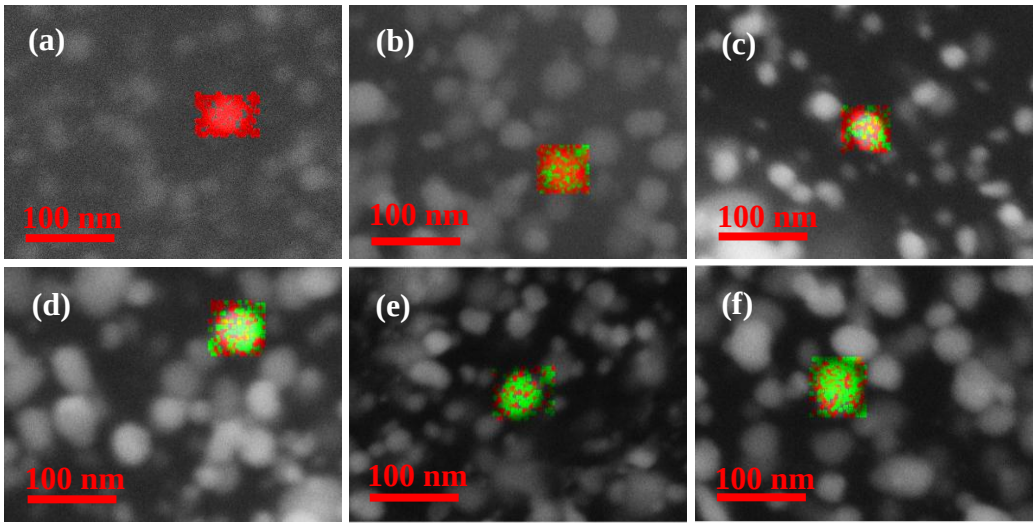

Figure 5.15. *FE-SEM images combined with EDXS area mapping, of* ***(a)*** *Cu-PVA (x = 0.25) and Cu-Ag-PVA thin films formed by treating the Cu-PVA with different concentrations (c, mM) of* $AgNO_3$ *solution:* ***(b)*** *1,* ***(c)*** *3,* ***(d)*** *6,* ***(e)*** *9 and* ***(f)*** *12; scale bar = 100 nm. The EDXS mapping shows Cu (red) and Ag (green) regions in a selected particle.*

5.4 Ag-PVA Thin Film

5.4.1 *Fabrication of Ag-PVA Thin Film*

We have also fabricated Ag-PVA thin films in order to perform control experiments in the study of the SERS application of Cu-Ag-PVA thin film discussed in the next section. 160 mg $AgNO_3$ dissolved in 0.8 mL water was mixed with a solution of 0.10 g of PVA in 2 mL water (Ag/PVA weight ratio = 1.0). The solution mixture was spin-coated on glass/ quartz/ Si wafer substrates as described in Sec. 5.2 and heated at 130^{o}C for 60 min. In an alternate approach, the film was exposed to hydrazine vapor at ~ 28^{o}C for 10 min.

5.4.2 *Spectroscopy, Microscopy and Chemical Analysis of Ag-PVA Thin Film*

Extinction spectra of the Ag-PVA films fabricated by thermal annealing as well as exposure to hydrazine vapor are shown in Fig. 5.16. Both show the clear peak due to

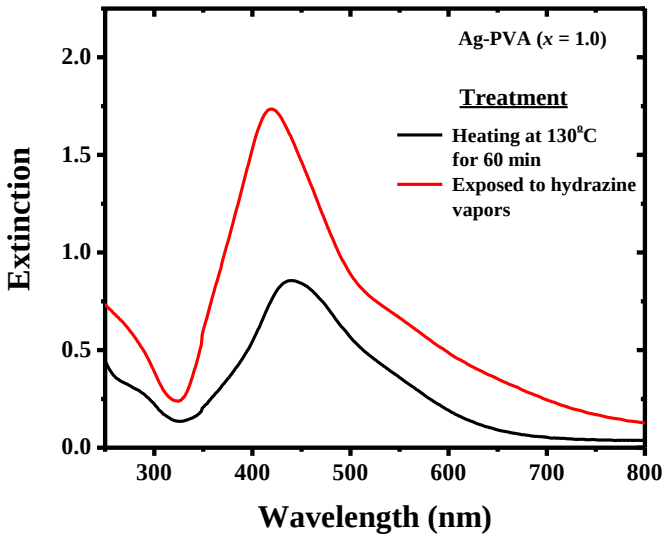

Figure 5.16. *Extinction spectra of Ag-PVA thin film.*

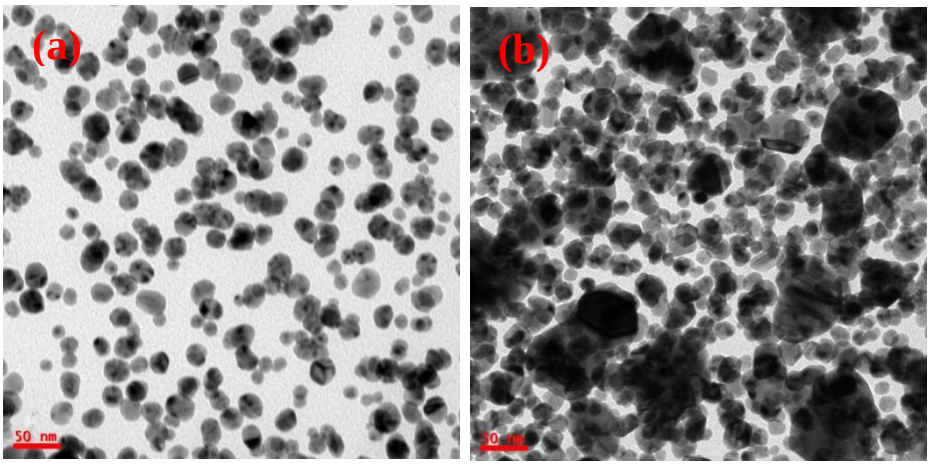

Figure 5.17. *TEM images (scale = 50 nm) of Ag-PVA thin films fabricated by* ***(a)*** *thermal treatment and* ***(b)*** *exposure to hydrazine vapors at room temperature.*

the LSPR extinction of Ag nanoparticles. The film fabricated by exposing to hydrazine vapor has higher extinction compared with that fabricated under thermal annealing. Fig 5.17a,b shows the TEM images of the Ag-PVA thin films. The Ag nanoparticles formed by exposure to hydrazine vapor are relatively larger than that obtained in thermal annealing; the particles size distribution in the former case is similar to that of Cu-Ag-PVA thin film (fabricated with c = 12 mM). Content of Ag and Cu in the

Table 5.4. *The metal contents found by ICP-OES analysis, in Cu-PVA (x=0.25) and Cu-Ag-PVA (fabricated using $AgNO_3$ solution of concentration, c) and Ag-PVA thin film formed by hydrazine vapor treatment, coated on 3 × 1 cm^2 quartz plate; the films were dissolved in 69% nitric acid to do analysis.*

Substrate		Atom content in the film (μmol)	
		Cu	Ag
Cu-PVA		0.6590	0
Cu-Ag-PVA [c (mM)]	1	0.6987	0.1954
	6	0.4572	0.3888
	9	0.3632	0.4432
	12	0.2931	0.5431
Ag/PVA	1.0	0	0.8292

various thin films analysed using ICP-OES are collected in Table 5.4. It is seen that the amount of Ag in Ag-PVA is higher than that in all the Cu-Ag-PVA films. Hence it would serve as a good control sample for the SERS studies.

5.5 SERS Studies

The Cu-PVA, Cu-Ag-PVA and Ag-PVA thin films coated on glass substrates are ~ 300 nm thick. As shown in Sec. 5.3.2, the Cu-Ag-PVA films exhibit strong LSPR extinction over a broad range in the visible regime, due to the embedded bimetallic nanoparticles; the hydrogel character of PVA facilitates efficient swelling and absorption of analyte solutions. These characteristics are expected to make these nanocomposite thin films cheap, easily fabricated and efficient substrates for the sensitive SERS detection of analytes using different excitation wavelengths. SERS experiments were conducted using Cu-Ag-PVA (with different Ag content) coated on silicon wafer as the substrate; control experiments were carried out using Cu-PVA and Ag-PVA films also coated on silicon wafer. Rhodamine 6G (R6G) and methylene blue (MB) were used as the analytes. Their absorption spectra (Fig 5.18) show strong visible light absorption at 460 - 560 nm and 580 - 680 nm respectively. Solution with

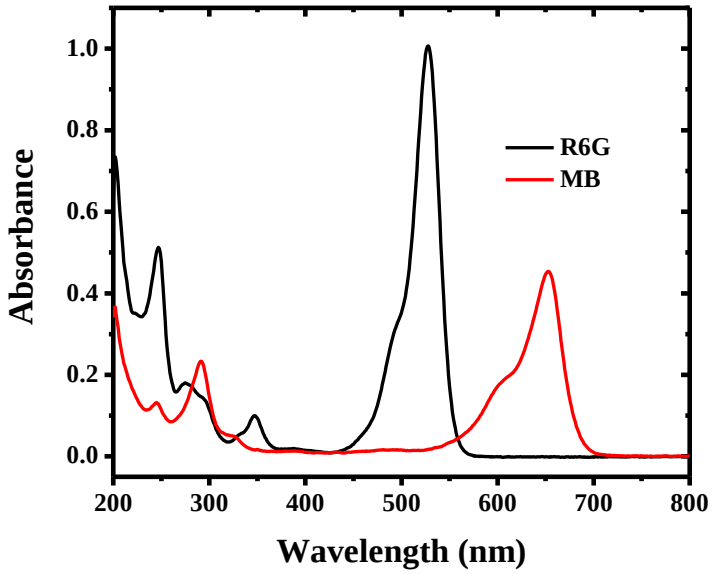

Figure 5.18. *Absorption spectra of R6G and MB aqueous solutions.*

concentrations of 8.6 µM and 6.3 µM respectively were used in the SERS experiments (the concentrations were confirmed by the measured absorbances and reported extinction coefficients). 20µL of each of the analyte solutions were spread uniformly on the thin film substrates listed above, and allowed to dry under ambient atmosphere. A WITec model Alpha 300 R Raman microscope was used for recording the Raman spectra, with 0.5 s integration time and 10 accumulations, through a 20× aperture (NA = 0.4). Three different line lasers (488, 633 and 785 nm) were used as the excitation source; the power at focus (spot diameter) was 4.8 mW (1.49 µm), 13.4 mW (1.93 µm) and 10.5 mW (2.39 µm) respectively. The laser intensity was maintained constant in all the measurements; 100 µm (for 488 nm) and 50 µm (for 633 and 785 nm) detecting fibers were used to collect the spectra. Raman spectra for the bulk material used as reference, were recorded using a small R6G and MB microcrystal placed on the Si wafer.

Raman spectra recorded with the pure PVA film as well as Cu-Ag-PVA film showed negligible background, but the spectra of the films with the analyte had a broad background due to fluorescence (Fig. 5.19); the spectra presented are corrected for this background, and used for analyzing the spectral line intensities to calculate EF. Raman

spectra recorded for R6G and MB on different thin film substrates are collected in Fig. 5.20 and 5.21, respectively; spectra obtained with three different excitations are shown in each case. Spectrum recorded for the reference microcrystal is shown in each panel; the peaks are hardly visible, but can be discerned on expanding the scale. Spectrum of R6G (λ_{exc} = 488 nm) recorded with Cu-PVA as the substrate shows slightly improved intensities. Incorporation of Ag by treatment with $AgNO_3$ of increasing concentrations led to significant increase in the spectral intensity with the maximum observed with c =

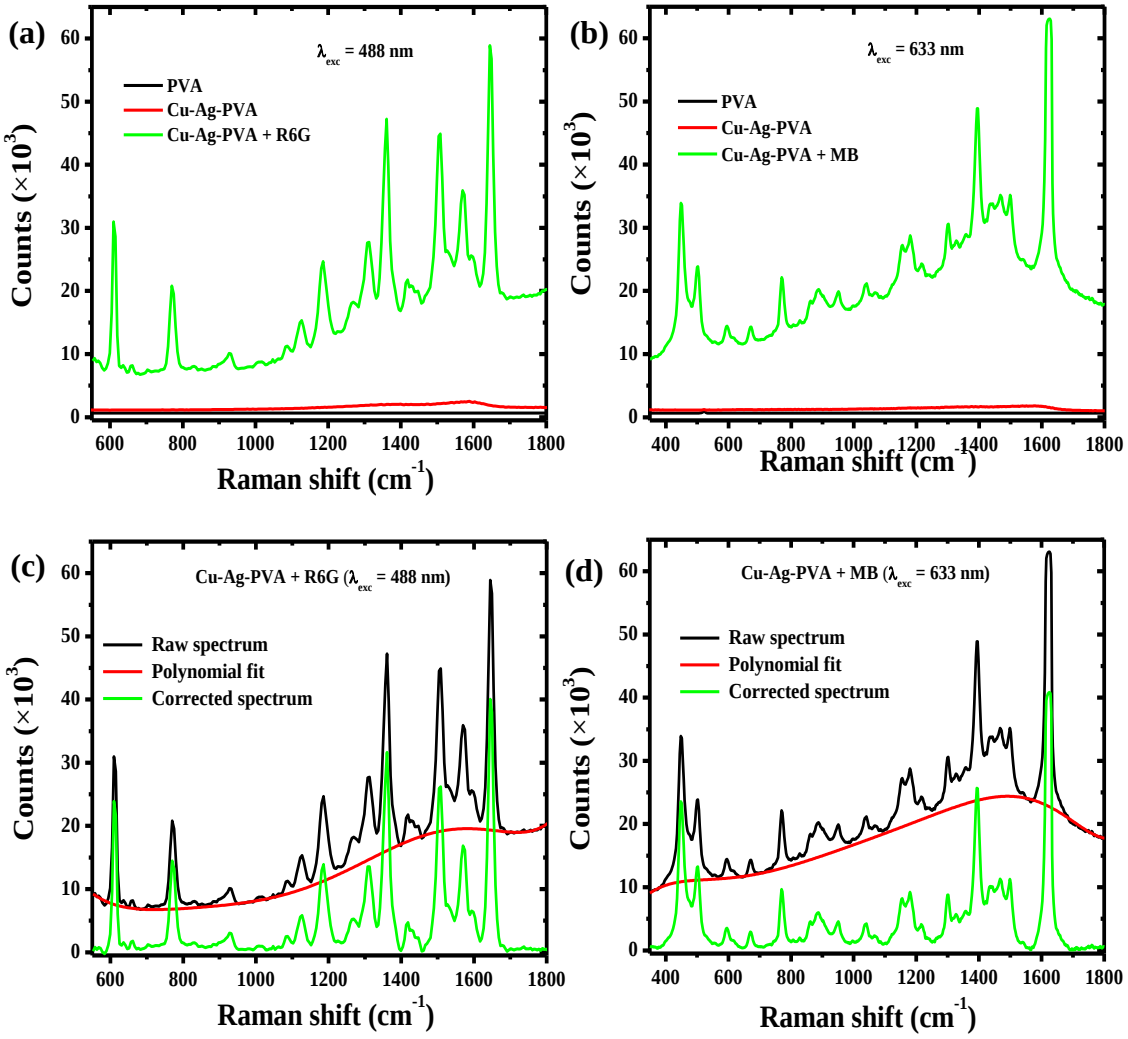

Figure 5.19. *Raman spectra of PVA and Cu-Ag-PVA thin films (without and with)* ***(a)*** *R6G (8.6 µM) and* ***(b)*** *MB (6.3 µM), recorded using 488 and 633 nm laser excitations respectively. The raw and corrected (for background due to fluorescence) spectra of* ***(c)*** *R6G and* ***(d)*** *MB on Cu-Ag-PVA are also shown.*

12 mM; aggregation of particles in the films fabricated with c > 12 mM possibly lead to decreasing SERS efficiency. The spectrum recorded on Ag-PVA (with similar content of Ag as that of Cu-Ag-PVA, c = 12 mM) is significantly weaker, with intensity comparable to the Cu-Ag-PVA film formed by treatment with 1 mM $AgNO_3$; a comparison of the spectra obtained on Cu-Ag-PVA (c = 12 mM) film and Ag-PVA film having similar size nanoparticles (Fig. 5.17) shows the former to be significantly stronger, revealing the critical role of the bimetallic composition. Parallel trends are seen in the case of MB (λ_{exc} = 633 nm).

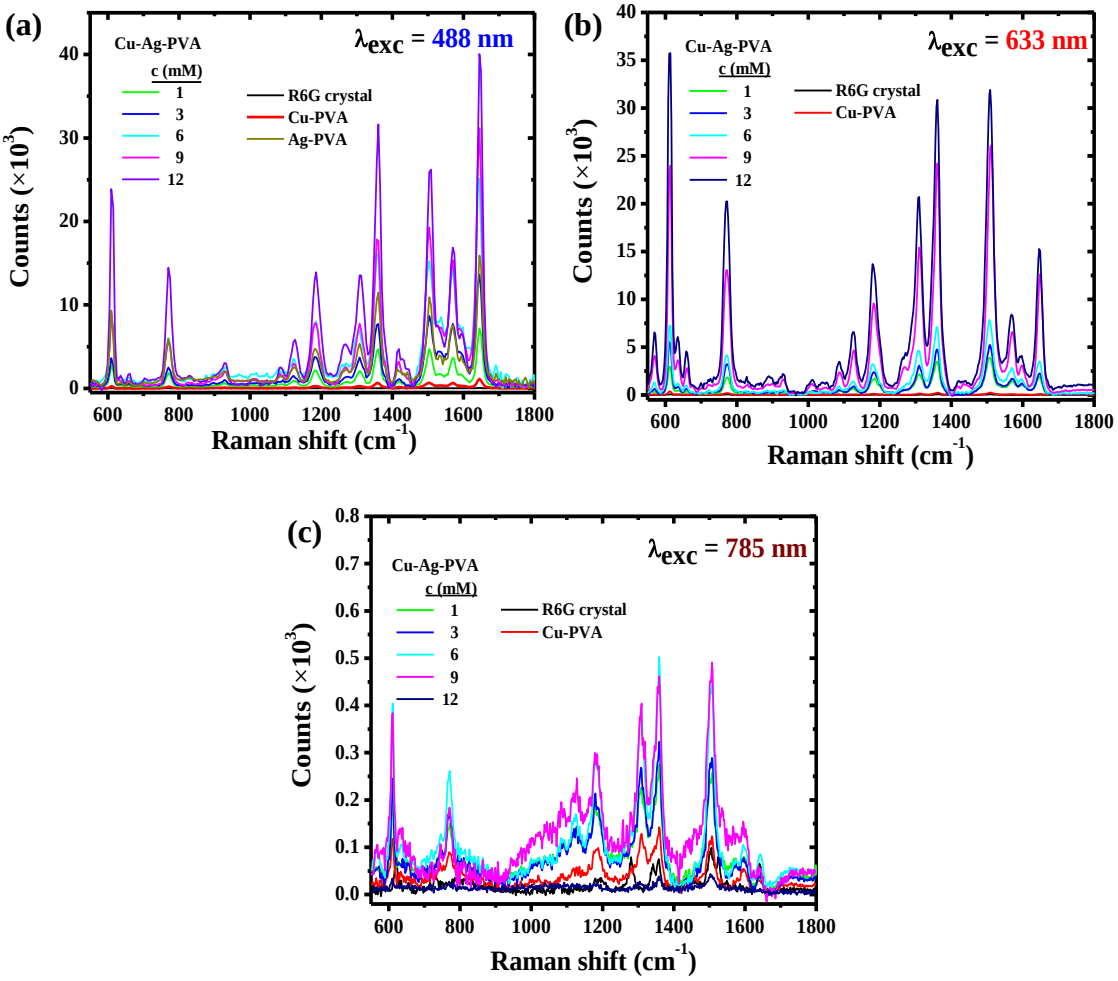

Figure 5.20. *Raman spectra of R6G solution (8.6 µM) on Cu-PVA (x = 0.25), Ag-PVA and Cu-Ag-PVA thin films fabricated by treatment of the Cu-PVA with different concentrations (c, mM) of $AgNO_3$, using* ***(a)*** *433,* ***(b)*** *633 and* ***(c)*** *785 nm lasers as excitation.*

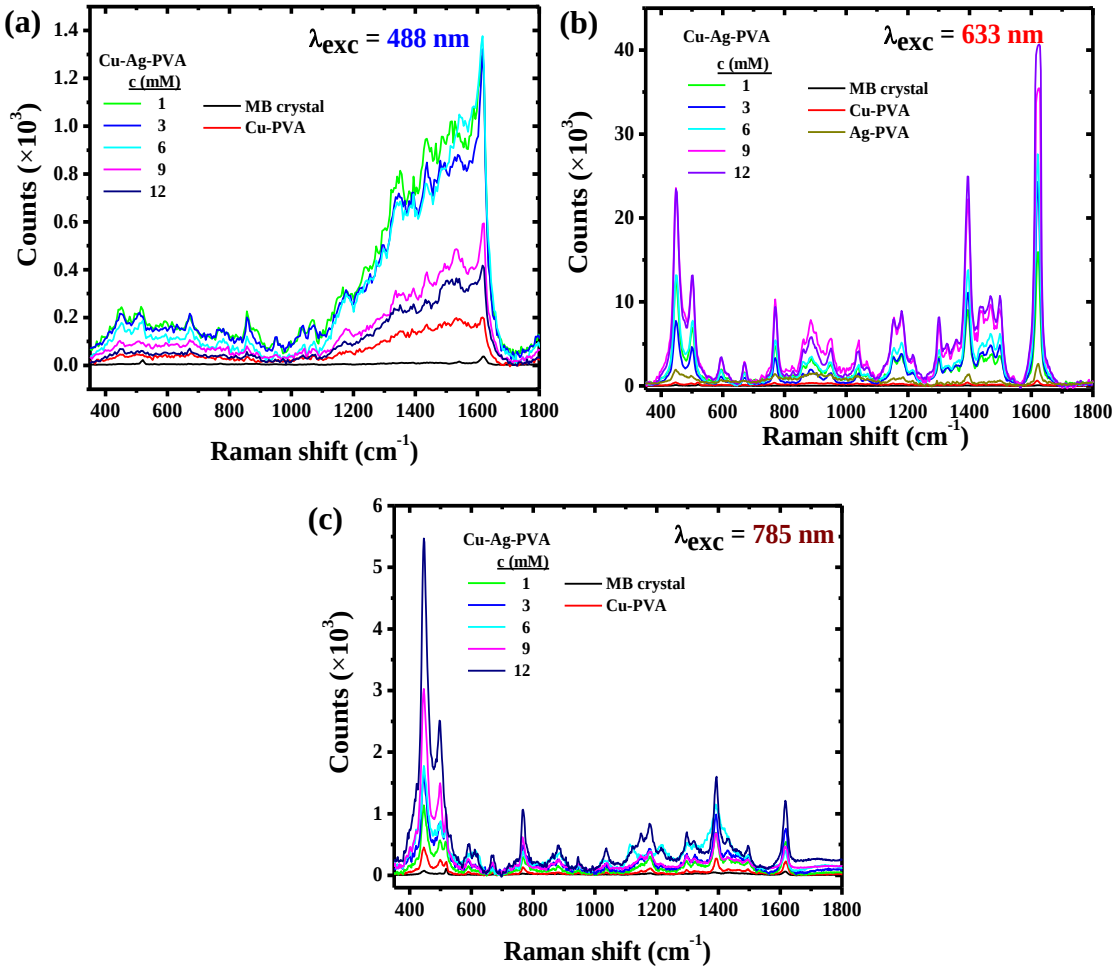

Figure 5.21. *Raman spectra of MB solution (6.3 µM) on Cu-PVA (x = 0.25), Ag-PVA and Cu-Ag-PVA thin films fabricated by treatment of the Cu-PVA with different concentrations (c, mM) of $AgNO_3$, using* ***(a)*** *433,* ***(b)*** *633 and* ***(c)*** *785 nm lasers as excitation.*

Experiments were carried out with the other two laser excitations in each case. In the case of R6G, 785 nm excitation produces relatively weak spectral lines (Fig. 5.20c); the spectral intensities are very high with the excitations at 633 (Fig. 5.20b) and 488 nm (Fig. 5.20a), the low energy vibrations being stronger with the former and the high energy vibrations with the latter. With MB, 488 nm excitation produces weaker spectra (Fig. 5.21a) than 633 nm (Fig. 5.21b) and 785 nm (Fig. 5.21c) excitations; in the

latter two cases once again, the lower energy vibrations dominate with the higher excitation wavelength and *vice versa*. These observations of selective enhancement of vibrational modes related to the excitation wavelength are consistent with earlier observations on R6G on Ag colloids, and MB on random array of gold nanoparticles covered with silica.[6,38]

5.5.1 *Calculation of Enhancement Factor*

The EF values were calculated using the approach discussed in Sec. 4.3, EF is given by the general expression,

$$EF = \frac{N_{Bulk}}{N_{SERS}} \times \frac{I_{SERS}}{I_{Bulk}} \qquad \text{where} \qquad \frac{N_{Bulk}}{N_{SERS}} = \frac{2344\,\lambda}{NA^2} \times A \times \frac{\rho}{w}$$

To estimate the EF, intensity of different vibrational peaks were chosen, based on the excitation wavelength and analyte. N_{Bulk}/N_{SERS} was estimated for the probe molecules by substituting the values given in Table 5.5. Table 5.6 shows the vibrational peak chosen, intensity of the peak for the bulk crystal and the value of N_{Bulk}/N_{SERS} under the

Table 5.5. P*arameters used for the estimation of N_{Bulk}/N_{SERS} for R6G and MB on Cu-Ag-PVA film.*

Analytes	**Parameters**			
	ρ (g cm^{-3})	***w* (ng)**	**NA (20x)**	**A (cm^2)**
R6G	1.28	82.39	0.4	3
MB	0.98	40.3	0.4	3

Table 5.6. *The vibrational peaks chosen, Raman intensity of this peaks for the reference bulk crystal, and the values of N_{Bulk}/N_{SERS} estimated for R6G and MB, for the three excitation lasers.*

λ_{exc} (nm)	**R6G**			**MB**		
	Peak (cm^{-1})	**I_{Bulk}**	**N_{Bulk} / N_{SERS} (×10^5)**	**Peak (cm^{-1})**	**I_{Bulk}**	**N_{Bulk} / N_{SERS} (×10^5)**
488	1645	58.72	3.33	1620	37.09	5.22
633	1509	86.30	4.32	1623	78.95	6.77
785	1506	99.00	5.36	445	74.59	8.39

Table 5.7. *Estimation of the SERS enhancement factor (EF) for R6G analyte on different substrates (λ_{exc} : 488 nm and peak : 1645 cm^{-1}).*

Substrate		R6G (λ_{exc} : 488 nm)		
		I_{1645}	I_{SERS}/I_{Bulk}	EF ($\times 10^8$)
Cu-PVA		1137	19	0.06
Cu-Ag-PVA [c (mM)]	1	7180	122	0.41
	3	13643	232	0.77
	6	25314	431	1.44
	9	31169	531	1.77
	12	40063	682	2.27
Ag-PVA		15140	258	0.86

Table 5.8. *Estimation of the SERS enhancement factor (EF) for R6G analyte on different substrates (λ_{exc} : 633 nm and peak : 1509 cm^{-1}).*

Substrate		R6G (λ_{exc} : 633 nm)		
		I_{1509}	I_{SERS}/I_{Bulk}	EF ($\times 10^8$)
Cu-PVA		258	3	0.01
Cu-Ag-PVA [c (mM)]	1	3911	45	0.19
	3	5219	60	0.26
	6	7635	88	0.38
	9	26110	303	1.31
	12	31904	370	1.60

Table 5.9. *Estimation of the SERS enhancement factor (EF) for R6G analyte on different substrates (λ_{exc} : 785 nm and peak : 1507 cm^{-1}).*

Substrate		R6G (λ_{exc} : 785 nm)		
		I_{1507}	I_{SERS}/I_{Bulk}	EF ($\times 10^8$)
Cu-PVA		123	1	0.01
Cu-Ag-PVA [c (mM)]	1	256	3	0.02
	3	288	3	0.02
	6	451	5	0.03
	9	491	5	0.03
	12	40	0.4	0.002

Table 5.10. *Estimation of the SERS enhancement factor (EF) for MB analyte on different substrates (λ_{exc} : 488 nm and peak : 1620 cm^{-1}).*

Substrate		MB (λ_{exc} : 488 nm)		
		I_{1620}	I_{SERS}/I_{Bulk}	EF ($\times 10^8$)
Cu-PVA		200	5	0.03
Cu-Ag-PVA [c (mM)]	1	1295	35	0.18
	3	1192	32	0.17
	6	1376	37	0.19
	9	593	16	0.08
	12	417	11	0.06

Table 5.11. *Estimation of the SERS enhancement factor (EF) for MB analyte on different substrates (λ_{exc} : 633 nm and peak : 1620 cm^{-1}).*

Substrate		MB (λ_{exc} : 633 nm)		
		I_{1620}	I_{SERS}/I_{Bulk}	EF ($\times 10^8$)
Cu-PVA		611	8	0.05
Cu-Ag-PVA [c (mM)]	1	15933	202	1.37
	3	24310	308	2.09
	6	27594	350	2.37
	9	35464	449	3.04
	12	40687	515	3.49
Ag-PVA		2637	33	0.22

Table 5.12. *Estimation of the SERS enhancement factor (EF) for MB analyte on different substrates (λ_{exc} : 785 nm and peak : 445 cm^{-1}).*

Substrate		MB (λ_{exc} : 785 nm)		
		I_{445}	I_{SERS}/I_{Bulk}	EF ($\times 10^8$)
Cu-PVA		453	6	0.05
Cu-Ag-PVA [c (mM)]	1	1136	15	0.13
	3	1640	22	0.18
	6	1777	24	0.20
	9	3026	41	0.34
	12	5467	73	0.61

Table 5.13. *Enhancement factor for the Raman spectra of R6G recorded (with different λ_{exc}) on Cu-Ag-PVA thin films fabricated by treatment of Cu-PVA (x = 0.25) with different concentrations (c, mM) of $AgNO_3$; values for Cu-PVA and Ag-PVA are also shown.*

Substrate		EF ($\times 10^8$) for λ_{exc}		
		488 nm	**633 nm**	**785 nm**
Cu-PVA		0.06	0.01	0.01
Cu-Ag-PVA [c (mM)]	1	0.41	0.19	0.02
	3	0.77	0.26	0.02
	6	1.44	0.38	0.03
	9	1.77	1.31	0.03
	12	2.27	1.60	0.002
Ag-PVA		0.86	0.09	~ 0.00

Table 5.14. *Enhancement factor for the Raman spectra of MB recorded (with different λ_{exc}) on Cu-Ag-PVA thin films fabricated by treatment of Cu-PVA (x = 0.25) with different concentrations (c, mM) of $AgNO_3$; values for Cu-PVA and Ag-PVA are also shown.*

Substrate		EF ($\times 10^8$) for λ_{exc}		
		488 nm	**633 nm**	**785 nm**
Cu-PVA		0.03	0.05	0.05
Cu-Ag-PVA [c (mM)]	1	0.18	1.37	0.13
	3	0.17	2.09	0.18
	6	0.19	2.37	0.20
	9	0.08	3.04	0.34
	12	0.06	3.49	0.61
Ag-PVA		~ 0.00	0.22	~ 0.00

three excitation lasers, for the experiments on R6G and MB. Details of the estimation of the SERS EF in experiments using the three different laser excitations with R6G on different substrates are collected in Tables 5.7-5.9. Similar data for MB are collected in Tables 5.10-5.12. Summary of the EF estimated from the various experiments for the analytes R6G and MB are collected in Tables 5.13 and 5.14 respectively; it is seen that

the excitation wavelength of 488 nm provides the highest EF with the different Cu-Ag-PVA films for R6G, whereas 633 nm is the best suited for MB. These observations are consistent with the absorption profile of the two analyte molecules, and point to potential resonance effects in the Raman scattering response. It is seen also that the EF are very low with Cu-PVA; the Cu-Ag-PVA films produces EF of the order of 10^7-10^8, significantly higher than that obtained using Ag-PVA having higher Ag content. The Cu-Ag nanoparticle substrate provides not only strong plasmonic fields over a wide range of wavelengths facilitating excitation by different lasers, but also efficient enhancement due to the interfaces that form between the bimetallic particles. Table

Table 5.15. *Comparison of SERS enhancement factors of Cu-Ag based substrates reported earlier for different analytes using different excitation wavelengths.*

Ref. No	λ_{exc} (nm)	Analyte	EF ($\times 10^6$)
4	514	R6G	*
11	514	R6G	1.1
12	785	Fluoranthene	0.21
13	633	R6G	*
14	780	Perchlorate	*
15	514	R6G	1.15
16	514	MBO	0.001
17	532	R6G	*
18	633	CV	*
19	514	R6G	1.0
20	532	R6G	2.5
21	633	4-ABT	1.4
22	514	CV	240
23	532	R6G	*
25	532	R6G	*
26	785	4-MBA	0.37
27	514	R6G	10.0
Present	488	R6G	227
	633	MB	349

.

*Absolute value of EF is not reported, R6G: Rhodamine 6G, MBO: 2-mercaptobenzoxazole, CV: Crystal violet, MB: Methylene blue, 4-ABT: 4-aminobenzenethiol and 4-MBA: 4-mercaptobenzoic acid.

5.15 shows that SERS EF values obtained with Cu-Ag-PVA are significantly higher than that observed with a wide range of Cu-Ag based substrates and analyte molecules, in earlier reports.

5.5.2 *Limit of Detection*

We have examined the linearity of the SERS response with respect to the analyte concentration and the limit of detection (LOD). Raman spectra recorded for different concentrations of R6G (λ_{exc} = 488 nm) and MB (λ_{exc} = 633 nm) spread on the Cu-Ag-

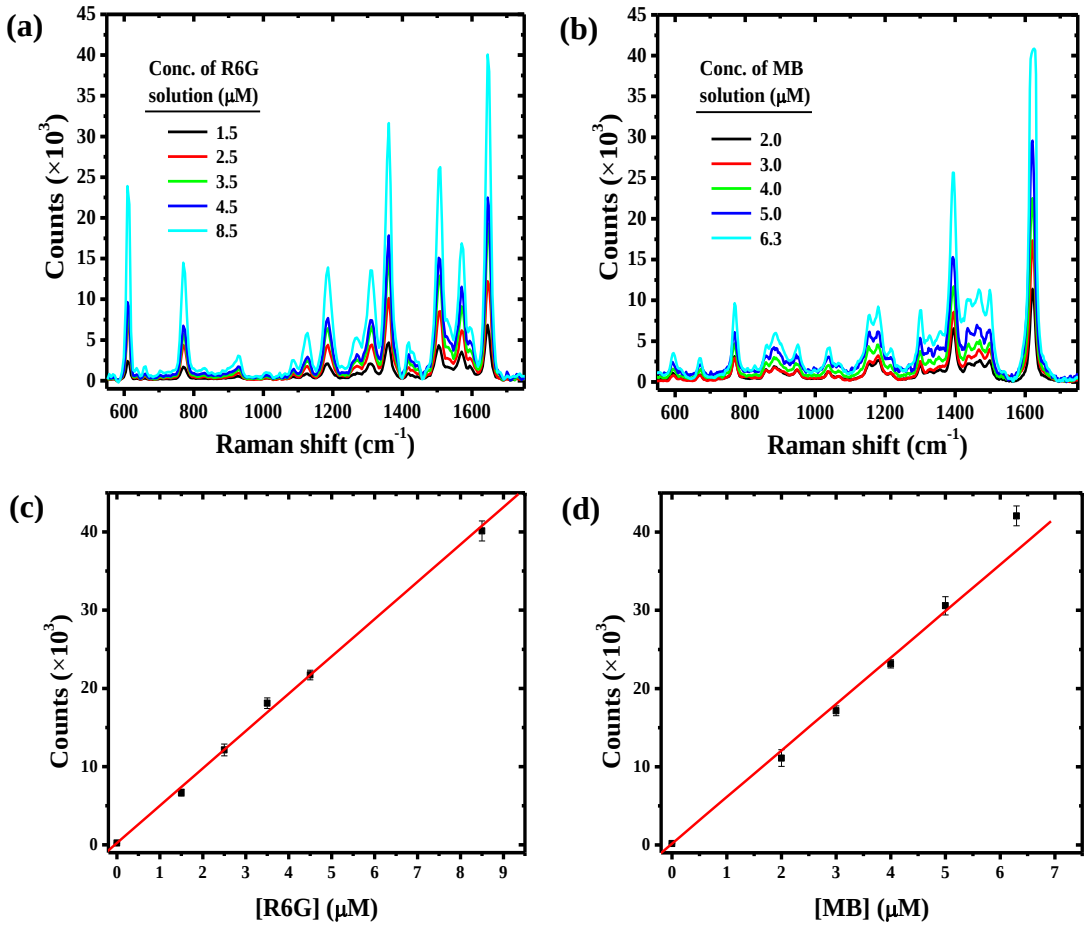

Figure 5.22. *Raman spectra for varying concentrations of* ***(a)*** *R6G (λ_{exc} = 488 nm) and* ***(b)*** *MB (λ_{exc} = 633 nm) on Cu-Ag-PVA thin film fabricated by treatment of Cu-PVA (x = 0.25) with 12 mM $AgNO_3$ solution. Plot of the intensity of* ***(c)*** *1645 cm^{-1} of the R6G spectra and* ***(d)*** *1620 cm^{-1} peak of the MB spectra versus concentration; standard deviations in the data and the linear best fit are shown.*

PVA film substrate (fabricated with c = 12 mM) are shown in Fig. 5.22a and 5.22b. Plots of the intensities of the 1645 cm^{-1} peak of R6G and 1620 cm^{-1} peak of MB versus the analyte solution concentration show clear linear variation (Fig. 5.22c,d). The LOD is defined as $3\sigma_{blank}/m$ (where σ_{blank} is the standard deviation for blank measurements and *m* is the slope of the intensity-concentration plot).[39,40] σ_{blank} on the Cu-Ag-PVA substrate (without probe molecules) was determined by recording the Raman spectra 5 times. The value was estimated to be 52 counts for the intensity at 1645 cm^{-1} (excitation at 488 nm) and 31 counts for the intensity at 1620 cm^{-1} (excitation at 633 nm); these corresponds to the Raman peaks of interest and the excitation wavelength for the probe molecules R6G and MB respectively. The slope *m* was determined from the calibration plot of signal intensity versus concentration; the plots for R6G and MB are shown in Fig. 5.22c and 5.22d. The LOD estimated are 0.66 pmol and 0.32 pmol for R6G and MB respectively. These observations point to the high sensitivities of detection that can be achieved using the Cu-Ag-PVA thin films as SERS substrates

5.6. Summary

We have demonstrated in this chapter, a facile route to the formation of stable bimetal-polymer nanocomposite thin films using the cost-effective choice of noble metals, Ag and Cu, serving as an efficient broad spectrum SERS substrate. Thin film with an optimal composition was shown to produce high enhancement factors for different analytes at varying excitation wavelengths. The general concept demonstrated can be implemented with other nanocomposite thin films to realize high SERS responses.

References

1. Schlücker, S. *Angew. Chem. Int. Ed.* **2014**, *53*, 4756−4795.
2. Pereira, A. J.; Gomes, J. P.; Lenz, G. F.; Schneider, R.; Chaker, J. A.; de Souza, P. E. N.; Felix, J. F. *J. Phys. Chem. C* **2016**, *120*, 12265−12272.
3. Tan, Y.; Gu, J.; Xu, W.; Chen, Z.; Liu, D.; Liu, Q.; Zhang, D. *ACS Appl. Mater. Interfaces* **2013**, *5*, 9878−9882.
4. Lee, J.; Chen, D.; Li, X.; Yoo, S.; Bottomley, L. A.; El-Sayed, M. A.; Park, S.; Liu, M. *Nanoscale* **2013**, *5*, 11620−11624.
5. McFarland, A. D.; Young, M. A., Dieringer, J. A.; Van Duyne, R. P. *J. Phys. Chem. B* **2005**, *109*, 11279−11285.
6. Álvarez-Puebla, R. A. *J. Phys. Chem. Lett.* **2012**, *3*, 857−866.
7. Sopousek, J.; Zobac, O.; Bursik, J.; Roupcova, P.; Vykoukal, V.; Broz, P.; Pinkas, J.; Vrestal, J. *Phys. Chem. Chem. Phys.* **2015**, *17*, 28277−28285.
8. Chen, H.; Zuo, J. *Acta Mater.* **2007**, *55*, 1617−1628.
9. Martinez De La Hoz, J. M.; Tovar, R. C.; Balbuena, P. B. *Mol. Simul.* **2009**, *35*, 785−794.
10. Grouchko, M.; Kamyshny, A.; Magdassi, S. *J. Mater. Chem.* **2009**, *19*, 3057−3062.
11. Guo, T.; Li, J.; Sun, X.; Sakka, Y. *Mater. Sci. Eng. C* **2016**, *61*, 97−104.
12. Jiang, X.; Lai, Y.; Yang, M.; Yang, H.; Jiang, W.; Zhan, J. *Analyst* **2012**, *137*, 3995−4000.
13. Mabbott, S.; Larmour, I. A.; Vishnyakov, V.; Xu, Y.; Graham, D.; Goodacre, R. *Analyst* **2012**, *137*, 2791−2798.
14. Hao, J.; Xu, Z.; Han, M.; Xu, S.; Meng, X. *Colloids Surf. A* **2010**, *366*, 163−169.
15. Gao, T.; Wang, Y.; Wang, K.; Zhang, X.; Dui, J.; Li, G.; Lou, S.; Zhou, S. *ACS Appl. Mater. Interfaces* **2013**, *5*, 7308−7314.

16. Pergolese, B.; Muniz-Miranda, M.; Bigotto, A. *J. Phys. Chem. B* **2006**, *110*, 9241−9245.

17. Chen, H.; Luo, J.; Zeng, T.; Jiang, L.; Sun, Y.; Jiao, Z.; Jin, Y.; Sun, X. *New J. Chem.* **2014**, *38*, 3907−3916.

18. Zhang, Q.; Chen, Y.; Guo, Z.; Liu, H.; Wang, D.; Huang, X. *ACS Appl. Mater. Interfaces* **2013**, *5*, 10633−10642.

19. Ke, X.; Lu, B.; Hao, J.; Zhang, J.; Qiao, H.; Zhang, Z.; Xing, C.; Yang, W.; Zhang, B.; Tang, J. *ChemPhysChem* **2012**, *13*, 3786−3789.

20. Jie, Z.; Pengyue, Z.; Yimin, D.; Xiaolei, Z.; Jiamin, Q.; Yong, Z. *Plasmonics* **2016**, DOI: 10.1007/s11468-016-0202-9.

21. Kim, K.; Lee, H. S. *J. Phys. Chem. B* **2005**, *109*, 18929−18934

22. Parisi, J.; Su, L.; Lei, Y. *Lab Chip* **2013**, *13*, 1501−1508.

23. Zhang, X.; Xu, S.; Jiang, S.; Wang, J.; Wei, J.; Xu, S.; Gao, S.; Liu, H.; Qiu, H.; Li, Z.; Liu, H.; Li, Z.; Li, H. *Appl. Surf. Sci.* **2015**, *353*, 63−70.

24. Gellini, C.; Sabatino, G.; Papini, A. M.; Muniz-Miranda, M. *J. Raman Spec.* **2014**, *45*, 418−423.

25. Chen, X.; Cui, C.; Guo, Z.; Liu, J.; Huang, X.; Yu, S. *Small* **2011**, *7*, 858−863.

26. Li, D.; Liu, J.; Wang, H.; Barrow, C. J.; Yang, W. *Chem. Commun.* **2016**, *52*, 10968-10971.

27. Chen, L. Y.; Zhang, L.; Fujita, T.; Chen, M. W. *J. Phys. Chem. C* **2009**, *113*, 14195−14199

28. Porel, S.; Singh, S.; Harsha, S. S.; Rao, D. N.; Radhakrishnan, T. P. *Chem. Mater.* **2005,** *17*, 9−12.

29. Ramesh, G. V.; Porel, S.; Radhakrishnan, T. P. *Chem. Soc. Rev.* **2009,** *38*, 2646−2656.

30. Hariprasad, E.; Radhakrishnan, T. P. in *Nanocomposites: In Situ Synthesis of Polymer-Embedded Nanostructures*, Eds. Carotenuto, G.; Nicolais, L. John Wiley and Sons, **2013**, p.129–144.

31. Rao, V. K.; Radhakrishnan, T. P. *J. Mater. Chem. A,* **2013,** *1,* 13612–13618.

32. Rao, V. K.; Radhakrishnan, T. P. *ACS Appl. Mater. Interfaces* **2015**, *7,* 12767−12773.

33. Hariprasad, E.; Radhakrishnan, T. P. *Langmuir* **2013**, *29*, 13050−13057.

34. Gawande, M. B.; Goswami, A.; Felpin, F.; Asefa, T.; Huang, X.; Silva, R.; Zou, X.; Zboril, R.; Varma, R. S. *Chem. Rev.* **2016**, *116*, 3722−3811.

35. Rehman, S.; Mumtaz, A.; Hasanain, S. K. *J. Nanopart. Res.* **2011,** *13*, 2497–2507.

36. Dagher, S.; Haik, Y.; Ayesh, A. I.; Tit, N. *J. Lumin.* **2014**, *151*, 149–154.

37. Watts, J. F.; Wolstenholme, J. *An introduction to Surface Analysis by XPS and AES*, John Wiley & Sons Ltd., Chichester, England, **2003**.

38. Andrea, C. D.; Irrera, A.; Fazio, B.; Foti, A.; Messina, E.; Maragò, O. M.; Kessentini, S.; Artoni, P.; David, C.; Gucciardi, P. G. *J. Opt.* **2015**, *17*, 114016 (1–8).

39. El-Safty, S. A.; Ismail, A. A.; Matsunaga, H.; Nanjo, H.; Mizukami, F. *J. Phys. Chem. C* **2008**, *112*, 4825–4835.

40. Christian, G. D. *Analytical Chemistry*, 6th ed.; John Wiley & Sons Inc.: New York, **2003**.

CHAPTER 6

Overview of the Present Work, New Directions and Future Prospects

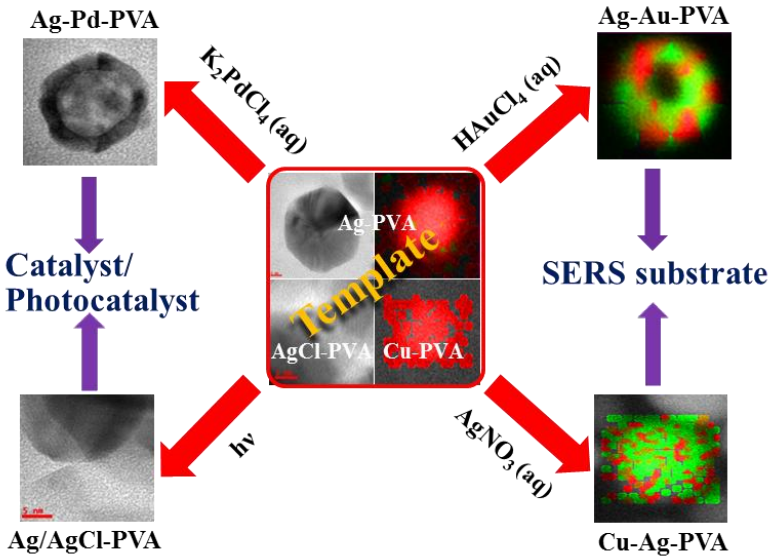

6.1 Overview of the Present Work

Development of new designs and novel fabrication methods of nanomaterials, as well as exploration of their unique characteristics and applications are core issues in contemporary research. Deep interest and extensive activity continue because of the uniqueness of these materials and the promise they hold for future technologies. The ability to control the growth, morphology and interfacial interactions of nanoparticles is highly important for realising well-defined and reproducible properties of nanomaterials. Polymer-embedded nanostructures are of special interest, and are potentially useful in various technological applications. The *in situ* methodology developed in our laboratory, for the fabrication of metal nanoparticles in polymer thin films, is one of the efficient, simple and environmentally benign approaches that enables control of size, shape and distribution of the particles.[1,2] A significant features of this protocol is that it allows us to monitor the nanoparticles during their fabrication as well as repeated applications in various situations, using techniques like spectroscopy, microscopy and chemical analysis. Embedding the nanoparticles inside the polymer film effectively prevents aggregation and enables long-term storage of these nanocomposite films, an aspect of considerable practical utility. Earlier work in our laboratory has demonstrated the appreciable optical limiting capability,[3,4] effective antibacterial activity,[5] strong microwave absorption,[6] selective chemical sensing,[7] efficient catalytic activity[8,9] and surface enhanced Raman scattering (SERS) capability of the metal-polymer nanocomposite thin films.[10]

The work presented in this thesis demonstrates the facile extension of the protocol, for the *in situ* generation of bimetallic and metal/semiconductor nanoparticles in polymer thin films, and their efficient applications in catalysis, photocatalysis and SERS (Fig. 6.1). We have used poly(vinyl alcohol) (PVA) as the polymer, in the different studies presented. PVA acts as both the reducing agent for the formation of noble metal nanoparticles from their precursor (using the hydroxy functionality), and as the stabilizing agent for the nanoparticles. The polymer gets cross linked during the fabrication process and becomes insoluble even in water; the resulting stability of the

thin film, is a key factor for its versatile applications. The hydrogel nature of the PVA is also equally important; it allows the film to swell in an aqueous medium and provides efficient access for the reactant molecules to nanoparticles embedded within. This is critical for the high efficiency of the nanocomposite thin films in applications such as catalysis and sensing. The thin film structure of nanocomposite facilitated easy retrieval and reinsertion of the catalyst into the reaction system, justifying the qualification, 'dip catalyst'. We have developed an efficient and facile method for the controlled fabrication of bimetallic nanoparticles in polymer thin films, using a suitable metal nanoparticle, M (Ag or Cu) as a sacrificial template. Treatment of the M-PVA thin film with an aqueous solution of the precursor of a second metal (N, with higher reduction potential compared to M, eg. Pd or Au relative to Ag or Ag relative to Cu), under ambient conditions, generates bimetal-polymer nanocomposite system (M-N-PVA); the process involved is a simple galvanic displacement. Hollow bimetallic (Ag-Pd and Ag-Au) nanoparticles were generated inside the polymer thin film with controlled composition and morphology. We have also developed a general approach to fabricate metal/semiconductor-polymer nanocomposite; the example illustrated is Ag/AgCl-PVA formed by the visible light irradiation of preformed AgCl nanoparticles in PVA thin film immersed in water.

Application potential of the bimetal-polymer (Ag-Pd-PVA) and metal/semiconductor-polymer (Ag/AgCl-PVA) nanocomposite thin films is demonstrated by employing them as a 'dip catalyst' in carbon - carbon bond formation reaction and photo-degradation of a dye respectively. The hollow bimetal-polymer nanocomposite thin film (Ag-Pd-PVA) is shown to be a significantly more efficient catalyst over the single metal nanocomposite thin film (Pd-PVA) in spite of the considerably lower precious metal content, because of the high surface area provided by the hollow morphology. The Ag/AgCl-PVA thin film served as an efficient plasmonic photocatalyst for the dye degradation, affording multiple, efficient reuses; the thin film nature of the catalyst allowed careful monitoring during the reuse cycles, yielding useful insight into the status of the catalyst and the eventual decline of its activity.

Another application of interest discussed in the thesis is the use of bimetal-polymer (Ag-Au-PVA and Cu-Ag-PVA) nanocomposite thin films as efficient SERS substrates. Thin films with optimized bimetallic composition were shown to produce high SERS enhancement factors of the order of 10^8, with sub-picomol limits of detection for some standard analytes. Some fundamental questions in this field could also be addressed; composition (and hence the LSPR extinction) dependence of the SERS efficiency using Ag-Au-PVA thin films, as well as the broad spectral applications of Cu-Ag-PVA thin film for different analytes were demonstrated.

We believe that the fabrication, characterization and applications of the *in situ* fabricated bimetal and metal/semiconductor-polymer nanocomposite thin films presented in this thesis represent a new direction in the field of nanocomposite materials. Further optimization of the methodologies we have developed, could lead to further improvement of the desired features and functions of these novel materials.

6.2 New Directions of Research

The *in situ* method presented in this thesis can be extended to fabricate polymer thin films with a wide range of important bimetallic nanoparticles, such as Ag-Pt, Cu-Au, Cu-Pd and Cu-Pt. Nanoparticles of metals such as Ag and Cu are appropriate as sacrificial template for the generation of these bimetallic systems; this is confirmed by some preliminary experiments that we have carried out. The *in situ* method that we have developed for the fabrication of nanoparticles of metals with low reduction potential (eg. copper) using an external reducing agent, could be employed in the case of other metals such as Ni and Fe, which can also act as a template for further synthesis. Morphology of the resultant bimetallic particles is dependent on the difference in the reduction potentials as well as the relative rate of diffusion of the metals used. The fabrication protocol can easily be extended to multi-metallic systems like Ag-Au-Pd, Ag-Au-Pt and Ag-Pd-Pt. Fabrication of metal nanoparticles in polymer films described in this thesis involved thermal treatment, photo-irradiation and chemical reduction. Alternate methods like microwave heating, electron beam irradiation/electron beam lithography and focused ion beams, for the generation of metal nanoparticles *in situ*

inside the polymer films need to be explored. The reduction process can have significant effect on the particle size and shape distribution, depending on the nucleation and growth processes involved.

Another interesting avenue to investigate is the synthesis of semiconductor nanoparticles inside polymer thin films. Simple approaches would involve the thermal decomposition of suitable metal precursors inside the polymer thin film. Another approach would be to use the metal nanoparticles generated inside the film as templates to obtain nanoparticles of metal oxide or metal sulfide through oxidation or sulfidation. Semiconductor/semiconductor-polymer nanocomposite could be fabricated by the simultaneous thermal decomposition of two metal precursors inside the polymer thin film. Photocatalytic applications of a wide range of metals/semiconductor composite nanostructures in polymer thin films remains to be investigated. The fabrication of these catalyst films could involve the partial oxidation of metal to form semiconductor as well as the partial reduction of semiconductor to form metal.

Use of conjugated polymers (such as polypyrrole and polyaniline) as the matrix and the *in situ* generation of nanoparticles to form nanocomposite thin films would be another direction for future studies. The optical and electronic properties of these thin films are likely to be fascinating. Development of chemical and biological sensors based on various metal-polymer combinations would be interesting. The wide range of possibilities thus includes metal, multimetal, metal/semiconductor, semiconductor, semiconductor/semiconductor-polymer (conjugated polymer) nanocomposite thin films; they are likely to have immense potential in areas such as sensing, photonics and fuel cells. Use of top-down approaches like lithography to patterns the various composite structures embedded in the polymer thin film can have important application in device fabrication.

The development and applications of bimetal-polymer and metal/semiconductor-polymer nanocomposite thin films presented in this thesis, and the exploration of the proposed ideas and methods outlined above, will open up new avenues for promising and exciting research in future.

References

1. Porel, S.; Singh, S.; Radhakrishnan, T. P. *Chem. Commun.* **2005**, 2387-2389.
2. Porel, S.; Hebalkar, N.; Sreedhar, B.; Radhakrishnan, T. P. *Adv. Funct. Mater.* **2007**, *17*, 2550-2556.
3. Porel, S.; Singh, S.; Harsha, S. S.; Rao, D. N.; Radhakrishnan, T. P. *Chem. Mater.* **2005**, *17*, 9-12.
4. Porel, S.; Venkatram, N.; Rao, D. N.; Radhakrishnan, T. P. *J. Appl. Phys.* **2007**, *102*, 033107.
5. Porel, S.; Ramakrishna, D.; Hariprasad, E.; Gupta, A. D.; Radhakrishnan, T. P. *Curr. Sci.* **2011**, *101*, 927-934.
6. Ramesh, G. V.; Sudheendran, K.; Raju, K. C. J.; Sreedhar, B.; Radhakrishnan, T. P. *J. Nanosci. Nanotechnol.* **2009**, *9*, 261-266.
7. Ramesh, G. V.; Radhakrishnan, T. P. *ACS Appl. Mater. Interfaces* **2011**, *3*, 988-994.
8. Hariprasad, E.; Radhakrishnan, T. P. *Chem. Eur. J.* **2010**, *16*, 14378-14384.
9. Hariprasad, E.; Radhakrishnan, T. P. *ACS Catal*. **2012**, *2*, 1179-1186.
10. Hariprasad, E.; Radhakrishnan, T. P. *Langmuir* **2013**, *29*, 13050-13057.

Appendix

APPENDIX

Materials

Silver nitrate	:	Aldrich, 99+%
Copper (II) nitrate trihydrate	:	Aldrich, 99+%
Potassium tetrachloropalladate (II)	:	Aldrich, 99.99%
Hydrogen tetrachloroaurate (III) trihydrate	:	Aldrich, 99.9+%
Hydrazine hydrate	:	Finar, 80%
Hydrochloric acid	:	Merck, 37%
Iodobenzene	:	Aldrich, 98%
Phenylboronic acid	:	Aldrich, 95%
Rhodamine 6G	:	Aldrich, 95%
Methylene blue	:	Aldrich, 97%
Methyl orange	:	Aldrich, 85%
Polystyrene	:	Aldrich, M_w = 280 kDa
Poly(vinyl alcohol)	:	Aldrich, M_w = 87-146 kDa, % hydrolysis = 99+ Aldrich, M_w = 146-186 kDa, % hydrolysis = 99+
Nitric acid	:	Merck, ≥69%
Ultrapure water	:	Millipore MilliQ (resistivity = 18.2 MΩ cm)

Instrumentation

Spin-coater

Laurell Technologies Corporation Model WS-650HZ-23NPP/LITE photoresist spinner was used for the fabrication of thin polymer films.

Film thickness measurement

Thickness of the films was measured using an Ambios Technology XP-1 profilometer.

Absorption spectroscopy

Absorption spectra were recorded on a Cary 100 UV-Visible spectrophotometer or Shimadzu Model UV-3100 UV-Visible Spectrophotometer.

X-ray photoelectron spectroscopy

XPS analysis was carried out on a VG Microtech, model ESCA 3000 instrument equipped with ion gun (EX-05) for cleaning the surface; with binding energy resolution of 0.1 eV. Un-monochromatized Al K_α radiation (photon energy = 1486.6 eV) was used where the electron take off angle (angle between electron emission direction and surface plane) was 60^o. Spectra were calibrated using the C 1s peak at 284.8 eV.

X-ray Diffractometer

X-ray diffraction was recorded on a SMART Bruker D8 Advance X-ray Diffractometer using Cu-K_α radiation (λ = 1.5406 Å).

Atomic force microscopy

AFM images were recorded on a Solver Pro M (NT-MDT) atomic force microscope in contact and semi-contact modes. A tip having a force constant of 11.8 N/m was used in semi-contact mode. Images were analyzed using the NOVA (version 1.0.26) software supplied by the microscope manufacturer.

Scanning electron microscopy

Field emission scanning electron microscope (FE-SEM) imaging with energy dispersive X-ray spectroscopy (EDXS) was carried out on a Carl Zeiss model Ultra 55

microscope; EDX spectra and maps were recorded using Oxford Instruments X-Max^N SDD (50 mm^2) system and INCA analysis software.

Transmission electron microscopy

TEM images were recorded on a FEI TECNAI G^2 S-Twin 200 kV TEM at an accelerating voltage of 200 kV.

Inductively coupled plasma-optical emission spectrometer

A Varian Model Liberty Series ICP-OES was used. Samples dissolved in 69% aqueous nitric acid and diluted to required concentrations were used.

Ion Chromatography

A Metrohm 850 Professional Ion Chromatography (IC) was used. Sample for the analysis was prepared by dissolving the film in 24 ml pyridine-water (1:5 v/v) mixture and sonicating for 30 min, followed by adding 20 ml of 69% nitric acid and sonicating for another 30 min; the solution volume was finally made up to 100 ml using water.

Gas chromatograph-mass spectrometer

GCMS analysis was carried out on Shimadzu model QP2010 Gas chromatograph-Mass spectrometer.

Confocal Raman microscope

WITec model Alpha300 R equipped with an AFM was used for the Raman spectral studies.

Publications and Presentations

PUBLICATIONS

1. **Rao, V. K.;** Radhakrishnan, T. P. Hollow Bimetallic Nanoparticles Generated *in situ* Inside a Polymer Thin Film: Fabrication and Catalytic Application of Silver-Palladium-Poly(vinyl alcohol). *J. Mater. Chem. A* **2013**, *1*, 13612-13618.

2. **Rao, V. K.;** Radhakrishnan, T. P. Tuning the SERS Response with Ag-Au Nanoparticle-Embedded Polymer Thin Film Substrates. *ACS Appl. Mater. Interfaces* **2015**, *7*, 12767-12773.

3. Madhuri, U. D.; **Rao, V. K;** Hariprasad, E.; Radhakrishnan, T. P. *In Situ* Fabricated Platinum-Poly(vinyl alcohol) Nanocomposite Thin Film: a Highly Reusable 'Dip Catalyst' for Hydrogenation. *Mater. Res. Express* **2016**, *3*, 045018.

4. **Rao, V. K.;** Radhakrishnan, T. P. *In Situ* Fabricated Ag/AgCl-Polymer Nanocomposite Thin Film: An Appraisal of the Efficient and Reusable Photocatalyst. *Mater. Res. Bull*. **2017**, *87*, 193-201.

5. **Rao, V. K.;** Ghildiyal, P.; Radhakrishnan, T. P. *In Situ* Fabricated Cu-Ag Nanoparticle-Embedded Polymer Thin Film as an Efficient Broad Spectrum SERS Substrate. *J. Phys. Chem. C (accepted).*

PRESENTATIONS

1. Poster presentation: 13th Eurasia Conference on Chemical Science, Bangalore, India, December 14-18, **2014**.
   Hollow Bimetallic Ag-Pd and Ag-Au Nanoparticle-Embedded Polymer Thin Film: Fabrication, Characterization and Applications.

2. Oral presentation: 7th International workshop on Polymer/Metal nanocomposites, Jaipur, Rajasthan, November 02-05, **2015**.
   Efficient Catalytic Activity of Hollow Ag-Pd Nanoparticle and Tuning the SERS Response with Ag-Au Nanoparticle-Embedded Polymer Thin Films.

3. Poster presentation: International Conference on Materials for the Millenium (MATCON-2016), Cochin University of Science and Technology, January 14-16, **2016**.
   Ag-Au and Ag/AgCl Nanoparticles-Embedded Polymer Thin Films: Tunable SERS Substrate and Efficient Photocatalyst.

4. Oral presentation: Chemfest-2016, University of Hyderabad, Hyderabad, India, February 17-18, **2016**.
   Bimetallic and Metal-Semiconductor Nanoparticles-Embedded Polymer Thin Films: *In Situ* Fabrication and Applications.

BIMETALLIC AND METAL/SEMICONDUCTOR NANOPARTICLE EMBEDDED POLYMER THIN FILMS

ORIGINALITY REPORT

%2	%1	%2	%0
SIMILARITY INDEX	INTERNET SOURCES	PUBLICATIONS	STUDENT PAPERS

PRIMARY SOURCES

1	Rao, V. Kesava, and T. P. Radhakrishnan. "Hollow bimetallic nanoparticles generated in situ inside a polymer thin film: fabrication and catalytic application of silver–palladium–poly(vinyl alcohol)", Journal of Materials Chemistry A, 2013. Publication	<%1
2	Submitted to University of South Australia Student Paper	<%1
3	Ramesh, G. V., S. Porel, and T. P. Radhakrishnan. "Polymer thin films embedded with in situ grown metal nanoparticles", Chemical Society Reviews, 2009. Publication	<%1
4	repository.ias.ac.in Internet Source	<%1
5	www.science.gov Internet Source	<%1
6	Prakash, Jai, R.A. Harris, and H.C. Swart. "Embedded plasmonic nanostructures:	<%1

synthesis, fundamental aspects and their surface enhanced Raman scattering applications", International Reviews in Physical Chemistry, 2016.
Publication

7	Submitted to 9561 Student Paper	<%1
8	Madhuri, U Divya, V Kesava Rao, E Hariprasad, and T P Radhakrishnan. "In situ fabricated platinum—poly(vinyl alcohol) nanocomposite thin film: a highly reusable ‘dip catalyst’ for hydrogenation", Materials Research Express, 2016. Publication	<%1
9	file.scirp.org Internet Source	<%1
10	S. Rizk. "Synthesis of SiC nanofibers by microwave plasma assisted chemical vapour deposition in CH4/H2 gas mixture", physica status solidi (a), 09/2007 Publication	<%1
11	Gerald Young. "Overview of the Present Work", Development and Causality, 2011 Publication	<%1
12	Zhang, Hui, Mingshang Jin, and Younan Xia. "Enhancing the catalytic and electrocatalytic properties of Pt-based catalysts by forming bimetallic nanocrystals with Pd", Chemical	<%1

Society Reviews, 2012.
Publication

13	Hariprasad, E., and T. P. Radhakrishnan. "Palladium Nanoparticle-Embedded Polymer Thin Film “Dip Catalyst” for Suzuki–Miyaura Reaction", ACS Catalysis, 2012. Publication	<%1
14	www.eu-softcomp.net Internet Source	<%1
15	www.osti.gov Internet Source	<%1
16	Puišo, J.; Baltrušaitis, V.; Ponelytė, S.; Prosyčevas, I. and Guobienė, A.. "Ag/PVA Nanocomposite Formation and its Application in Microsystem Devices", Mechanika, 2013. Publication	<%1
17	Goldbach, Tobias. "Introduction", Control Modes on Mobile Software Platforms, 2016. Publication	<%1
18	Abreu, C.M.. "Long-term behaviour of AISI 304L passive layer in chloride containing medium", Electrochimica Acta, 20060120 Publication	<%1
19	S. Porel. "Palladium Nanowire from Precursor Nanowire: Crystal-to-Crystal Transformation via In Situ Reduction by Polymer Matrix", Advanced Functional Materials, 09/24/2007 Publication	<%1

20	Shang, Jing, and Xiaohu Gao. "Nanoparticle counting: towards accurate determination of the molar concentration", Chemical Society Reviews, 2014. Publication	<%1
21	Ramesh, G. V., B. Sreedhar, and T. P. Radhakrishnan. "Real time monitoring of the in situ growth of silver nanoparticles in a polymer film under ambient conditions", Physical Chemistry Chemical Physics, 2009. Publication	<%1
22	"Biomedical and Pharmaceutical Applications of Electrochemistry", Springer Nature, 2016 Publication	<%1
23	Lee, Hae Mi, Seung Min Jin, Hyung Min Kim, and Yung Doug Suh. "Single-molecule surface-enhanced Raman spectroscopy: a perspective on the current status", Physical Chemistry Chemical Physics, 2013. Publication	<%1
24	Abargues, R., M. L. Martinez-Marco, P. J. Rodriguez-Canto, J. Marques-Hueso, and J. P. Martinez-Pastor. "Metal-polymer nanocomposite resist: a step towards in-situ nanopatterns metallization", Advances in Resist Materials and Processing Technology XXX, 2013. Publication	<%1